Evaporated Sn-doped In₂O₃ films: Basic optical properties and applications to energy-efficient windows

I. Hamberg and C. G. Granqvist

Physics Department, Chalmers University of Technology, S-412 96 Gothenburg, Sweden

We review work on In_2O_3:Sn films prepared by reactive e-beam evaporation of In_2O_3 with up to 9 mol % SnO_2 onto heated glass. These films have excellent spectrally selective properties when the deposition rate is ~ 0.2 nm/s, the substrate temperature is $\gtrsim 150$ °C, and the oxygen pressure is $\sim 5 \times 10^{-4}$ Torr. Optimized coatings have crystallite dimensions $\gtrsim 50$ nm and a C-type rare-earth oxide structure. We cover electromagnetic properties as recorded by spectrophotometry in the 0.2–50-μm range, by X-band microwave reflectance, and by dc electrical measurements. Hall-effect data are included. An increase of the Sn content is shown to have several important effects: the semiconductor band gap is shifted towards the ultraviolet, the luminous transmittance remains high, the infrared reflectance increases to a high value beyond a certain wavelength which shifts towards the visible, phonon-induced infrared absorption bands vanish, the microwave reflectance goes up, and the dc resisitivity drops to $\sim 2 \times 10^{-4}$ Ω cm. The corresponding mobility is ~ 30 cm²/V s. The complex dielectric function ϵ is reported. These data were obtained from carefully selected combinations of spectrophotometric transmittance and reflectance data. It is found that ϵ can be reconciled with the Drude theory only by assuming a strongly frequency-dependent relaxation energy between the plasma energy and the band gap. We review a recently formulated quantitative theoretical model for the optical properties which explicitly includes the additive contributions to ϵ from valence electrons, free electrons, and phonons. The theory embodies an effective-mass model for n-doped semiconductors well above the Mott critical density. Because of the high doping, the Sn impurities are singly ionized and the associated electrons occupy the bottom of the conduction band in the form of an electron gas. The Sn ions behave approximately as point scatterers, which is consistent with pseudopotential arguments. Screening of the ions is described by the random phase approximation. This latter theory works well as a consequence of the small effective electron radii. Exchange and correlation in the electron gas are represented by the Hubbard and Singwi–Sjölander schemes. Phonon effects are included by three empirically determined damped Lorentz oscillators. Free-electron properties are found to govern the optical performance in the main spectral range. An analysis of the complex dynamic resistivity (directly related to ϵ) shows unambiguously that Sn ions are the most important scatterers, although grain-boundary scattering can play some role in the midvisible range. As a result of this analysis one concludes that the optical properties of the best films approach the theoretical limit. Band-gap shifts can be understood as the net result of two competing mechanisms: a widening due to the Burstein–Moss effect, and a narrowing due to electron-electron and electron-ion scattering. The transition width—including an Urbach tail—seems to be consistent with these notions. Window applications are treated theoretically from detailed computations of integrated luminous, solar, and thermal properties. It is found that In_2O_3:Sn films on glass can yield $\sim 78\%$ normal solar transmittance and $\sim 20\%$ hemispherical thermal emittance. Substrate emission is found to be insignificant. Antireflection with evaporated MgF_2 or high-rate sputtered aluminum oxyfluoride can give $\sim 95\%$ normal luminous transmittance, $\sim 5\%$ normal luminous reflectance, little perceived color and little increase in emittance. A color purity $< 1\%$ in normal transmission and $< 10\%$ in normal reflection is achievable for a daylight illuminant within extended ranges of film thickness.

I. INTRODUCTION

This review aims at giving a thorough analysis of the optical properties of tin-doped indium oxide films produced by reactive e-beam evaporation onto heated glass. The coating material is also known as indium tin oxide or ITO. The purpose of the review is twofold: to summarize the current understanding of the basic optical properties of a heavily doped oxide semiconductor, and to discuss the applicability of this material to coatings for obtaining energy efficiency of windows.

In_2O_3:Sn, and also some other doped oxide semiconductors, can show an interesting and technologically important combination of properties: they have high luminous transmittance, high infrared reflectance, good electrical conductivity, excellent substrate adherence, hardness, and chemical

inertness. It is not surprising that there have been many investigations of this type of material. Some of this work is summarized in several earlier reviews.[1-11] In_2O_3:Sn is probably the most widely studied material with the above-mentioned properties. Surface coatings have been produced by a variety of techniques such as evaporation in a reactive atmosphere[12-32] or in vacuum,[23,33-35] sputtering in reactive[36-65] or nonreactive atmosphere,[48,66-75] reactive ion plating,[76-78] glow-discharge deposition,[79-80] different varieties of chemical vapor deposition,[81-106] and dip coating.[107] Some results are available[108] also for In_2O_3:F. Coatings of pure In_2O_3—which are of central importance for understanding the doped material—have been produced by evaporation in reactive atmosphere[13,14,22,25,109-116] and in vacuum,[34,117,118] sputtering in reactive[57,60,119-125] or nonreactive atmosphere,[34] reactive ion plating,[126,127] chemical vapor deposition,[81,94,100,128-134] and oxidation of an In metal film.[135] Many reports describe techniques to improve the properties by post-deposition heat treatment. The great majority of the published papers is of technical nature and is limited to fabrication methods and ensuing film properties. It is surprising that this overwhelmingly large empirical work has not been matched by corresponding scientific efforts to understand the properties—notably the optical performance—on a fundamental level until very recently. Also, it is undoubtedly so that many of the published reports are repetitive and of rather limited value. This review is focused on the physical mechanisms governing the optical properties and applies this knowledge to devise coatings with a performance approaching the theoretical limits. Thus we wish to lay a solid ground for further research on heavily doped semiconductors for potential applications on windows, etc. It is our hope that there will be less need for trial-and-error experiments in the future.

The optical requirements of window coatings[2,6,7,9,11,136-143] are conveniently introduced by considering the radiative properties of our ambience. The upper part of Fig. 1 presents the most important of these on a common logarithmic wavelength scale. The solid curves in the right-hand part show blackbody exitance spectra in megawatt per square meter and wavelength increment (in meter) for bodies having three temperatures (− 50, 0, and + 50 °C) of interest for window applications. The exitance is increased for increasing temperature, and the peak in the curves—which lies at ∼ 10 μm—is shifted somewhat towards shorter wavelength λ. The thermal radiation from a body is given by the blackbody spectrum times a spectral emittance whose magnitude is less than unity. It is found that the thermal radiation is insignificant at $\lambda \lesssim 3$ μm. The solid curve at the left-hand part of the figure shows a typical solar irradiance spectrum in gigawatt per square meter and wavelength increment (in meters). The actual curve[144] is known as the air mass one (AM1) spectrum and represents the radiation at sea level for clear weather and the sun at zenith. The overall curve shape corresponds to the sun's surface temperature (∼ 5500 °C). The more or less sharp minima originate from atmospheric absorption in molecules of water vapor, carbon dioxide, and ozone. When the sun is off-zenith these absorption bands become more prominent, but the general curve
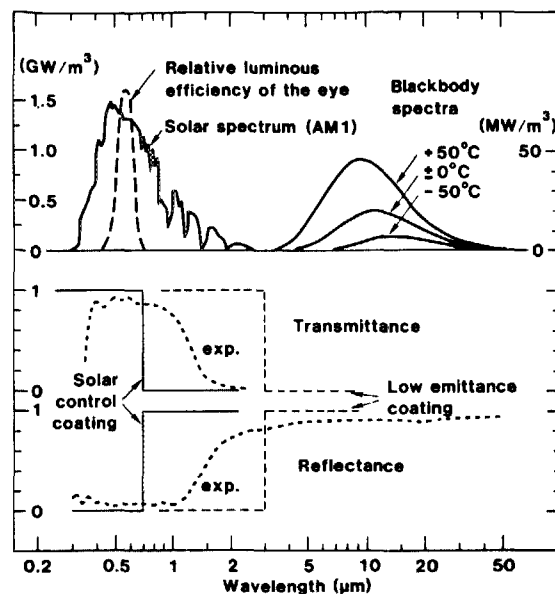

FIG. 1. Upper part shows the relative luminous efficiency of the light-adapted eye (from Ref. 145), a typical solar spectrum for one air mass (from Ref. 144), and blackbody spectra corresponding to three temperatures. Lower part shows transmittance and reflectance for idealized window coatings designed for "solar control" (solid lines) and for low thermal emittance (dashed lines). Dotted curves refer to experimental data for a 0.36-μm-thick In_2O_3:Sn film overcoated with 0.10 μm of MgF_2 and deposited onto glass (cf. Sec. X B).

shape is not altered. The irradiated intensity is almost zero for $\lambda > 3$ μm, and hence there is practically no overlap between the solar and thermal spectra. The dashed curve in the left-hand part of the figure refers to the CIE relative photopic retinal spectral-sensitivity function[145]; it is peaked at $\lambda \approx 0.56$ μm. It is inferred that only part of the solar radiation is useful for the human eye. In particular, there is a large fraction—carrying ∼ 45% of the solar energy—which comes as invisible near-infrared sunlight.

It is now possible to specify the desired properties of coatings for energy-efficient windows. Two different cases must be considered. First we think of a *cold* climate. Here we wish to have a window which is transparent for solar radiation, so that maximum benefit can be received from direct solar heating, while the thermal emittance should be decreased thereby improving the insulation and making the window a less serious heat leak. Consequently, we look for a coating with maximum transmittance at $\lambda < 3$ μm and maximum reflectance at $\lambda > 3$ μm. The ideal performance is indicated by the dashed lines in the lower part of Fig. 1. For a *warm* climate the situation is different. Here the solar energy which enters through a window is frequently causing an overheating which must be balanced by air conditioning. Thus, one can achieve energy efficiency by a coating which is transparent for visible light, i.e., at $\lambda < 0.7$ μm, while it is reflecting off the infrared sunlight at $0.7 < \lambda < 3$ μm. The ideal property for such a "solar control coating" is shown by the solid lines in the lower part of Fig. 1.

We find that selectively transmitting coatings are of interest for windows irrespective of the climate being cold or

warm; only the wavelength where the shift from high transmittance to high reflectance takes place should be different. The dotted curves in Fig. 1 refer to measured transmittance and reflectance of a window coating, based on In_2O_3:Sn, having intermediate properties. The preparation and analysis of this type of coating—including the factors governing the wavelength and width of the transmitting/reflecting transition—is the main theme of this review.

This review is organized as follows: Section II covers film fabrication by reactive e-beam evaporation. It is found that high-quality spectrally selective coatings of In_2O_3:Sn are obtained by slow deposition in the presence of oxygen onto glass substrates heated to > 150 °C. Film characterization by transmission electron microscopy and electron diffraction is presented in Sec. III, together with a discussion of the pertinent defects in In_2O_3:Sn. Good optical properties are associated with crystallites larger than ~50 nm in size and a C-type rare-earth oxide structure. Section IV is devoted to measured electromagnetic properties and first treats spectrophotometry in the $0.2 < \lambda < 50$ μm range—techniques as well as typical results. Increasing the Sn content in In_2O_3:Sn films has important consequences: the infrared reflectance goes up while the luminous transmittance is conserved, which is clearly desired for a window coating, while the fundamental semiconductor band gap is shifted towards the ultraviolet. This section also includes brief discussions of electrical resistivity, mobility, and microwave reflectance. Dielectric functions of In_2O_3 and In_2O_3:Sn are presented in Sec. V. The techniques required to obtain the results, and for assessing their numerical accuracy and internal consistency, are outlined. A qualitative treatment in terms of the Drude theory is included. Section VI sets the scene for the subsequent quantitative analysis of the optical properties by discussing the bandstructure of In_2O_3:Sn and giving a survey over the different physical mechanisms which contribute to the dielectric function. In Sec. VII we treat the optical properties around the band gap. A progressive widening of the band gap as the electron density goes up is explained as a Burstein–Moss shift which is partially compensated by manybody effects (electron-electron and electron-ion scattering). We also discuss logarithmic band edges. Section VIII gives a detailed account of the free-electron properties, which are prevalent in the main spectral range. We review a recent theory of ionized impurity scattering, and demonstrate that it yields a quantitative description of the optical data. The model treats singly ionized Sn defects in an In_2O_3 lattice and uses the random phase approximation (or extensions thereof) to represent screening in the electron gas. Section IX is devoted to the effects of phonons. It is found that their influence on the dielectric function can be approximated by three damped Lorentz oscillators. In Sec. X we turn to the application of In_2O_3:Sn to energy-efficient windows. For the single film, the luminous, solar, and thermal properties can be optimized by computation. We also discuss work on In_2O_3:Sn films which are antireflection coated with evaporated magnesium fluoride or with sputtered aluminum oxyfluoride with the aim of boosting the transmittance. Color properties are treated briefly. The review is concluded in Sec. XI with a summary and remarks.

II. FILM PREPARATION

Films of In_2O_3:Sn and In_2O_3 can be prepared by a plethora of techniques, as apparent from the literature cited in the Introduction. Useful descriptions of the most widely used methods have been given especially by Vossen,[4] Jarzebski,[8] and Chopra et al.[11] We have chosen to focus on reactive evaporation. This technique has several advantages: it is capable of yielding films which do not contain significant amounts of uncontrollable contaminants; it is relatively easy to operate; and it involves a minimum of critical process parameters. On the other hand, sputtering may be preferable when very large areas are to be coated. An example of an evaporation unit and deposition procedure are described in Sec. II A. The preparation of In_2O_3:Sn films with optimum optical and electrical performance requires that several interrelated process parameters be chosen correctly. Section II B discusses the preferred values of evaporation rate r, substrate temperature T_s, and pressure P_{ox} of the oxygen atmosphere in which the deposition takes place. Nonreactive deposition of In_2O_3:Sn, followed by a post-treatment in a reducing or oxidizing atmosphere, can be viewed as an alternative to direct reactive deposition. Section II C contains examples of experimental results obtained with heat treatments in air and in Ar + H_2 mixtures. They show that, in fact, reactive deposition is superior. The presentations in Secs. II B and II C rest to some extent on optical measurements; the relevant techniques will be discussed in Sec. IV.

A. Deposition

Most of our discussions are based on films made by a procedure which was first presented by us in Refs. 18–20. We start by describing this procedure in some detail.

The films were made in a versatile deposition system[146] whose most important parts are sketched in Fig. 2. A stainless-steel chamber can be evacuated by an oil diffusion pump with a liquid-nitrogen trap. The starting materials were evaporated from a 10-kW e-beam source operated at 9 kV and a current set to obtain a desired evaporation rate. The source was equipped with an XY sweep, so that the e beam could be continuously swept over the whole hearth. This facility was necessary in order to secure an even deposition of the present
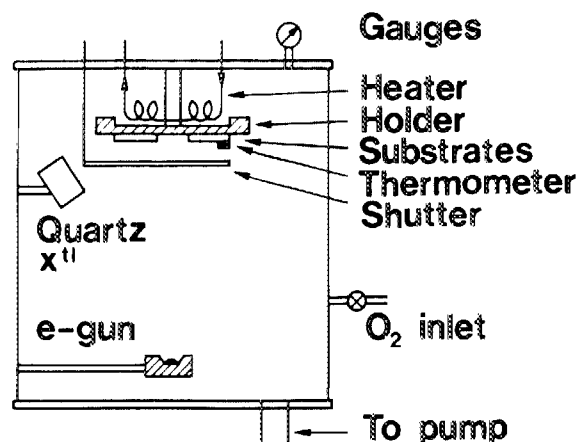

FIG. 2. Schematic view of the evaporation system.

materials. The evaporated species condensed onto substrates positioned 35 cm above the e-beam source. A large shutter covered the substrates except during the depositions. Evaporation in a controlled oxygen atmosphere was possible by a gas inlet through a precision needle valve. A residual gas analyzer was usually connected to the system.

The evaporation rate is a most important parameter for the film quality. The rate was monitored by the use of a vibrating quartz microbalance mounted over the e-beam source. The frequency response of the crystal was converted to deposition rate and ensuing film thickness on a microprocessor-based instrument (Sloan MDC 9000 Deposition Controller) which also adjusted the power delivered to the e-beam source so that a preset deposition rate could be maintained during extended periods of time.

The substrates were held by screws or stainless-steel clamps against a copper plate which could be electrically heated to temperatures up to 400 °C. A Pt 100 resistance thermometer was mounted on top of a reference substrate, placed close to the substrate used for thin-film deposition, in order to secure a realistic measurement of the surface temperature.

The starting materials were hot-pressed pellets of In_2O_3, In_2O_3 + 9 mol % SnO_2, or a mixture of these (obtained from Kyodo International, Japan). The purity was 99.99%. Evaporation took place after evacuation to a base pressure $< 10^{-5}$ Torr. The substrates were Corning 7059 glass, calcium fluoride, silicon, or standard microscope glass slides. All substrates were 1 mm thick. Prior to mounting in the deposition unit, they were cleaned in detergent, rinsed in distilled water, rinsed in alcohol, and dried with a filtered compressed air gun. In order to facilitate later mechanical thickness measurements, a thin strip of stainless steel was clamped over the substrate, thus producing a well-defined step in the coating. Some depositions were also made onto plastic foils and onto carbon-covered copper grids used for transmission electron microscopy studies. The grids were mounted behind a small shutter (not shown in Fig. 2) which could be manipulated without disturbing the deposition onto the substrates.

After having reached proper vacuum and substrate temperature, the evaporation procedure began with 5–10 min of soaking, i.e., heating of the pellets to a temperature slightly less than that needed during the depositions. This was done to remove condensed gases and to establish near-equilibrium conditions in the chamber. The oxygen pressure was then set to the desired value ($\sim 5 \times 10^{-4}$ Torr), as read on a capacitance manometer, at full pump capacity. The power was increased, the main shutter was opened, and film growth took place on the substrate. With a typical deposition rate (0.2 nm/s) and film thickness (0.3 μm), it took ~ 25 min to produce a film. Oxygen pressure and substrate temperature were monitored continuously and adjusted manually if necessary.

B. Process parameters for reactively evaporated coatings

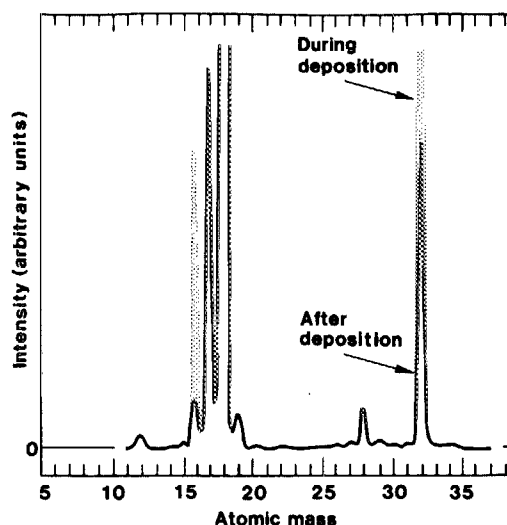When In_2O_3:Sn is evaporated it decomposes slightly into suboxides and free oxygen, which can be documented by

FIG. 3. Mass spectra taken during nonreactive evaporation of In_2O_3:Sn (including the shaded areas) and after evaporation (excluding the shaded areas).

residual gas mass spectrometry performed during a nonreactive deposition and immediately after the same deposition. Figure 3 shows some results obtained by use of the deposition technique outlined above. One finds several peaks which demonstrate that oxygen, water vapor, and carbon-dioxide are the most abundant gases during deposition. The highest peaks, at the atomic masses 18 and 32, correspond to H_2O and O_2, respectively. After deposition there is a dramatic decrease in the peaks at the masses 16 and 32—illustrated by the shaded areas in Fig. 3—whereas the other peaks remain unchanged. This can only be explained as a decrease in the oxygen content. The conclusion is thus that oxygen is liberated during the deposition process.

The oxygen release causes a nonstoichiometry in the films of a magnitude which depends critically on the details of the deposition. It is therefore hardly surprising that very different data have been stated for In_2O_3 and In_2O_3:Sn films prepared by different researchers. It has also been reported[4,106,147] that the properties of such films are thickness dependent, which we believe to be a manifestation of varying deposition conditions. In order to obtain reproducible results and high-quality coatings it is clearly necessary to carefully control the amount of oxygen, which can be done either by oxidation so that a stoichiometric indium oxide structure is produced (and doping is entirely due to tin in the case of In_2O_3:Sn) or by creating a desired oxygen deficiency. Both these types of films can be obtained, in principle, by choosing suitable deposition conditions as well as by postdeposition treatment. For reactive deposition in the presence of oxygen, the majority of the lost oxygen can be regained in the film. The governing parameter is then the relative impingement rate of oxygen molecules onto the surface of the growing film, which, in its turn, is determined by the evaporation rate and the oxygen pressure. Furthermore, the reactivity of the oxygen with the surface is important, which points at the fact that the substrate temperature is another crucial parameter. The temperature also affects the crystallinity of the film.
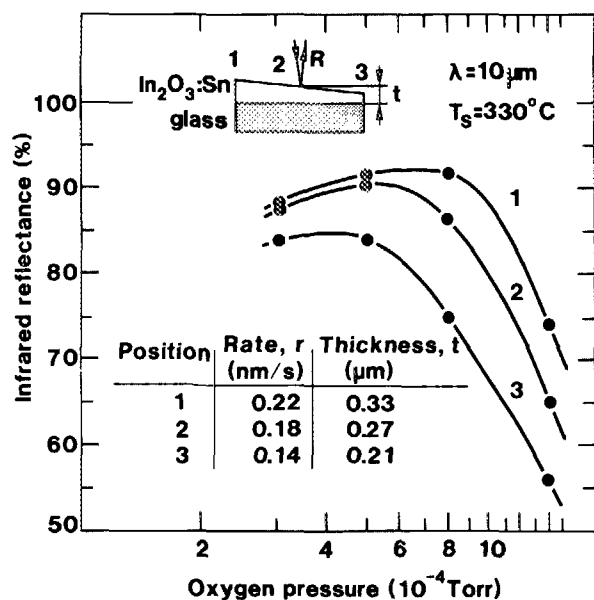
FIG. 4. Infrared reflectance vs oxygen pressure, measured at three positions (denoted by the numbers) for wedge-shaped In_2O_3:Sn films on glass. The experimental configuration is shown in the upper inset. The three sets of data points, joined by curves for convenience, pertain to the shown deposition rates and film thicknesses.

FIG. 5. Infrared reflectance vs substrate temperature for In_2O_3:Sn films on glass. The experimental configuration and process parameters are shown in the inset. The solid curve is drawn only to guide the eye.

Below we elucidate the roles of these three parameters for the optical and electrical characteristics with regard to our deposition technique.[18–20]

Figure 4 shows infrared reflectance at $\lambda = 10\,\mu m$ as a function of oxygen pressure P_{ox} at four different pressures between 3×10^{-4} and 1.4×10^{-3} Torr but otherwise with identical conditions. Evaporation of $In_2O_3 + 9$ mol % SnO_2 was made onto 75×25 mm^2 substrates mounted on the copper plate. Its temperature T_s was kept at 330 °C. The substrate was positioned somewhat off-center on the plate so that a wedge-shaped coating was obtained. At one end the ultimate film thickness t was $0.21\,\mu m$; at the other end it was $0.33\,\mu m$. The corresponding evaporation rates r were 0.14 and 0.22 nm/s, respectively. Optical measurements were conducted at the two extrema of the substrate and also in the middle. The maxima in the curves shown in Fig. 4 yield the optimum magnitudes of P_{ox}. The corresponding reflectance values lie between 85 and 92%; this, however, is entirely a consequence of the varying film thickness and is not relevant for our arguments. Figure 4 proves that the ideal value of P_{ox} is in the 5–8×10^{-4} Torr range for $r \approx 0.2$ nm/s and $T_s \approx 300$ °C. At $P_{ox} \lesssim 3 \times 10^{-4}$ Torr we obtained visually opaque films, which were useless as window coatings, and at $P_{ox} \gtrsim 1.5 \times 10^{-3}$ Torr the filament in the e-beam source burnt out quickly.

The role of T_s for $In_2O_3 + 9$ mol % SnO_2 films is elucidated in some detail in Figs. 5–7. To get comparable data, we have fixed the following parameters: $r = 0.2$ nm/s, $t = 0.3\,\mu m$, and $P_{ox} = 5 \times 10^{-4}$ Torr. Figure 5 shows the infrared reflectance at $\lambda = 10\,\mu m$ for several coatings produced with $70 < T_s < 320$ °C. Good data, i.e., a reflectance of $\sim 90\%$ is found at $T_s \gtrsim 150$ °C. Figure 6 refers to the luminous absorptance A. This quantity is obtained by
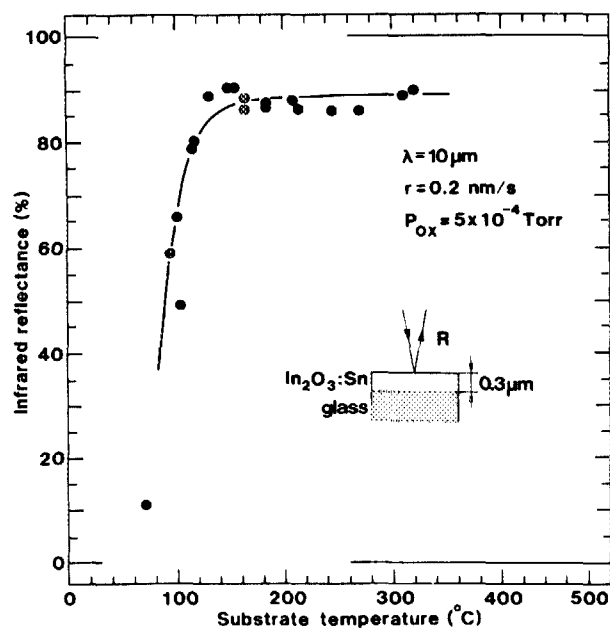
$$A = 1 - R - T,\qquad (1)$$

where R and T are the reflectance and transmittance, respectively, averaged over the 0.5–0.6-μm wavelength interval. The low luminous absorptance demanded in an energy efficient window can only be reached at a high substrate temperature; requiring $A < 5\%$, we are confined to $T_s \gtrsim 150$ °C. At lower temperatures the films look brownish and opaque. At $T_s \sim 300$ °C the absorptance is $\sim 2\%$. This value includes a substrate absorptance of roughly 1%, so the actual film absorptance is down in the 1% range. Figure 7 finally proves that the electrical dc resistivity is low only for $T_s \gtrsim 150$ °C.
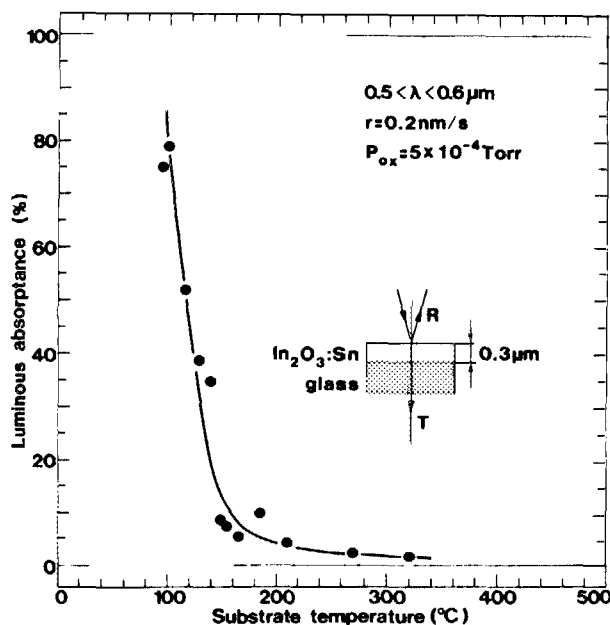

FIG. 6. Luminous absorptance vs substrate temperature for In_2O_3:Sn films on glass. The experimental configuration and process parameters are shown in the inset. The solid curve is drawn only to guide the eye.
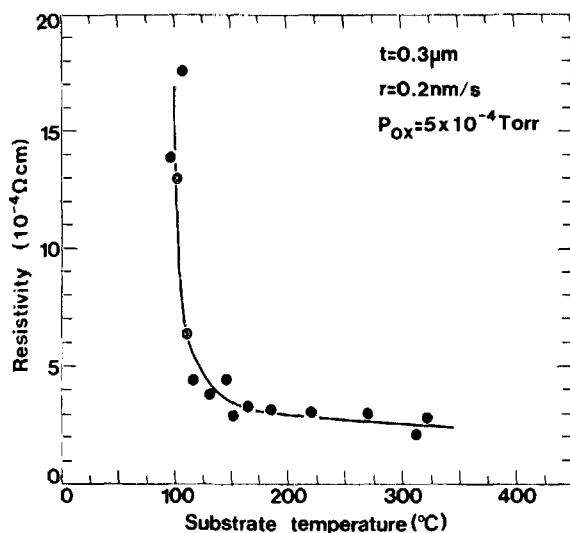
FIG. 7. Electrical resistivity vs substrate temperature for In_2O_3:Sn films on glass. The process parameters are shown in the inset. The solid curve is drawn only to guide the eye.
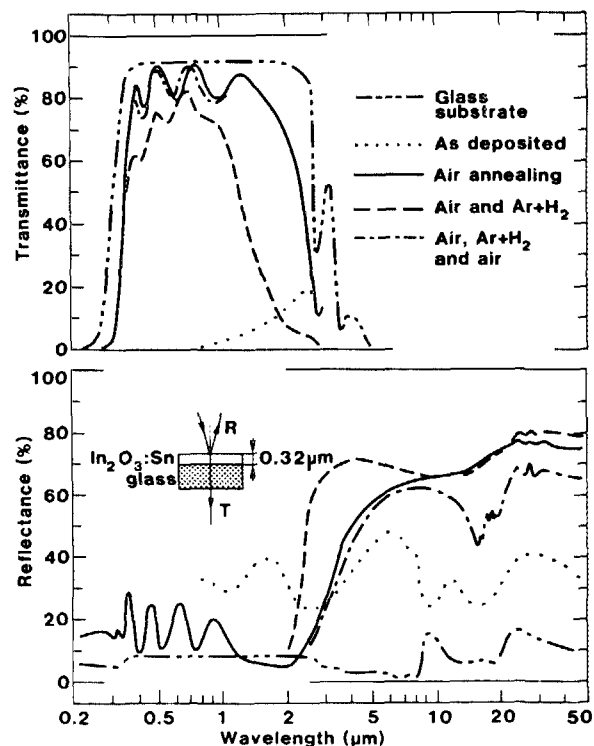

FIG. 8. Spectral transmittance (upper part) and reflectance (lower part) for an uncoated glass substrate and after nonreactive deposition of an In_2O_3:Sn film. The experimental configuration is shown in the inset. Dotted curves refer to the as-deposited film. Solid, dashed, and dash-dotted curves denote results obtained after subsequent heat treatments, each at 440 °C for 2.5 h, in air, in $Ar + H_2$, and again in air.

The common result of these studies is that good film properties can be obtained when the glass temperature is $\gtrsim 150$ °C. It is to be observed that our films were produced with nonassisted evaporation. If the deposition would have been activated by ion bombardment of the growing film—as discussed, for example, by Ebert[17]—it is expected that good film properties could have been reached at considerably lower substrate temperatures.

C. Annealing of nonreactively evaporated coatings

We prepared $In_2O_3 + 9$ mol % SnO_2 films by evaporation without an oxygen inlet in the chamber, but otherwise as described above. These coatings had a brownish or black visual appearance and a poor infrared reflectance. Heat treatments led to the formation of transparent films with moderately high infrared reflectance. The treatments were performed in a temperature-controlled oven having a gas-tight ceramic tube with surrounding heating elements. The gases were either air, Ar, or a 95% Ar + 5% H_2 mixture at normal pressure or slightly above. Annealing at a temperature in the 150–450 °C interval was conducted for 1–3 h.

Figure 8 shows spectral transmittance and reflectance in the $0.2 < \lambda < 50$ μm range. For reference we first show the properties of the Corning 7059 glass substrate; the high and uniform transmittance across the full $0.35 < \lambda < 2.5$ μm interval is noteworthy. Deposition of a 0.32-μm-thick film onto an unheated substrate gave a very low luminous transmittance and an infrared reflectance between 30 and 40%, as indicated by the dotted curves. Annealing in air at 440 °C for 2.5 h led to high transmittance for $\lambda \lesssim 2$ μm and high reflectance for $\lambda \gtrsim 5$ μm. This is shown by the solid curves. As we will find later (cf. Sec. III A), this change can be associated with a structural transformation into a state with large crystallites. The results of a further annealing in Ar + H_2 at 440 °C for 2.5 h—i.e., in a reducing atmosphere—are apparent from the dashed curves. The infrared reflectance is seen to be increased substantially at $2 \lesssim \lambda \lesssim 6$ μm, while the lumi-

nous transmittance is decreased somewhat. This may be explained as a consequence of additional doping through the creation of oxygen vacancies (cf. Sec. III C). Finally, after a new heat treatment in air at 440 °C for 2.5 h, the properties found after the first annealing in air are almost regained. This is seen from the similarity between the dash-dotted and solid curves. The only significant difference is the absorption around $\lambda \sim 15$ μm, which only occurs after the final treatment. Presumably, the oxygen vacancies have been eliminated by oxidation. Annealing of other samples in pure Ar yielded results analogous to those obtained by annealing in air.

We conclude that heat treatments in controlled atmosphere can improve the performance of In_2O_3:Sn and also alter the properties reversibly. Annealing in inert or oxidizing atmosphere gives high luminous transmittance, whereas annealing in reducing atmosphere gives the highest near-infrared reflectance. However, even the best of our nonreactively evaporated coatings do not attain the optical quality which can be reached via reactive evaporation.

III. FILM CHARACTERIZATION

Good characterization of the films is imperative for understanding their optical properties. Section III A contains results from transmission electron microscopy and electron diffraction. The crystallite size is $\gtrsim 50$ nm for In_2O_3:Sn films prepared at $T_s \gtrsim 150$ °C. The crystal structure is treated in Sec. III B, and it is found that the electron diffraction data

are consistent with a C-type rare-earth oxide configuration. Section III C reviews the defect models for In_2O_3:Sn introduced by Frank and Köstlin[87]; this part will be very important in connection with the theory of the optical properties presented in Secs. VI–IX.

A. Grain size

Specimens for transmission electron microscopy were prepared by evaporation onto carbon-covered copper grids according to the procedure in Sec. II. The optimum thickness for obtaining high-resolution micrographs was found to be ~ 40 nm. Most of the studies were made with a Philips EM 300 transmission electron microscope operated at 100 kV and with a magnification of up to $130\,000\times$. The coatings were made with $r = 0.2$ nm/s, $P_{ox} = 5 \times 10^{-4}$ Torr, and $45 < T_s < 320$ °C.

Figure 9 shows bright-field micrographs and diffraction patterns for $In_2O_3 + 9$ mol % SnO_2 coatings prepared at four different substrate temperatures. Figure 9(a), pertaining to $T_s = 45$ °C, indicates a microcrystalline structure. The corresponding diffraction pattern contains only diffuse rings. The coating looked opaque brownish. At $T_s = 160$ °C, Fig. 9(b) shows a crystalline structure with grains having a
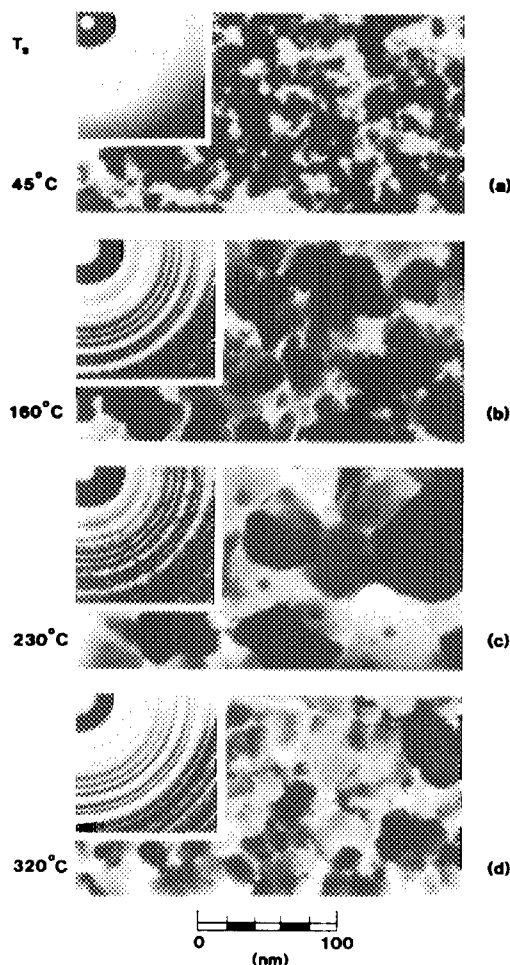
FIG. 9. Transmission electron micrographs and corresponding electron diffraction patterns for In_2O_3:Sn films grown at the shown substrate temperatures.

linear dimension of 10–50 nm. The diffraction pattern displays a large number of distinct rings, proving order over many interatomic distances. We infer that the development of selective optical properties, inherent in Figs. 5 and 6, is connected with an increase in crystal size. The crystallinity is further improved at $T_s = 230$ °C, as apparent from Fig. 9(c). Now the crystallites are ~ 100 nm in size, and the diffraction pattern is very distinct. At still higher temperatures the crystallites seemed to be smaller; cf. Fig. 9(d). The reason for this unexpected shrinkage is not known; possibly different values of P_{ox} are required for maximum grain size in films grown at different substrate temperatures.

Figure 10 shows a micrograph and a diffraction pattern for an In_2O_3 film prepared at $T_s = 245$ °C. The crystallites are ~ 50 nm in diameter and rather uniform. Comparing Figs. 9 and 10, it appears that the $In_2O_3 + 9$ mol % SnO_2 and the pure In_2O_3 films look almost identical.

A JEOL 200-kV scanning transmission electron microscope was used in scanning mode to investigate the surface structure of films with different thicknesses but produced under identical conditions. The surface structures were found to be almost indistinguishable, indicating that the microscopy studies of 40-nm-thick specimens are adequate also for the order-of-magnitude thicker films employed in the optical work. The same instrument was used for x-ray point (diameter ~ 7 nm) analysis of small grains and near grain boundaries. In no case could we detect any difference from the average composition.

Compositional depth profiles of indium, tin, and oxygen were recorded by use of Auger electron spectroscopy combined with sputtering. The indium and tin signals were found to be constant, whereas the oxygen signal decreased somewhat with depth. The variation is small and is regarded as insignificant.

In principle, the film growth is influenced by the kind of substrate used, and one may ask whether our films on amorphous carbon, glass, CaF_2, and Si have identical properties. A completely conclusive answer cannot be given, but we note that films stripped from NaCl (Refs. 82 and 148) and KCl (Ref. 14) looked very similar to our films made on amorphous carbon, and hence the substrate conditions are
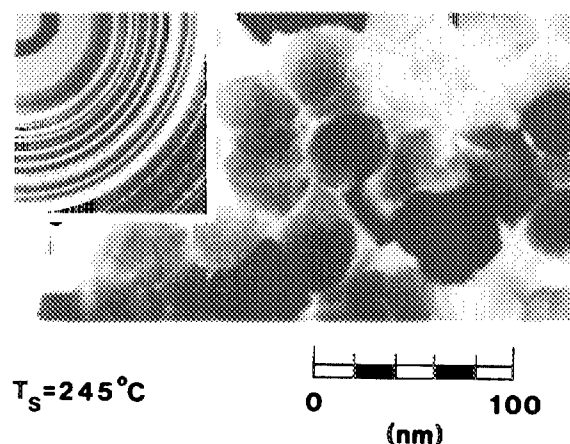
FIG. 10. Transmission electron micrograph and corresponding electron diffraction pattern for an In_2O_3 film grown at 245 °C.

not expected to be critical. We also remark that at very high substrate temperature—above 500 °C, for example—there can be a significant diffusion of ions from the substrate into the film. This effect is not believed to be important at $T_s \lesssim 300$ °C.

B. Crystal structure

At normal pressure In_2O_3 crystallizes in a cubic structure of the bixbyite $Mn_2O_3(I)$ type (also called the C-type rare-earth oxide structure, space group T_h^7 $Ia3$).[149,150] The lattice parameter is 1.0117 nm and the density is 7.12 g/cm³. The coordination is sixfold for the In atoms and fourfold for the O atoms. To visualize the structure, we note that there are two crystallographically nonequivalent In sites. One of these is associated with an In-O separation of 0.218 nm and O atoms lying nearly at the corners of a cube with two body-diagonally opposite corners unoccupied; the other is associated with nonequal In-O separations being 0.213, 0.219, and 0.223 nm (average 0.218 nm) and O atoms lying nearly at the corners of a cube with two face-diagonally opposite corners unoccupied. A hexagonal structure of In_2O_3 occurs at high pressure[150]; it is not normally detected in thin films.

Figures 9 and 10 present diffraction patterns for In_2O_3:Sn and In_2O_3 films prepared by our technique.[18-20] They are consistent with the C-type rare-earth oxide structure. Figure 11 displays a magnification of part of a diffractogram. It was taken on an $In_2O_3 + 9$ mol % SnO_2 film, but indistinguishable data were recorded for In_2O_3. The (hkl) indices for the reflections are shown. Most of the reflections agree with bulk data for cubic In_2O_3 (ASTM Card 6-0416), but we note the occurrence fo four "extra" rings corresponding to (110), (200), (220), and (310). They ought to be extinct in th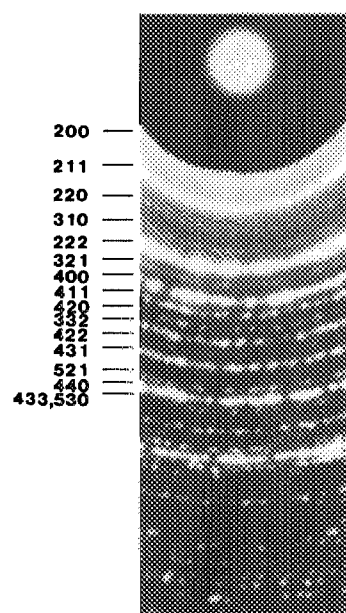e bulk, although the (200) and (220) have in fact been observed[149] by x-ray diffraction from single crystals. The four "extra" reflections were seen also in recent work by Ovadyahu et al.[25] on e-beam evaporated In_2O_3. Their significance remains unknown. The shown diffractograms are inconsistent with hexagonal In_2O_3 (22-336; 21-406), In_2SnO_5 (32-458), SnO (24-1342; 6-0395; 13-111; 7-195), SnO_2 (21-1250; 29-1484), Sn_3O_4 (20-1293; 16-737), $SnO \cdot SnO_2$ (25-1259), In (5-642), Sn (5-0390; 4-0673), and In-Sn (7-396; 7-345), where the pertinent ASTM card numbers are given in parantheses. Each diffraction ring has a uniform brightness, and thus there is no evidence for preferred orientation in the shown data. Different kinds of perferred orientation have been reported in Refs. 8 and 99.

C. Defect models

The optical properties of the spectrally selective In_2O_3 films are governed by *defects* introduced in the C-type rare-earth oxide structure. Here we summarize recent work by Frank and Köstlin[99] on this issue. They carried out extensive experiments and analyses on films with varying Sn contents prepared by chemical vapor deposition (spray pyrolysis) and treated in oxidizing and reducing atmospheres.

We first consider In_2O_3. Under reducing conditions some oxygen is lost and the ensuing material can be described, using standard notation,[151] as

$$In_2O_{3-x}(V_0^-)_x \, e'_{2x} , \tag{2}$$

with $x \lesssim 0.01$. V_0^- denotes doubly charged oxygen vacancies, and e' denotes electrons which are needed for charge neutrality on a macroscopic scale.

When adding small amounts of Sn to In_2O_3, the Sn atoms enter substitutionally in the cation sublattice. Hence we have Sn^{4+} replacing In^{3+} and acting as n-type donors; a suggestion[70] that Sn^{2+} is incorporated has not been substantiated by experiments.[83] The material may be described by

$$In_{2-y} \, Sn_y^- \, O_3 \, e'_y . \tag{3}$$

Here we have neglected the oxygen vacancies, which is adequate when the Sn content exceeds a few percent. Expression (3) is believed to give a good representation o the $In_2O_3 + 9$ mol % SnO_2 films reported above, and hence each Sn atom can be taken to contribute one electron. The electron density inherent in expressions (2) and (3) can lead to metalliclike reflectance at long wavelengths which is required for a window coating.

At higher Sn contents there are also three other types of defects: an ionizable $(Sn_2^- \, O_i'')$ complex involving an interstitial O atom loosely bound to two Sn atoms; a nonionizable $(Sn_2O_4)^x$ complex composed of two nearby Sn atoms which strongly bind three closest O atoms together with an additional O atom; and a $(Sn_2^- \, O_i'') (Sn_2O_4)^x$ associate. They are expected to play a marginal role, at most, for the films discussed in this review. The model by Frank and Köstlin does not involve other defects; we observe, however, that interstitial In atoms have been discussed in some recent work.[25,110]

FIG. 11. Electron diffractogram for an In_2O_3:Sn film on amorphous carbon. Calculated positions of several reflections for cubic In_2O_3 are shown (the 110 reflection is omitted, since it is not clearly seen on the photo). The innermost part of the pattern was shadowed during most of the exposure.

IV. MEASURED ELECTROMAGNETIC PROPERTIES

This section is devoted to measured optical and electrical data. The majority of these will be used as input in the

evaluations in the subsequent sections. Section IV A presents spectrophotometric techniques used to obtain transmittance T and reflectance R in the $0.2 < \lambda < 50 \, \mu m$ interval—including the solar and thermal ranges— and also gives illustrative examples of these data. In particular, we note how the semiconductor band gap (in the ultraviolet), the luminous transmittance, the infrared reflectance, and the phonon-induced absorption (at $15 \lesssim \lambda \lesssim 30 \, \mu m$) are influenced by the Sn content. Section IV B gives results on resistivity ρ and mobility μ determined from dc electrical measurements and Hall-effect measurements. Section IV C contains a complementary study of the microwave reflectance, which is found to correlate well with the infrared reflectance. The coatings discussed in Sec. IV, and also in the remainder of this review, were produced with the following parameters; $r = 0.2 \, nm/s$, $T_s \approx 300 \, °C$, and $P_{ox} \approx 5 \times 10^{-4}$ Torr.

A. Spectrophotometry: Techniques and illustrative results

This section reviews typical spectral transmittance and reflectance data for e-beam evaporated In_2O_3:Sn films. For specificity, we describe the techniques used in our own work[18–22,27–32] and some typical results obtained by applyng these.

In the $0.2 < \lambda < 2.5 \, \mu m$ interval we used a Beckman ACTA MVII double-beam spectrophotometer equipped with polarizers. Variable-angle attachments were employed both for transmittance and reflectance. To record R, we used an MgF_2-coated Al mirror in the reference beam and either the specimen under study or an additional MgF_2-coated Al mirror in the sample beam. Apertures were sometimes used to diminish the investigated area of the films; this was necessary for films having a nonuniform thickness. Accurate calibration of the Al mirrors is imperative. This was achieved through two techniques: by measuring their absolute reflectance on a v-w reflectometer, or by comparing them to freshly evaporated Au, Ag, or Al mirrors whose optical properties were taken to be given by literature data.[152,153] Total and diffuse reflectance were measured by attaching a $BaSO_4$-coated integrating sphere to the spectrophotometer. The diffuse component was $< 0.5\%$ for all of the investigated films, and hence they can be regarded as fully specular.

In the $2.5 < \lambda < 50 \, \mu m$ interval we used a Perkin-Elmer 580 B double-beam spectrophotometer with polarizers and air dryer. Variable-angle reflectance was measured with Al- or Au-coated mirrors as reflectance standards.

A data acquisition and handling system was developed to facilitate accurate readings from the spectrophotometers and for using these results in later analysis. The spectrophotometers were interfaced to a Hewlett Packard 1000 computer and were normally run from the computer keyboard. Each recorded spectrum was normalized with regard to 0% and 100% lines. By correcting for the reference mirror, we obtained data of generally better than 1% accuracy. Mutually connected spectra for T and R were stored together in the computer. The sampling interval was different for different spectral ranges: at $0.2 < \lambda < 0.4 \, \mu m$ it was 2 nm, at $0.4 < \lambda < 0.8 \, \mu m$ it was 5 nm (or sometimes more), and at
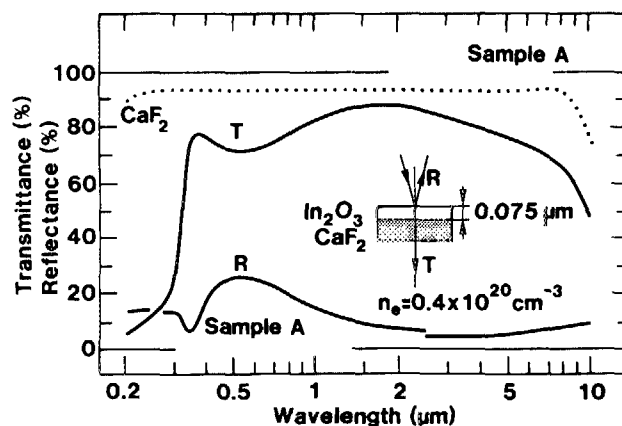

FIG. 12. Spectral normal transmittance and near-normal reflectance (p-polarized light) for an In_2O_3 film, having the shown thickness and electron density, backed by CaF_2. The dotted curve refers to the transmittance of the bare substrate. The angle of incidence in the reflectance measurement was $10°$ for $\lambda < 2.5 \, \mu m$ and $25°$ for $\lambda > 2.5 \, \mu m$. The experimental configuration is shown in the inset.

$0.8 < \lambda < 2.5 \, \mu m$ it was usually 20 nm; for $2.5 < \lambda < 50 \, \mu m$ we stored the spectrophotometric data versus wave number ($1/\lambda$) with a typical sampling interval of 10 or 20 cm^{-1}. A complete spectrum thus normally comprised more than 500 data points.

Figures 12–14 show spectral transmittance and reflectance of films deposited onto 1-mm-thick CaF_2 plates. The scatter in the data was usually less than the widths of the graphs. The transmittance of the bare substrate is indicated by the dotted curve in Fig. 12; it is seen to be $\sim 90\%$ for $0.2 \lesssim \lambda \lesssim 8 \, \mu m$ and to fall off at larger wavelengths. Reliable film data could be recorded at $\lambda \lesssim 10 \, \mu m$. The solid curves in
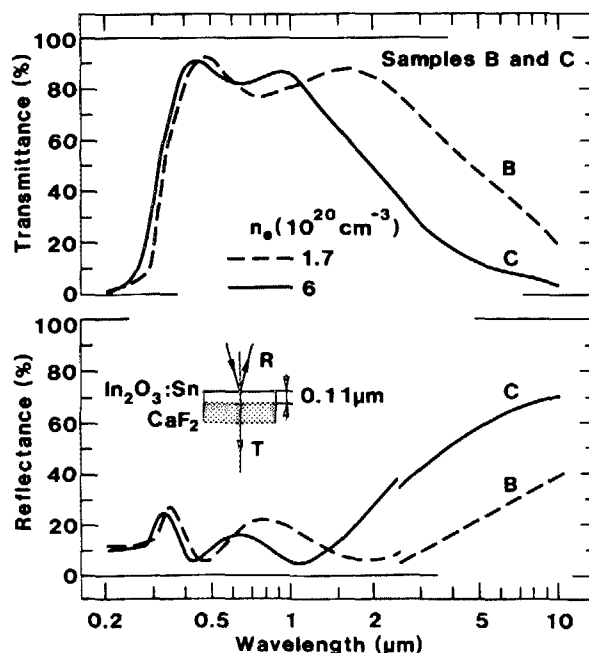

FIG. 13. Spectral normal transmittance (upper part) and near-normal reflectance (lower part; p-polarized light) for CaF_2 coated with In_2O_3:Sn films having the shown thickness and electron densities. The angle of incidence in the reflectance measurement was $10°$ for $\lambda < 2.5 \, \mu m$ and $25°$ for $\lambda > 2.5 \, \mu m$. The experimental configuration is shown in the inset.

FIG. 14. Spectral normal transmittance and near-normal reflectance (p-polarized light) for CaF$_2$ coated with an In$_2$O$_3$:Sn film having the shown thickness and electron density. The angle of incidence in the reflectance measurement was 10° for $\lambda < 2.5\,\mu$m and 25° for $\lambda > 2.5\,\mu$m. The experimental configuration is shown in the inset.
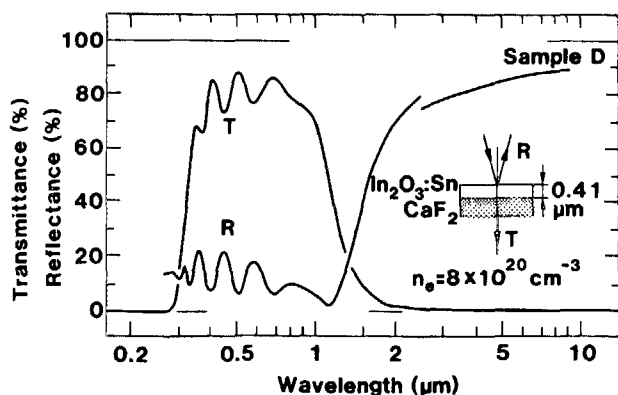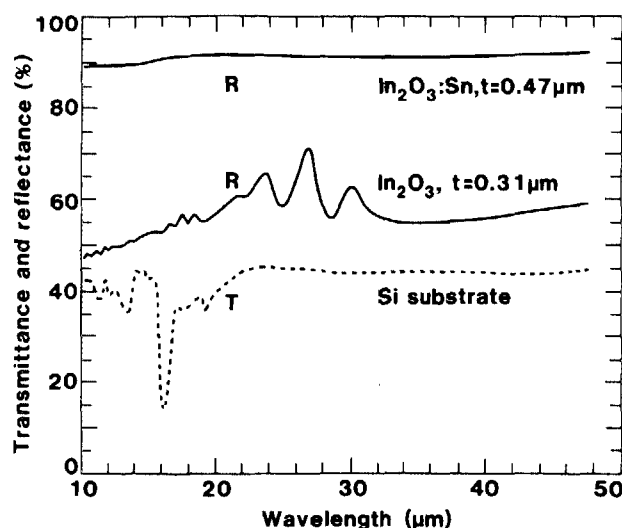

FIG. 15. Spectral normal transmittance for a Si plate and near-normal reflectance (25° angle of incidence; p-polarized light) for Si coated with In$_2$O$_3$ or In$_2$O$_3$:Sn films having the shown thicknesses.

Fig. 12 pertain to a 0.075-μm-thick In$_2$O$_3$ film (denoted sample A for future reference). Oxygen vacancies yield some n doping, as outlined in Sec. III C. The ensuing density of free electrons n_e is 0.4×10^{20} cm^{-3}; the determination of this important quantity will be elaborated in Sec. V C. At $\lambda > 0.4$ μm the transmittance varies smoothly around 80% and the reflectance varies around 10%. The large decrease in T at $\lambda < 0.4\,\mu$m is due to absorption at the semiconductor band gap.

Figure 13 shows T and R for two In$_2$O$_3$:Sn films, each being 0.11 μm thick. The dashed and solid curves (samples B and C) correspond to coatings doped through interstitial Sn atoms so that n_e was 1.7 and 6×10^{20} cm^{-3}, respectively. Sample C was produced by evaporation of In$_2$O$_3$ + 9 mol % SnO$_2$, whereas sample B was produced with less SnO$_2$ present in the evaporation material. It is found that an increase of the Sn content (or of n_e) causes an increase of the infrared reflectance and a concomitant decrease of the infrared transmittance, while the luminous performance is rather unaffected. We note that the band gap appears to be shifted towards the ultraviolet when the doping is increased.

The infrared reflectance shown in Fig. 13 is undesirably low for window applications even for the film with the highest electron density, and it is of practical interest to investigate thicker coatings. Figure 14 reports on T and R for a 0.41-μm-thick In$_2$O$_3$ + 9 mol % SnO$_2$ film (sample D) with $n_e = 8 \times 10^{20}$ cm^{-3}. Now the reflectance is high in the thermal range, while the luminous transmittance remains quite high. Several interference maxima and minima lie in the visible part of the spectrum, and it is evident that this coating is prone to display color.

Figure 15 reports spectral optical properties at $10 < \lambda < 50\,\mu$m for films on 1-mm-thick Si plates. The scatter in the data was insignificant at $\lambda \lesssim 40\,\mu$m. The transmittance of the uncoated substrate, given by the dotted curve, is $\sim 45\%$ except at $\lambda \approx 16\,\mu$m where a moderately strong absorption takes place. The solid curves pertain to reflectance from a 0.31-μm-thick In$_2$O$_3$ film and from a 0.47-μm-thick In$_2$O$_3$ + 9 mol % SnO$_2$ film. The heavily doped In$_2$O$_3$:Sn coating displays a featureless reflectance of $\sim 90\%$ in the

entire spectral range. The lightly doped In$_2$O$_3$ coating has an overall reflectance of $\sim 60\%$ and shows a reproducible structure with several peaks and dips at $15 \lesssim \lambda \lesssim 30\,\mu$m. We will find in Sec. IX that this structure is associated with phonon absorption, which is clearly seen only if the electron density is not too large.

B. Resistivity and mobility

Resistivity and mobility can be determined by dc electrical measurements and by Hall-effect measurements. The dc resistivity of the films discussed in the previous section was obtained by pressing fine indium wires against the coated substrates with a distance between the wires equal to the width of the coated area. Measurements were thus made on a true square. The recorded resistance $R_\square$ is related to the resistivity ρ_c by

$$\rho_c = R_\square t . \tag{4}$$

Earlier ρ_c was used to optimize the deposition parameters (cf. Fig. 7). The conduction mobility μ_c can be found, provided that the electron density is known from independent measurements, by

$$\mu_c = (\rho_c e n_e)^{-1} . \tag{5}$$

Values of ρ_c and μ_c, obtained at room temperature, are included in Table I. Cooling to 77 K made ρ_c go down by 5–10%, and we infer that the films consist of highly degenerate semiconductors.

Resistivity, mobility, and electron density can be found also from Hall-effect measurements (subscript H denotes these results). The samples used in this work were coated CaF$_2$ plates, 4×4 mm^2 in size, with small evaporated silver contacts in the four corners. The van der Pauw technique[154] in a magnetic field of 0.5 T was used to obtain ρ_H and the Hall constant R_H. The samples were n type and the electron density was found from

$$n_{eH} = f_H / e R_H , \tag{6}$$

TABLE I. Data for films of In_2O_3 (sample A) and In_2O_3:Sn (samples B–D). Results are given on thickness (t), resistance per square ($R_\square$), electron density (n_e), resistivity (ρ), and mobility (μ). Quantities based on dc electrical measurements and Hall-effect measurements are indicated by subscripts c and H, respectively. When two values are given for the Hall-effect data, these were obtained for different parts cut out from the same sample.

Sample	t (μm)	$R_\square$ (Ω)	n_e (10^{20} cm^{-3})	ρ_c (10^{-4} Ω cm)	μ_c (cm^2/V s)	n_{eH} (10^{20} cm^{-3})	ρ_H (10^{-4} Ω cm)	μ_H (cm^2/V s)
A	0.075	230	0.4	17	91	0.46	18	78
B	0.115	80	1.7	9.2	40	1.1–1.2	6.8–7.2	77–79
C	0.11	27	6.2	3.0	34	4.7	3.0	45
D	0.41	6.7	8.0	2.8	29	5.5–8.6	1.9–2.0	43–60

where f_H is a factor which depends on the type of scattering[155] and also on the degree of degeneracy in the semiconductor. For complete degeneracy one may put $f_H = 1$. The Hall mobility μ_H was obtained from a relation analogous to Eq. (5). Table I gives room-temperature data on ρ_H, μ_H, and n_{eH} (with $f_H = 1$). After cooling to 77 K, ρ_H was reduced by 8–12%.

Table I shows that the resistivity can be as low as $\sim 2 \times 10^{-4}$ Ω cm at the highest doping levels (corresponding to an electron density of $\sim 10^{21}$ cm^{-3}). The Hall mobility is ~ 80 at low doping and is reduced by a factor ~ 2 at high doping. The results reported here are in good general agreement with the data summarized in Refs. 8–11. The estimated accuracy[156] in the Hall-effect data is 2% for ρ_H, 15% for μ_H, and 25% for n_{eH}. The first value is dominated by uncertainties in film thickness determination, while the latter two are dominated by the sizes of the silver contacts. An alternative optical technique to obtain the electron density will be described in Sec. V C.

C. Microwave reflectance

To complement the optical data for In_2O_3:Sn films, we report the microwave reflectance in the 6.5–13 GHz range. The specimen was mounted at the end of an X-band waveguide, and the reflected intensity was determined by use of an automatic network analyzer interfaced to a computer. Figure 16 shows reflectance as a function of frequency for a bare glass substrate and for glass coated with two In_2O_3:Sn films having different square resistances. The film with $R_\square = 11$ Ω is seen to have a reflectance of $\sim 90\%$, while the film with $R_\square = 88$ Ω has a reflectance of $\sim 55\%$. These results correlate well with the long-wavelength optical reflectance data for films with comparable $R_\square$ values, as seen from Figs. 13 and 14 and from Table I.

No detailed analysis of the microwave reflectance will be given. However, we note that in the limit of long wavelengths one can write[157]

$$R = (1 + 2R_\square/Z_0)^{-2}, \tag{7}$$

where $Z_0 = 377$ Ω is the impedance of free space. For $R_\square = 11$ and 88 Ω we find $R = 89$ and 46%, respectively, which proves that the results on electrical resistance and microwave reflectance are internally consistent.

V. DIELECTRIC FUNCTIONS

Spectral transmittance and reflectance data for thin films, such as those shown in Figs. 12–15, can be used to derive the complex dielectric function $\epsilon \equiv \epsilon_1 + i\epsilon_2$, or, equivalently, the complex refractive index $N \equiv n + ik$ of the coating material. These functions contain basic information on the optical properties and are needed both for reliable comparison with theory and for optimizing the performance of a window coating. The real and imaginary parts of the dielectric function (ϵ_1 and ϵ_2) are related to the optical constants (n and k) by

$$\epsilon_1 = n^2 - k^2, \tag{8}$$

$$\epsilon_2 = 2nk. \tag{9}$$

In principle, ϵ_1 and ϵ_2 (or n and k) can be obtained from any two independent spectrophotometric recordings by use of Fresnel's equations.[158,159] In practice, though, experimental uncertainties in the spectrophotometric data can cause uncertainties in ϵ_1 and ϵ_2 to an extent that the evaluated dielectric function is useless. Techniques to obtain accurate values for ϵ_1 and ϵ_2 are elaborated in Sec. V A with particular regard to the selection of appropriate input data. Section V B reports typical data on ϵ_1 and ϵ_2 for In_2O_3 and In_2O_3:Sn films with different electron densities. The numerical accuracy and internal consistency are treated. Section V C gives a preliminary analysis of the data in terms of the Drude theory.

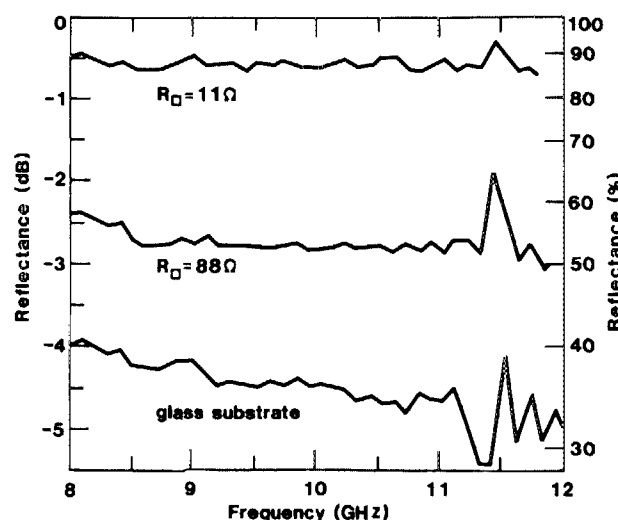

FIG. 16. Microwave reflectance (on a linear dB scale) vs frequency for a bare glass substrate and for glass coated with In_2O_3:Sn films having the shown values of resistance per square. The individual data points are joined by straight lines.

We present ϵ for "undoped" In_2O_3 and discuss the evaluation of electron density from optical measurements.

A. Techniques

It is not practical to use analytic techniques to compute ϵ_1 and ϵ_2 from measured transmittance and reflectance or any other combination of spectrophotometric data. Instead the desired information can be obtained by minimization of a function[146,160]

$$F(\epsilon_1,\epsilon_2) \equiv |X_{comp}^{(1)} - X^{(1)}| + |X_{comp}^{(2)} - X^{(2)}|, \qquad (10)$$

where X is the spectrophotometric quantity (T or R), and the subscript "comp" denotes the result of a computation for the pertinent experimental configuration, viz., a thin film of thickness t and dielectric function ϵ backed by a substrate whose optical properties are taken to be known. The calculations are based on amplitude ratios for transmittance and reflectance at the air/film, film/substrate, and substrate/air interfaces obtained by Fresnel's equations[158,159] for given angle of incidence and state of polarization. Multiple reflections must be allowed for both in the film and in the substrate. Under practical conditions, the coherence length inherent in the optical measurements is always much larger than t and much less than the substrate thickness, and hence one can include interference in the film through summation of amplitudes, and exclude interference in the substrate through summation of intensities. A weak absorption in the substrate can be incorporated in the formalism[156] through an empirical attenuation factor. This extends the useful range for the substrates (cf. Figs. 12 and 15) and, for example, it is not impossible to work with Si in the whole thermal infrared range.

The minimization of F in Eq. (10) is conveniently performed by first estimating reasonable start values for ϵ_1 and ϵ_2 and then using a two-dimensional Newton–Raphson iteration scheme to obtain the correct solution. A computer-based data acquisition system, such as the one mentioned in Sec. IV A, is of great help to derive ϵ as a function of λ. In our own work, an evaluation at 100 discrete wavelengths could be obtained automatically in a few minutes.

The selection of "good" spectrophotometric input data to derive ϵ is an old problem. A recent discussion has been given by McPhedran et al.[161] There are innumerable options as to the choice of transmittance and/or reflectance, the angle of incidence, the polarization, and the film thickness. Curves of constant T and R, or other combinations, plotted in the complex (n,k) plane, are important for judging the usefulness of a certain combination of input data.[160–163] The technique is "good" when curves corresponding to different parameter values ($R = 10$ and 15%, for example) lie close to one another, and the grids pertaining to T and R, intersect under near-90° angles. Normal transmittance combined with near-normal reflectance is widely used,[162] but this technique is notoriously bad when $n \approx k + 1$. Another method, which is often of considerable value, is to combine normal transmittance with reflectance for a film on a metallized substrate.[160,163]

Figure 17 gives an example of the usefulness of plots in the (n,k) plane. Normal transmittance for $t/\lambda = 0.013$ (for
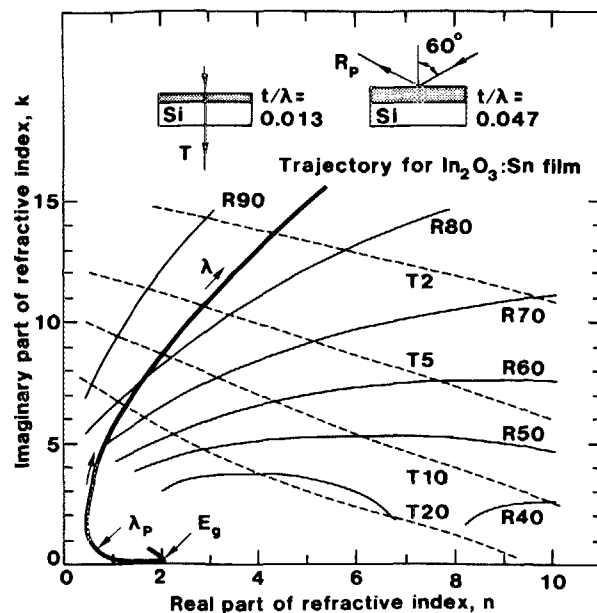

FIG. 17. Contours of constant transmittance at normal incidence and constant reflectance of p-polarized light at 60° angle of incidence drawn in the (n,k) plane. The studied configurations are indicated in the upper part of the figure. The designations of the thin solid and dashed curves indicate the magnitude (in percent) of the transmittance and reflectance. The thick solid curve shows the trajectory gone through for a heavily doped In_2O_3:Sn film as the wavelength is increased. The curve starts in the ultraviolet with $(n,k) \approx (1.6,0.6)$ and evolves with decreasing k, passing through the wavelength for the semiconductor band gap E_g, into the visible with k values as low as 0.005. Then k increases towards the near infrared and passes the plasma wavelength λ_p (given by $\epsilon_1 = 0$, i.e. $n = k$). Finally, the trajectory evolves rapidly in the infrared to large values of n and k, which are indicative of metalliclike properties.

example, a 0.13-μm-thick film at $\lambda = 10\ \mu$m) is combined with reflectance for $t/\lambda = 0.047$ of p-polarized light with 60° angle of incidence. The films are backed by Si (refractive index 3.4). Curves corresponding to different values of transmittance and reflectance are shown. s-polarized light at 60° gave reflectance curves about three times wider apart, proving that p polarization yields higher accuracy. The thick curve in Fig. 17 indicates the trajectory which is gone through for a heavily doped In_2O_3:Sn film as the wavelength is increased from the ultraviolet into the thermal infrared. The major part of the trajectory pertains to large values of n and k, i.e., to metalliclike film properties. It is readily seen that the chosen combination of optical data is capable of producing accurate magnitudes of n and k for such films.

An accurate determination of the film thickness is essential for the derivation of ϵ. In Sec. II A we mentioned measurements by an oscillating quartz microbalance and by a mechanical stylus instrument. Both techniques give important information on t, but normally the accuracy is not high enough, and it is necessary to employ supplementary optical methods. These also have the advantage of yielding t precisely for the area of the film used to find ϵ.

There are several useful optical techniques; three of them will be mentioned here. The first one is based on a generalization of Eq. (10). The thickness is obtained from a
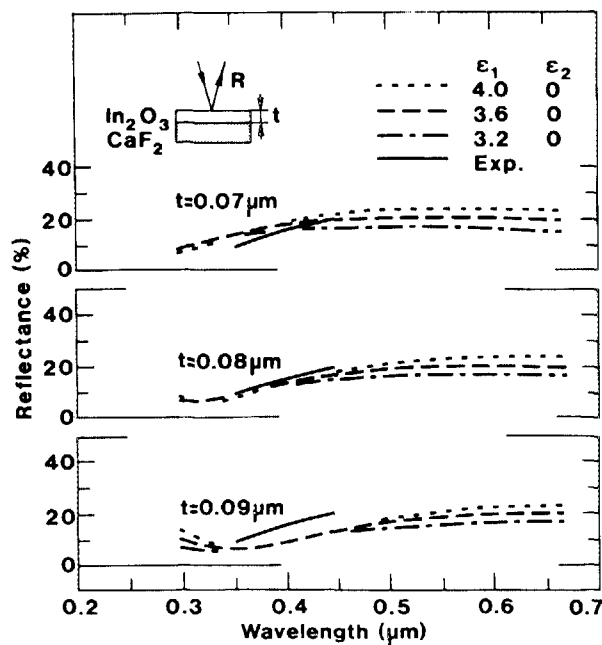
FIG. 18. Measured and computed spectral reflectance at 10° angle of incidence for an In_2O_3 film on CaF_2. The shown values of ϵ_1 and t were used in the calculations. Theoretical curves are partly overlapping, especially for $t = 0.09\ \mu m$. Experimental results for a more extended wavelength range were given in Fig. 12.

minimization of the function

$$F'(\epsilon_1, \epsilon_2; t)$$

$$\equiv |X_{comp}^{(1)} - X^{(1)}| + |X_{comp}^{(2)} - X^{(2)}| + |X_{comp}^{(3)} - X^{(3)}|,$$
$$(11)$$

comprising three independent optical measurements. This gives t as a function of wavelength, and the preferred thickness can then be taken as an average value from those wavelength ranges which are judged to produce the most reliable results.

The second technique, which is applicable to thick films, is based on the locations for maxima and minima of T and R in the wavelength interval where the films are weakly absorbing.

The third technique, useful for thin films, employs straightforward calculations of reflectance within certain ranges. Figure 18 illustrates its usefulness. The solid curves for $0.35 < \lambda < 0.45\ \mu m$ show measured reflectance for an In_2O_3 film. The dashed and dotted curves were computed for nonabsorbing films characterized by $\epsilon_1 = 3.2$, 3.6, and 4.0 and having $t = 0.07$, 0.08, and 0.09 μm. It is apparent that the calculated reflectance is only weakly dependent on ϵ_1 for $0.35 < \lambda < 0.45\ \mu m$, and it is easy to find a reliable value for t equal to 0.075 μm.

B. Data

Figures 19–22 present evaluated dielectric functions for In_2O_3 and In_2O_3:Sn on a logarithmic scale for photon energy $\hbar\omega$. Both ϵ_1 and ϵ_2 vary over several orders of magnitude. The solid curves represent "best data." For $\lambda \lesssim 10\ \mu m$ these are based on spectrophotometric measurements on the specimens A–D, whose normal transmittance and near-nor-
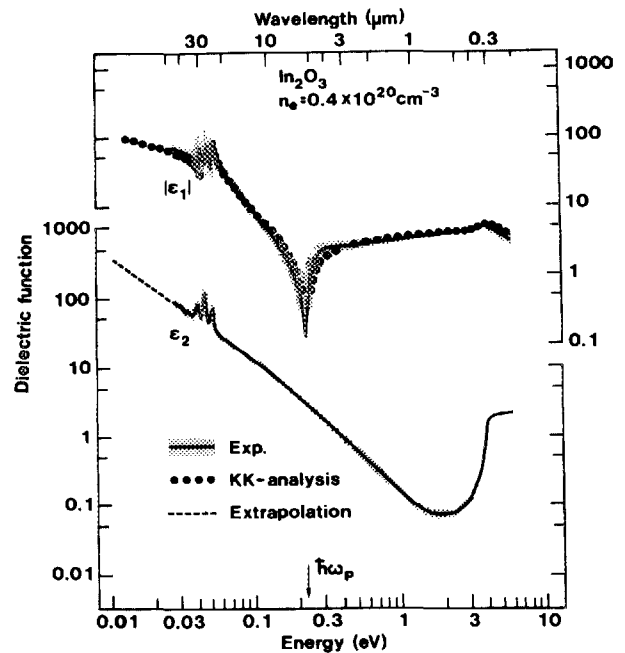

FIG. 19. Real and imaginary parts of the dielectric function for In_2O_3 films. Solid curves denote the evaluation, which is estimated to be accurate to within the shaded areas. Filled circles in the upper part shows results for ϵ_1 obtained from a Kramers–Kronig (KK) analysis of the measured ϵ_2 together with the extrapolation indicated by the dotted curve. The electron density (n_e) and plasma energy $(\hbar\omega_p)$ are indicated. The data were obtained with films deposited onto CaF_2 (sample A; cf. Fig. 12) and Si.

mal reflectance were shown in Figs. 12–14. Supplementary measurements on similar films deposited onto Si were used to extend some of the data to $\lambda > 10\ \mu m$.

The dielectric functions show a consistent pattern. An *absorbing region* is found in the ultraviolet ($\hbar\omega \gtrsim 4$ eV),

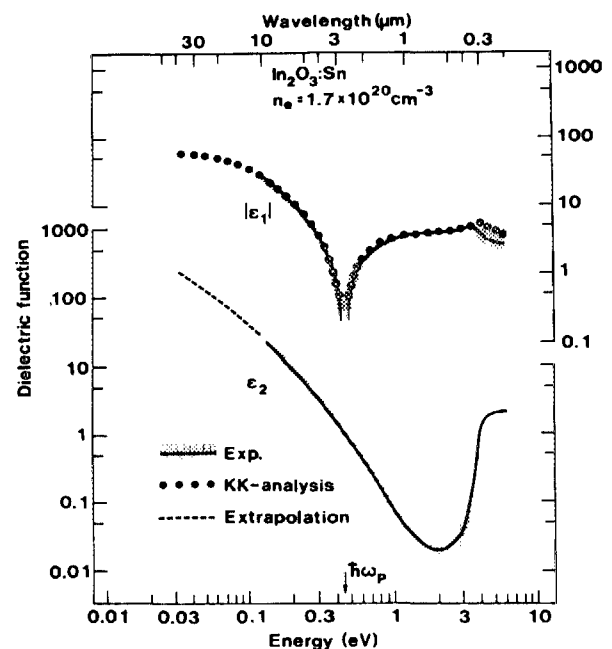FIG. 20. As in Fig. 19, but for In_2O_3:Sn films obtained by deposition of $In_2O_3 + SnO_2$ onto CaF_2 (sample B; cf. Fig. 13).

R135   J. Appl. Phys., Vol. 60, No. 11, 1 December 1986

I. Hamberg and C. G. Granqvist   R135
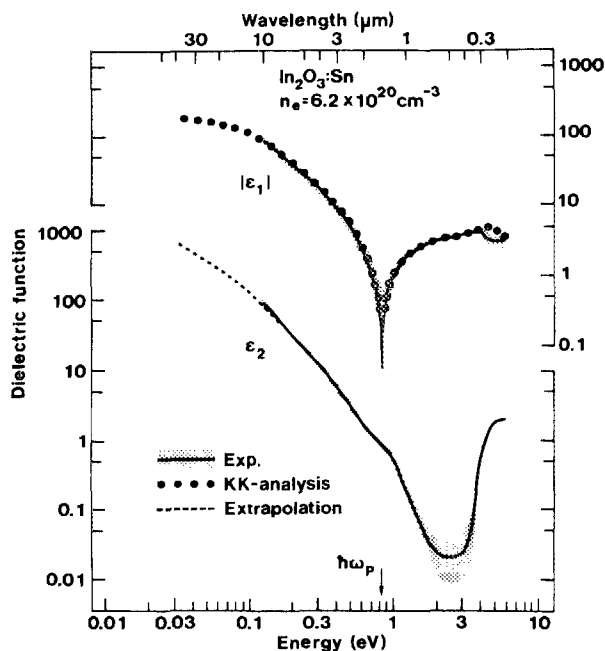
FIG. 21. As in Fig. 19, but for In_2O_3:Sn films obtained by deposition of $In_2O_2 + SnO_2$ onto CaF_2 (sample C; cf. Fig. 13).

where we have, roughly, $\epsilon \approx 4 + i2$. The absorption is associated with excitations across the fundamental semiconductor band gap. At somewhat lower energies there is a rapid drop in ϵ_2 to values which can be as low as ~ 0.01, and a concomitant small peak in ϵ_1. The decrease in absorption leads to a *transparent region* which prevails in the visible part of the spectrum. It is not clear why the minimum value of ϵ_2 is not as low for In_2O_3 as for In_2O_3:Sn. Conceivably, the

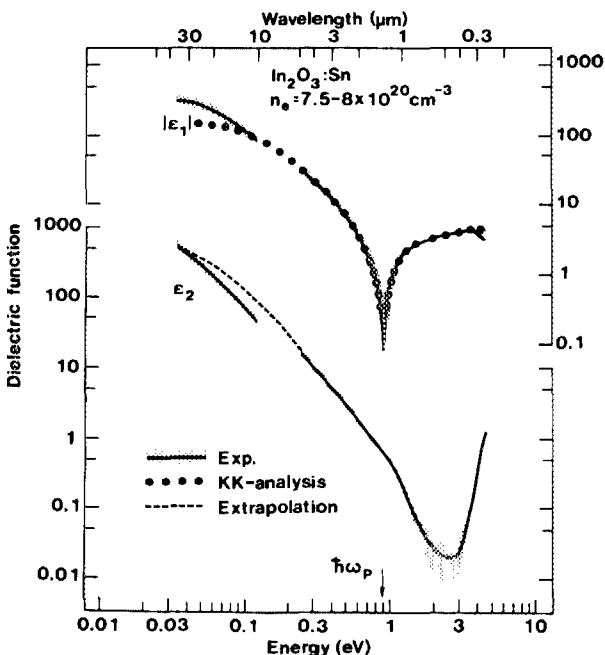FIG. 22. As in Fig. 19, but for In_2O_3:Sn films obtained by deposition of $In_2O_3 + 9$ mol % SnO_2 onto CaF_2 (sample D; cf. Fig. 14) and Si. The film used to obtain data at $\hbar\omega \gtrsim 0.2$ eV had $n_e \approx 8.0 \times 10^{20}$ cm^{-3}, while the film used at $\hbar\omega \lesssim 0.1$ eV had $n_e \approx 7.5 \times 10^{20}$ cm^{-3}.

investigated films have different degrees of crystallinity, and hence their intrinsic properties may not be different. In the infrared ($\hbar\omega \lesssim 1.5$ eV) ϵ_2 rises monotonically, whereas ϵ_1 goes down and crosses zero at an energy $\hbar\omega_p$. At $\hbar\omega \ll \hbar\omega_p$, ϵ_1 becomes strongly negative and the films enter a *reflecting regime* with metalliclike properties. A change in the slope of the ϵ_2 curves takes place at $\hbar\omega \approx \hbar\omega_p$, which is apparent particularly in Figs. 21 and 22. This is a feature which gives important clues to the basic electron scattering processes in In_2O_3:Sn, as we return to in Sec. VIII. Far out in the infrared, the In_2O_3 data display structure caused by phonon absorption.

The accuracy in the evaluated dielectric functions is an important issue since we wish to make valid comparisons with theoretical models in subsequent sections. The errors $\Delta\epsilon_1$ and $\Delta\epsilon_2$ are related to errors in the spectrophotometric input data $\Delta X^{(1)}$ and $\Delta X^{(2)}$ through the matrix equation[160]

$$\begin{pmatrix} \Delta X^{(1)} \\ \Delta X^{(2)} \end{pmatrix} = M \begin{pmatrix} \Delta\epsilon_1 \\ \Delta\epsilon_2 \end{pmatrix}, \tag{12}$$

where M contains the partial derivatives of $X^{(1)}$ and $X^{(2)}$ with respect to ϵ_1 and ϵ_2. These derivatives were computed numerically, and M was then inverted to yield $\Delta\epsilon_1$ and $\Delta\epsilon_2$. Using $|\Delta X| = 0.01$ as a general criterion for the uncertainty in the optical measurements, we obtain the magnitudes of $\Delta\epsilon_1$ and $\Delta\epsilon_2$ indicated by the shaded regions in Figs. 19–22. Presumably, $|\Delta X|$ is usually less than the above value, but, on the other hand, our procedure does not involve uncertainties in the film thickness determination, and on balance we should obtain a good feeling for the potential errors in ϵ. It is seen that the relative uncertainty is reassuringly small except around the minima in the ϵ_2 curves. In this region it is difficult to rely on thin-film data to determine the pertinent weak absorption.

The internal consistency of the dielectric functions can be tested by Kramers–Kronig (KK) analysis. To this end we used ϵ_2 to compute ϵ_1 according to[164]

$$\epsilon_1(\omega) = 1 + \frac{2}{\pi} P \int_0^\infty \frac{\omega' \epsilon_2(\omega')}{\omega'^2 - \omega^2} d\omega', \tag{13}$$

where P denotes the principal value of the integral. We fixed the ϵ_1 value at one wavelength in the visible or near infrared. For low frequencies we extrapolated ϵ_2 according to the Drude theory (indicated by dotted curves in Figs. 19–22). The solid dots in the upper parts of the figures show results of the KK analyses. The agreement with the curves obtained directly from the spectrophotometric measurements is seen to be good, and hence the shown complex dielectric functions are internally consistent.

C. Preliminary analysis using Drude theory

The classical Drude theory[164] can be used for a preliminary analysis of the data on ϵ. This will make it apparent that free electrons play a decisive role for the optical performance of the films. The Drude approach is also useful for computing the dielectric function of In_2O_3 in the absence of free electrons[22]—which is needed in a quantitative theory of the optical properties—and for deriving the electron density from the optical data.
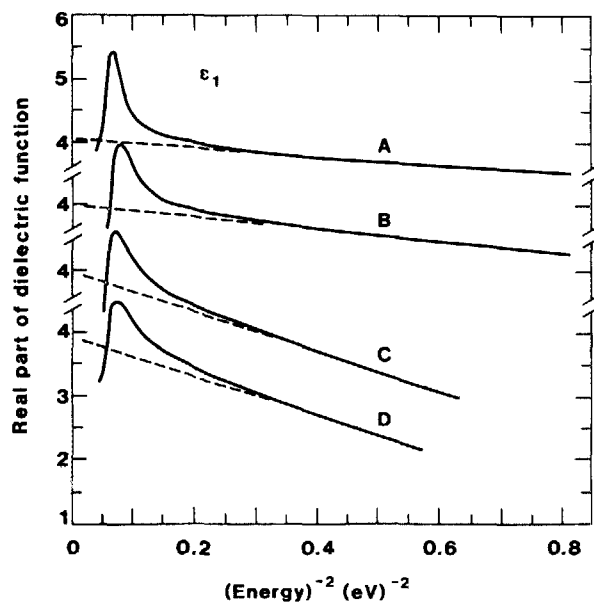
FIG. 23. Real part of the dielectric function for In_2O_3 and In_2O_3:Sn films vs $(\hbar\omega)^{-2}$. Solid curves represent empirical data for the samples A–D. The curves are vertically displaced. Dashed lines show linear extrapolations; their intercepts with $(\hbar\omega)^{-2} = 0$ yield ϵ_∞. The peaks in the left-hand part are due to the approach of the band gap and cannot be accounted for by the Drude analysis.

FIG. 24. Theoretical and empirical results for the real and imaginary parts of the dielectric function of an In_2O_3:Sn film. Solid curves were computed from the Drude theory using the shown values of $\hbar\omega_p$, $\hbar\gamma$, and ϵ_∞. Dashed curves show part of the data reported for sample C in Fig. 21.

The Drude theory describes the free electron contribution to the dielectric function by

$$\epsilon_1^{Drude}(\omega) = \epsilon_\infty - [\omega_N^2/(\omega^2 + \gamma^2)], \qquad (14)$$

$$\epsilon_2^{Drude}(\omega) = (\gamma/\omega)[\omega_N^2/(\omega^2 + \gamma^2)], \qquad (15)$$

where ϵ_∞ is the dielectric constant extrapolated towards high energy, and $\hbar\gamma$ is a relaxation energy which may be taken as energy-independent for qualitative analyses. The electron density and the effective conduction-band mass of the electrons m_c^* determine ω_N through

$$\omega_N^2 = n_e e^2/\epsilon_0 m_c^*, \qquad (16)$$

where $\epsilon_0 = 8.854 \times 10^{-12}$ A s/V m is the permittivity of free space. The energy at which $\epsilon = 0$—i.e., the longitudinal plasma energy $\hbar\omega_p$—is approximately related to $\hbar\omega_N$ by

$$\omega_p^2 = (\omega_N^2/\epsilon_\infty) - \gamma^2. \qquad (17)$$

The value of ϵ_∞ can be determined by plotting ϵ_1 vs $(\hbar\omega)^{-2}$, provided that the Drude formalism applies. Figure 23 shows results for the samples A–D. The extrapolated value is

$$\epsilon_\infty = 3.95 \pm 0.1, \qquad (18)$$

where it seems that the upper limit pertains to low doping and the lower limit to high doping. For the following analysis it is accurate enough to put $\epsilon_\infty = 4$ irrespective of doping. This is the value found in most earlier investigations,[8] although Ohhata et al.[46] has stated that ϵ_∞ goes from 4.0 down to ~3 when the doping is increased.

If we except the interband absorption in the ultraviolet and the phonon absorption in the far infrared, the main features of the dielectric functions in Figs. 19–22 are consistent with the Drude theory, and hence it is evident that free elec-
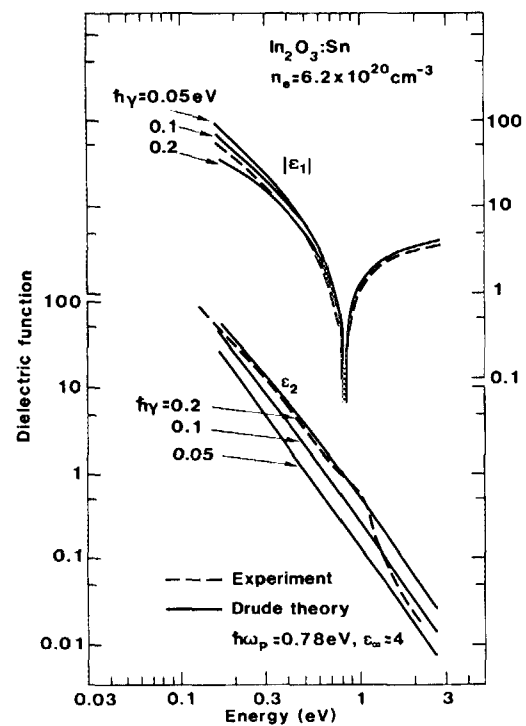
trons play a crucial role for the optical properties. Figure 24 shows an example of the overall applicability of the Drude theory. The solid curves were drawn with $\hbar\omega_p = 0.78$, $\epsilon_\infty = 4$, and three different values of $\hbar\gamma$. The agreement with the empirical data (dashed curves) is good, particularly for $\hbar\omega < \hbar\omega_p$, if we set $\hbar\gamma \lesssim 0.2$ eV. These values were used to extrapolate ϵ_2 towards low energy in Fig. 21, and analogous extrapolations—with other magnitudes of $\hbar\omega_p$ and $\hbar\gamma$—were given in Figs. 19, 20, and 22. The above results can be compared with earlier data. For example, the sputtered In_2O_3:Sn films studied by Fan and Bachner[70] and by Yoshida[42,43] were represented by $\hbar\omega_p = 0.77$ eV, $\hbar\gamma = 0.075$ eV, $\epsilon_\infty = 4.45$ and $\hbar\omega_p = 0.71$ eV, $\hbar\gamma = 0.12$ eV, $\epsilon_\infty = 4.0$, respectively. A most important result from Fig. 24 is that there is a change in the slope of the ϵ_2 curve around $\hbar\omega_p$, and above this energy we have to invoke a relaxation energy which decreases with increasing photon energy. Clearly, the simple Drude theory provides no explanation for this effect.

In the later analysis we will investigate the effect of Sn atoms added to an In_2O_3 host lattice. The dielectric function of "undoped" In_2O_3, denoted $\epsilon^{In_2O_3}$, is therefore of importance. As elaborated in Ref. 22, this quantity can be obtained by subtracting ϵ^{Drude} from the empirical ϵ, i.e., by

$$\epsilon^{In_2O_3} = \epsilon - \epsilon^{Drude}. \qquad (19)$$

At energies far below the semiconductor band gap we expect $\epsilon_2^{In_2O_3}$ to be zero except in the wavelength range where phonon absorption is important, i.e., at $0.035 \lesssim \hbar\omega \lesssim 0.055$ eV. Within the phonon range one may take ϵ^{Drude} to be a smoothly varying background, as shown in Fig. 25. The remaining part of the evaluated dielectric function is hence
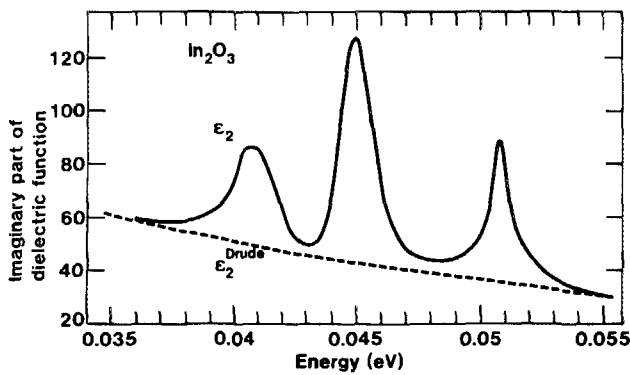
FIG. 25. Theoretical and empirical results for the imaginary part of the dielectric function of an In_2O_3 film. Solid curve is an enlargement of the empirical data given in Fig. 19. Dashed curve shows a Drude plot, which has been fitted to the empirical results outside the range of phonon absorption.

$\epsilon_2^{In_2O_3}$. The corresponding real part, $\epsilon_1^{In_2O_3}$, can be determined by Kramers–Kronig analysis according to Eq. (13). Using $\epsilon_\infty^{In_2O_3} = 4$ we found[22] $\epsilon_1^{In_2O_3}(0) = 8.9$. The latter value corresponds to the static dielectric constant. It is interesting to note that the values 9 and 9.5 have been used for this quantity in recent work by Frank et al.[98,99] and by Szczyrbowski et al.[61]; the reasons behind these choices were not given, though. The ensuing dielectric function of "undoped" In_2O_3 is shown in Fig. 26. The two most salient features are the semiconductor band gap and the phonon structure comprising three peaks. In the intervening range we have $\epsilon^{In_2O_3} \approx 4 + i0$. The band gap at 3.75 eV is consistent with literature results[165] for single-crystalline In_2O_3.

We now turn to the evaluation of electron density. As seen from Eqs. (16) and (17), this quantity is found once $\hbar\omega_p$ and the product $\epsilon_\infty m_c^*$ have been determined (provided that $\hbar\omega_p \gg \hbar\gamma$, which is usually the case). The plasma energy can be obtained with high precision—typically better than 2%—but $\epsilon_\infty m_c^*$ is less easy to get. Using Hall-effect data one can plot $(\hbar\omega_p)^2$ versus n_{eH} and extract information[156] on $\epsilon_\infty m_c^*$, but this procedure is connected with some uncertainty, as mentioned in Sec. IV B. Probably the best data were
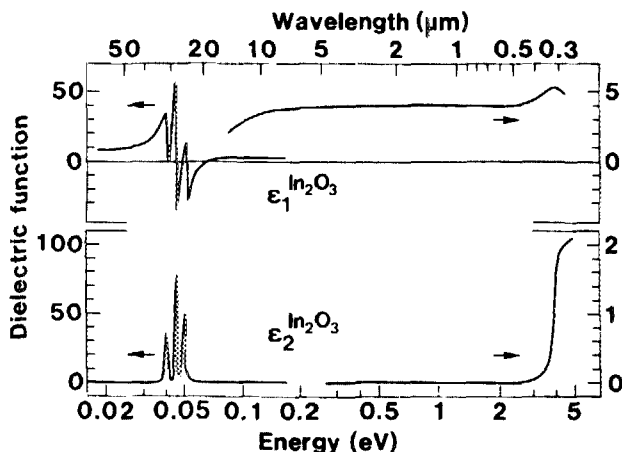

FIG. 26. Real and imaginary parts of the dielectric function for "undoped" In_2O_3. Different vertical scales are used, as indicated by the arrows.

given by Köstlin et al.,[83] who investigated a large number of In_2O_3:Sn samples with different dopings and concluded that

$$\epsilon_\infty m_c^* = 1.4m, \qquad (20)$$

where m is the free-electron mass. Thus with $\epsilon_\infty = 4$ we have $m_c^* = 0.35m$. Equation (20) was used to obtain the n_e values given in Table I and in several figures in this review. A somewhat different magnitude of the $\epsilon_\infty m_c^*$ ratio was reported by Ohhata et al.[46]

VI. INTERLUDE: ELEMENTS OF A THEORY FOR THE OPTICAL PROPERTIES

We wish to analyze the optical properties of In_2O_3:Sn by regarding In_2O_3 as a host lattice to which the effect of the Sn dopant is added. The bandstructure of In_2O_3 forms the basis of such a theory. Unfortunately, the complicated crystal structure of In_2O_3 (the C-type rare-earth oxides have 80 atoms per unit cell) has precluded bandstructure calculations, and to our knowledge the only attempt for a similar material is in recent work[166] on Eu_2O_3. We note in passing that bandstructures have been worked out for several other oxide semiconductors which may be useful as window coatings, such as ZnO (Ref. 167), CdO (Ref. 168), SnO_2 (Ref. 169), and WO_3 (Refs. 170 and 171).

Figure 27(a) shows the assumed bandstructure of undoped In_2O_3. It has parabolic bands characterized by m_c^* for the conduction band and m_v^* for the valence band. Both bands are taken to be isotropic. The direct semiconductor band gap, denoted E_{g0}, is[165] 3.75 eV. Furthermore, we know that $m_c^* \approx 0.35m$, whereas the magnitude of m_v^* is unknown. It has been proposed[172] that the conduction band is mainly from indium 5s electrons and the valence band is from oxygen 2p electrons. For the undoped material, the Fermi energy E_F is located halfway between the energy bands. With the introduction of a low density of donor atoms, donor states are formed just below the conduction band. Now E_F lies between the donor level and the conduction-band minimum. For increased donor density, the donor states merge with the conduction band at a certain critical density n_c, whose magnitude can be estimated using Mott's criterion[173,174]

$$n_c^{1/3} a_0^* \approx 0.25. \qquad (21)$$

The effective Bohr radius a_0^* is given by

$$a_0^* = h^2 \epsilon_0 \epsilon^M / \pi e^2 m_c^*, \qquad (22)$$

where ϵ^M is the static dielectric constant of the host lattice. Using data for In_2O_3 [i.e., $\epsilon^M = \epsilon_1^{In_2O_3}(0) = 8.9$] we find $a_0^* \approx 1.3$ nm, and hence—since each donor provides one electron—we expect free-electron properties when $n_e > n_c \approx 6 \times 10^{18}$ cm^{-3}. Above the Mott critical density, E_F is determined by the highest occupied states in the conduction band, and we can write

$$E_F = (\hbar^2/2m_c^*)k_F^2, \qquad (23)$$

where the magnitude of the wave vector at the Fermi energy is

$$k_F = (3\pi^2 n_e)^{1/3}. \qquad (24)$$

The bandstructure of heavily doped In_2O_3:Sn is sketched in Fig. 27(b). A partial filling of the conduction band as well as
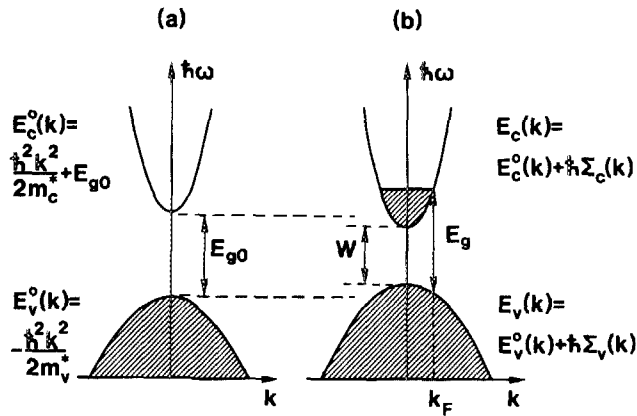
FIG. 27. (a) shows the assumed bandstructure of undoped In_2O_3 in the vicinity of the top of the valence band and the bottom of the conduction band. (b) describes the effects of Sn doping. A shift of the bands is apparent. Shaded areas denote occupied states. Band gaps, Fermi wave number, and dispersion relations are indicated.

shifts in energy of the bands—relative to their location in In_2O_3—are indicated.

It is apparent from Fig. 27, as well as from the foregoing sections, that there are several physical mechanisms which influence the optical properties of In_2O_3:Sn. In many cases it is possible to split up the dielectric function of a heavily doped semiconductor into parts corresponding to separate

FIG. 28. Schematic representation of the complex susceptibilities $\chi \equiv \chi_1 + i\chi_2$ (due to valence electrons, polar optical phonons, and free carriers) which contribute to the complex dielectric function of a heavily doped semiconductor. They are shown with a common horizontal energy scale. A single peak in χ_2 is taken to signify each of the absorption mechanisms, and the corresponding χ_1's are drawn to be consistent with the Kramers–Kronig relation.

elementary excitations.[175,176] We may write

$$\epsilon = 1 + \chi^{VE} + \chi^{FC} + \chi^{PH} \qquad (25)$$

for the interesting photon energies, where χ is a complex susceptibility, and the superscripts denote valence electrons (VE), polar optical phonons (PH), and free carriers (FC). The separation is useful particularly if the χ's correspond to resonances lying in different energy ranges. Far from the resonance, χ is real and constant. For undoped In_2O_3, only χ^{VE} and χ^{PH} are relevant, while doping makes it possible to vary the magnitude of χ^{FC} within wide limits.

χ^{VE} is due to interband transitions of valence electrons. The resonances lie at high energies in the ultraviolet. Well below the band gap, the electrons respond quickly to an applied electromagnetic field, and the material can be characterized by the real high-energy dielectric constant ϵ_∞. χ^{PH} is caused by polar optical phonons which couple to the applied transverse field. The photon energies lie in the far infrared. χ^{FC} originates from free electrons; the associated resonance is at zero energy. Figure 28 gives a schematic representation of the electron susceptibilities and the ensuing dielectric function. There is a convincing qualitative agreement with the dielectric function evaluated from optical measurements on In_2O_3:Sn films (shown on a logarithmic ordinate in Figs. 19–22). The following three sections will be devoted to detailed quantitative analyses of χ^{VE}, χ^{FC}, and χ^{PH}.

VII. ANALYSIS OF OPTICAL PROPERTIES AROUND THE BAND GAP

The optical data presented in Sec. IV A indicated that the band gap became wider as the electron density went up. The physics behind this effect is an interesting subject in itself. The phenomenon is also important in connection with window coatings, since a narrowing of the band gap—or an unchanged band gap in conjunction with a smearing of the onset of absorption—would tend to produce an unwanted absorption in the solar and luminous spectral ranges. Section VII A reviews results on the optical band gap E_g for In_2O_3 and In_2O_3:Sn films. We find consistently that

$$E_{g0} < E_g \equiv E_{g0} + \Delta E_g, \qquad (26)$$

where ΔE_g is a positive quantity whose magnitude is increased for increasing electron density. In Sec. VII B we summarize theoretical models for ΔE_g. They encompass a Burstein–Moss shift[177,178] which is partially balanced by a narrowing of the intrinsic band due to manybody effects (treated in the random phase approximation[176,179]). Section VII C shows that theory and experiments can be reconciled provided that m_v^* is assigned an appropriate value. Sections VII A–C are based on Refs. 28 and 31. Section VII D is devoted to the tailing of the band gap towards low energy.[32] This tailing is associated with an Urbach behavior,[180,181] whose origin is discussed.

A. Data on band-gap widening

From the optical constants of In_2O_3 and In_2O_3:Sn (n and k inherent in Figs. 19–22) one can derive the absorption coefficient by

$$\alpha = 4\pi k/\lambda. \qquad (27)$$

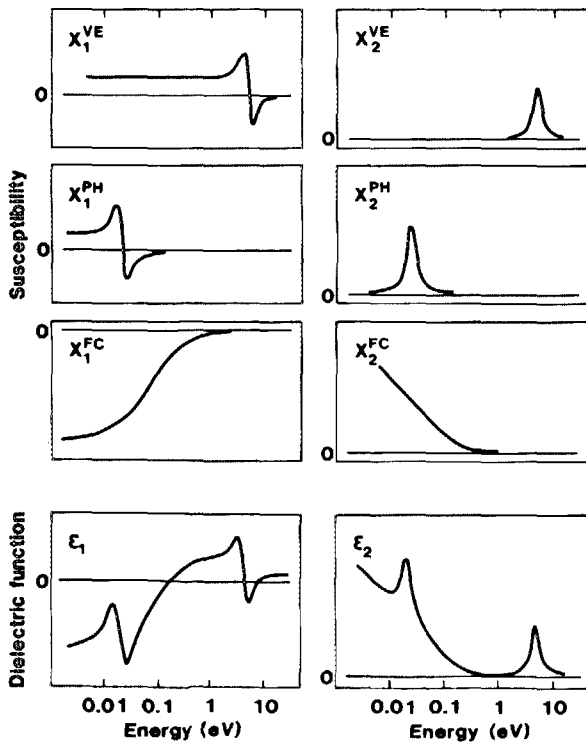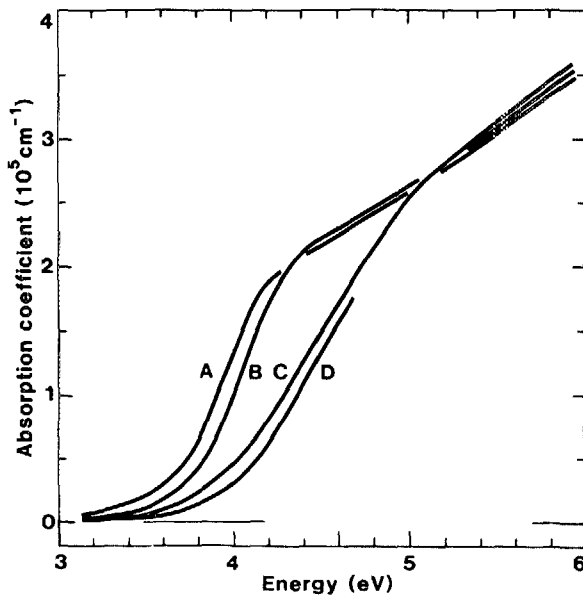FIG. 29. Spectral absorption coefficients for films of In_2O_3 (sample A) and In_2O_3:Sn (samples B–D). Corresponding electron densities were given in Table I.

FIG. 30. Energy gap vs electron density to the power 2/3 for films of In_2O_3 and In_2O_3:Sn (samples A–D). Approximate energy gaps were obtained by plotting α^2 vs $\hbar\omega$. Different symbols indicate results for our own work on films made by reactive e-beam evaporation (Refs. 28, 31; data denoted "this work"), as well as for sputtered films studied by Vainshtein and Fistul' (Ref. 121), Ohhata et al. (Ref. 46), and Smith and Lyu (Ref. 51), and for films made by chemical vapor deposition by Kulaszewicz et al. (Ref. 104). Possible errors in the determination of n_e are indicated by bars. Arrow points at the energy gap for undoped In_2O_3, as given by Weiher and Ley (Ref. 165). Solid curve was computed from the theoretical model outlined in Sec. VII B with $E_{g0} = 3.75$ eV and $m_v^* = 1.0m$.

Figure 29 shows results for samples A–D in the $3 < \hbar\omega < 6$ eV range. We find a gradual shift of the band gap towards higher energy as the electron density is increased. This is actually a well-known effect, which has been reported many times for heavily doped oxide semiconductors based on In_2O_3 (Refs. 8, 11, 28, 31, 32, 34, 46, 48, 51, 61, 72, 75, 83, 88, 101, 104, 121, 122, 129, 135, 148, and 165), ZnO (Refs. 182–184), CdO (Ref. 185), SnO_2 (Refs. 88 and 186–191), and Cd_2SnO_4 (Refs. 192–194). The most detailed study is found in a rather old work on nonstoichiometric CdO by Finkenrath.[185] We note from Fig. 29 that the onset of absorption is rather gradual and that the curves intersect at high energies.

It is commonplace to use a relation

$$\alpha \propto (\hbar\omega - E_g')^{1/2} \quad \text{for } \hbar\omega > E_g' \qquad (28)$$

to derive band gaps for heavily doped oxide semiconductors. Somewhat different formulas (for example, with $\hbar\omega\alpha$ instead of α) are also frequently used.[164] This procedure is amenable to criticism and seems to be rooted in misconceptions. It should be observed that Eq. (28) is approximately correct for direct allowed transitions to an empty parabolic conduction band.[164] Thus one might determine E_{g0} by plotting α^2 vs $\hbar\omega$. However, this simple technique is *not* valid for the heavily doped semiconductor, since the lowest states in the conduction band are blocked, and transitions can take place only to energies above E_F. This situation is illustrated in Fig. 27(b). We return to a proper way of extracting band gaps in Sec. VII C. For the moment, however, we wish to compare different experimental results on band-gap widening—based on plots of α^2 vs $\hbar\omega$—and so we have to resort to the same procedure. The comparison is given in Fig. 30, where the band gaps are shown as a function of $n_e^{2/3}$. The data from our own work[28,31] (solid triangles) are in reasonable agreement with those of Ohhata et al.[46] (open circles), whereas the results of Vainshtein and Fistul'[121] (solid squares), Smith and Lyu[51] (solid circles), and Kulaszewicz
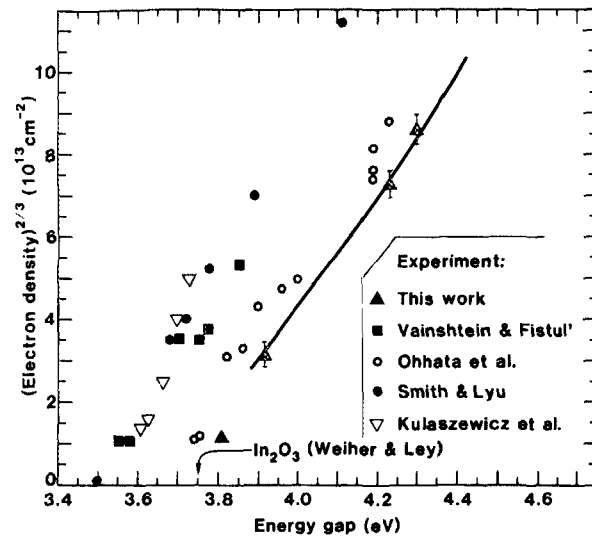
et al.[104] (open triangles) are displaced towards lower energy. Even larger displacements were reported by Ray et al.[75] Our results are consistent with the energy gap $E_{g0} = 3.75$ eV measured for undoped In_2O_3 by Weiher and Ley.[165] An important result from Fig. 30 is that the band gaps scale approximately with $n_e^{2/3}$.

B. Theoretical models for shifted band gaps

We start from the bandstructure shown in Fig. 27 and follow closely the analysis in Ref. 28. The dispersions for the valence and conduction bands in the undoped In_2O_3 lattice can then be written

$$E_v^0(k) = -\hbar^2 k^2/2m_v^*, \qquad (29a)$$

$$E_c^0(k) = E_{g0} + \hbar^2 k^2/2m_c^*, \qquad (29b)$$

where k is the wave vector and superscript 0 denotes unperturbed bands. The top of the valence band is taken as reference energy. When doping is introduced and $n_e > n_c$, there is a blocking of the lowest states in the conduction band and hence a widening of E_g. But at the same time electron-electron and electron-impurity scattering tend to decrease the gap.[195–198] This is illustrated by setting $E_{g0} > W$ in Fig. 27, where W is the energy difference between the top of the valence band and the bottom of the conduction band in the doped material. Finally, there may be a k dependence of m_c^* and m_v^*.

We first consider the blocking of the lowest states in the conduction band and neglect scattering effects. Then

$$E_g^0 = E_{g0} + \Delta E_g^{BM}, \qquad (30)$$

where ΔE_g^{BM} is the band-gap shift given by the Burstein–

Moss (BM) theory,[177,178] viz.,

$$\Delta E_g^{BM} = (\hbar^2/2m_{vc}^*)(3\pi^2 n_e)^{2/3}, \qquad (31)$$

with the reduced effective mass

$$(m_{vc}^*)^{-1} = (m_v^*)^{-1} + (m_c^*)^{-1}. \qquad (32)$$

Equation (31) yields a band-gap change proportional to $n_e^{2/3}$, which is in approximate agreement with experiments. This has led to the unjustified assumption[8,11,34,46,48,51,61,72,75,87,88,104,121] that the BM shift alone would determine the band-gap widening.

In a more complete theory one also has to include band-gap shifts due to electron interaction and impurity scattering. The ensuing effect can be described by replacing the dispersions of the unperturbed bands by the corresponding quasiparticle dispersions

$$E_v(k,\omega) = E_v^0(k) + \hbar\Sigma_v(k,\omega), \qquad (33a)$$

$$E_c(k,\omega) = E_c^0(k) + \hbar\Sigma_c(k,\omega), \qquad (33b)$$

where $\hbar\Sigma_v$ and $\hbar\Sigma_c$ are self-energies due to electron-electron (ee) and electron-impurity (ei) scattering. In a perturbation treatment we may take these processes to be additive, i.e.,

$$\Sigma_v = \Sigma_v^{ee} + \Sigma_v^{ei}, \qquad (34a)$$

$$\Sigma_c = \Sigma_c^{ee} + \Sigma_c^{ei}. \qquad (34b)$$

The band gap is now given by Eq. (26) with

$$\Delta E_g = \Delta E_g^{BM} + \hbar\Sigma_c(k_F,\omega) - \hbar\Sigma_v(k_F,\omega). \qquad (35)$$

The computation of the pertinent self-energies (Σ_v^{ei}, Σ_c^{ei}, Σ_v^{ee}, and Σ_c^{ee}) within the random phase approximation[176,179] is rather demanding and a full discussion is not possible in this review. We refer to Refs. 137, 156, 198, and 199 for details and contend ourselves with some comments here. The computation of Σ_v^{ei} and Σ_c^{ei} is simplified by the fact that the Sn^{4+} ions—which enter substitutionally on In^{3+} sites in the In_2O_3 lattice—behave effectively as singly charged point scatterers, as can be shown by representing the
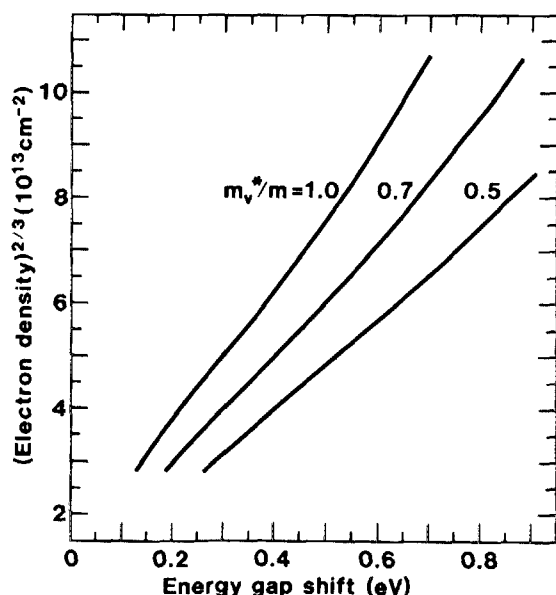

FIG. 31. Band-gap shift as a function of electron density to the power 2/3 computed for three magnitudes of the effective valence-band mass.
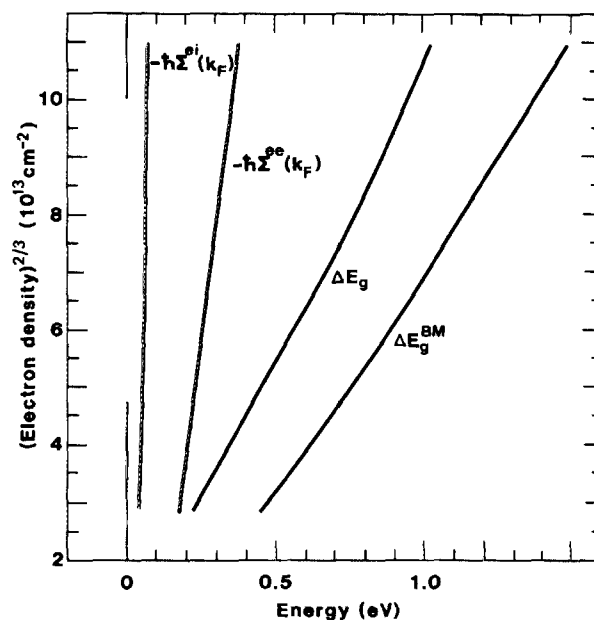

FIG. 32. Energy as a function of electron density to the power 2/3 computed for $m_v^* = 0.6m$. The band-gap shift (ΔE_g) is decomposed into contributions due to the Burstein–Moss effect (ΔE_g^{BM}), electron-impurity scattering [$\hbar\Sigma^{ei}(k_F)$], and electron-electron scattering [$\hbar\Sigma^{ee}(k_F)$].

ionic species by their Heine–Abarenkov pseudopotentials.[200,201] We return to this point in Sec. VIII D. The simplification may well be invalid if the substituting ion has a pseudopotential widely different from that of the substituted ion. The computation of Σ_v^{ee} and Σ_c^{ee} is facilitated by suppressing the energy dependence of the background. Explicit results were obtained by setting $\hbar\omega$ equal to $\hbar k_F^2/2 m_{v(c)}^*$, and using m_c^* as given in Ref. 46.

Figures 31 and 32 show results obtained from the detailed theory of band-gap shifts outlined above. Figure 31 gives ΔE_g as a function of $n_e^{2/3}$ with m_v^*, the only free parameter, having values between 0.5 and 1.0m. It is found that an increasing electron density yields an enhanced gap shift, and that at constant electron density one obtains the largest shift for the smallest valence-band mass. A decomposition of ΔE_g into its various contributions is presented (with $m_v^* = 0.6m$) in Fig. 32. It reports ΔE_g^{BM} as well as

$$\hbar\Sigma^{ei}(k_F) \equiv \hbar\Sigma_c^{ei}(k_F) - \hbar\Sigma_v^{ei}(k_F) \qquad (36a)$$

and

$$\hbar\Sigma^{ee}(k_F) \equiv \hbar\Sigma_c^{ee}(k_F) - \hbar\Sigma_v^{ee}(k_F). \qquad (36b)$$

The BM shift is largest, but the effects of electron-impurity and electron-electron scattering are by no means negligible—being one half to one third in magnitude compared with ΔE_g. An earlier discussion of scattering-induced band-gap shrinkage in ZnO was given by Roth et al.[182]

C. Comparison of theory and experiments for band-gap widening

The measured spectral absorption coefficients show a considerable broadening (cf. Fig. 29), which must be included in the analysis before a detailed comparison with the computed E_g can be made, as discussed in Refs. 28 and 31. Using

a time-dependent perturbation theory[202] one can show that the rate for quantum-mechanical transitions between states in a filled parabolic valence band and a partially filled parabolic conduction band is given by

$$\mathscr{R} \propto \int_{\kappa_0}^{\infty} d\kappa (\kappa + \hbar\omega - W)^{1/2} \frac{\Gamma}{\kappa^2 + \Gamma^2} (1 - P_F), \quad (37)$$

with the notation

$$\kappa \equiv (\hbar^2 k^2/2m_{vc}^*) + W - \hbar\omega, \quad (38)$$

$$\kappa_0 \equiv \Delta E_g^{BM} + W - \hbar\omega. \quad (39)$$

Γ accounts for the broadening of the states and is assumed to be k independent. W is given, approximately, by

$$W \approx E_{g0} + \hbar\Sigma_c(k_F) - \hbar\Sigma_v(k_F), \quad (40)$$

and it is apparent that $W + \Delta E_g^{BM}$ is the experimental quantity to be compared with computed E_g. Blocking of states in the valence band due to thermal excitations is represented by a Fermi function

$$P_F = \left\{ \exp\left[\left(\frac{\hbar^2 k^2}{2m_c^*} - \mu_0 \right) \frac{1}{k_B T_0} \right] + 1 \right\}^{-1}, \quad (41)$$

where $k_B T_0$ is Boltzmann's constant times the temperature, and μ_0 is the chemical potential. At $k_B T_0 \ll E_F$, which is true for the present films, we have

$$\mu_0 \approx E_F \left[1 - \frac{\pi^2}{3} \left(\frac{k_B T_0}{2E_F} \right)^2 \right]. \quad (42)$$

Putting $\alpha \propto \mathscr{R}$, which is valid not too far from the energy gap, one has a model[28,31] for the spectral absorption coefficient in terms of the two parameters $W + \Delta E_g^{BM}$ and Γ.

Figure 33 shows a comparison between theory and experiment for two In$_2$O$_3$:Sn films. The circles represent experimental absorption coefficients. They are compared with computed data (curves) with $W + \Delta E_g^{BM}$ chosen to obtain
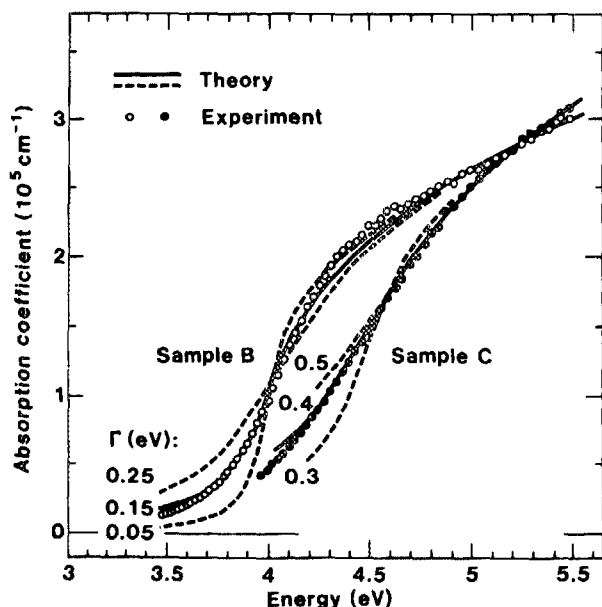
TABLE II. Data for films of In$_2$O$_3$ (sample A) and In$_2$O$_3$:Sn (samples B–D). Results are given for electron density (n_e), band-gap energy ($W + \Delta E_g^{BM}$), and band-gap width (Γ).

Sample	n_e (10^{20} cm^{-3})	$W + \Delta E_g^{BM}$ (eV)	Γ (eV)
A	0.4	3.88	0.07
B	1.7	4.04	0.13
C	6.2	4.46	0.37
D	8.0	4.55[a]	0.35[a]

[a] This value is based on an evaluation of α vs $\hbar\omega$ for $\hbar\omega < 4.7$ eV only, and is somewhat uncertain.

best agreement around the steepest parts of the curves, and Γ as given in the figure. The parameter values extracted from the fits in Fig. 33—and analogous comparisons for other samples—are listed in Table II. We find that both $W + \Delta E_g^{BM}$ and Γ increase with increasing electron density. The band gaps obtained by plotting α^2 vs $\hbar\omega$ are smaller than those given in Table II by an amount $\sim \Gamma$, which is in fact to be expected.[28]

We are now ready to compare $W + \Delta E_g^{BM}$ with E_g. Figure 34 shows that good agreement can be reached, provided that E_{g0} and m_v^* are chosen appropriately. For $m_v^* = 0.7m$ we obtain best agreement by setting $E_{g0} = 3.82$ eV, whereas for $m_v^* = 0.6m$ the corresponding energy is 3.75 eV. Thus it appears that one has to assume a band gap for the undoped crystal which is either the same as for single-crystalline In$_2$O$_3$, or somewhat larger than this value. A more detailed calculation,[199] retaining the k dependence of the self-ener-

FIG. 33. Spectral absorption coefficients for films of In$_2$O$_3$:Sn. Filled and open circles refer to measured data, and solid and dashed curves to computations (with $T_0 = 300$ K). We used $W + \Delta E_g^{BM}$ as shown in Table II and Γ as given in the figure.
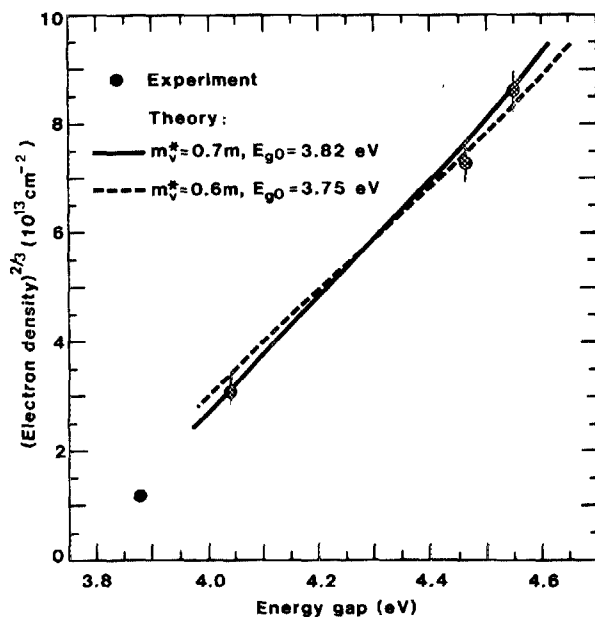
FIG. 34. Energy gap vs electron density to the power 2/3 for films of In$_2$O$_3$ and In$_2$O$_3$:Sn (samples A–D). Solid dots refer to the band gaps listed in Table II. Possible errors in the determination of n_e are indicated by bars. Solid and dashed curves were computed with the shown values of effective valence-band mass and host crystal band gap. The curves are confined to $n_e^{2/3} \gtrsim 3 \times 10^{13}$ cm^{-2} since the theory only applies to electron densities well above the Mott critical density [cf. Eqs. (21) and (22)].

gies, corroborates the present magnitudes of m_v^* and E_{g0}. It is also possible to compare the theory with the approximate band gaps in Fig. 30; the solid curve in this figure pertains to $m_v^* = 1.0m$ and $E_{g0} = 3.75$ eV. Unfortunately, it is not possible to confirm the present results on m_v^* with detailed band-structure data.

The parameter Γ can also be interpreted by theoretical arguments. The initial and final states of the quantum-mechanical transitions are broadened as a result of scattering. Electron-impurity scattering can be estimated[28] for electrons in the conduction and valence bands, and the ensuing magnitude of Γ is similar to the one found in the experiment. Electron-electron scattering gives no broadening at the Fermi level for $T_0 = 0$ K, but since the folding in Eq. (37) also involves states away from the Fermi energy, Γ may be affected. Effects of electron-phonon interaction are similar. There may also be smearing effects due to local deformations of the lattice resulting from the randomly introduced Sn atoms. The latter mechanism may also be responsible for the Urbach tails, which we return to in Sec. VII D. Clearly, it is difficult to formulate a complete theory of Γ as a function of n_e, but there can be little doubt that the major contribution stems from the scattering of electrons against ionized impurities.

We close this section with some comments on the effect of neglecting the self-energy contributions to E_g, as has been done in previous analyses. Now it is possible to reconcile theory and experiments only by assuming a *negative* m_v^* somewhere between ~ -0.6 and $\sim -1.0m$. This would imply that the valence band were curved in the same direction as the conduction band. Inclusion of the self-energies leads to a *positive* m_v^*, as we have just shown. This proves the importance of electron-impurity and electron-electron scattering, and that qualitative differences can occur if they are neglected. It is interesting also to consider doped CdO (Ref. 185) and SnO$_2$ (Ref. 189). Analyzing the band gaps in terms of a BM shift, one obtains a negative m_v^*, which is demonstrably[168,169] in opposition with bandstructure calculations. Inclusion of self-energy effects would tend to improve the correspondence between theory and experiments, but no detailed results are currently available.

D. Logarithmic band edges (Urbach tails)

A common way of presenting band gaps is by plotting the logarithm of the absorption coefficient versus photon energy. Figure 35, taken from Ref. 203, shows such data for films of In$_2$O$_3$ and In$_2$O$_3$:Sn. The low-energy parts of the band gaps look almost linear, obeying the relation

$$\alpha = \alpha'' \exp[a(\hbar\omega - b)], \tag{43}$$

where α'', a, and b are parameters. This behavior is often referred to as Urbach tails.[180] For later reference we rewrite Eq. (43) in terms of a valence electron susceptibility, applicable in the band-edge range, as

$$\chi_{bc}^{VE} = \epsilon_\infty - 1 + i(\epsilon_\infty^{1/2}/2\pi)\lambda\alpha'' \exp[a(\hbar\omega - b)], \tag{44}$$

where the band-gap shift is represented, approximately, by

$$b = cn_e^{2/3} + d, \tag{45}$$

with c and d being constants. The results in Fig. 35 can be
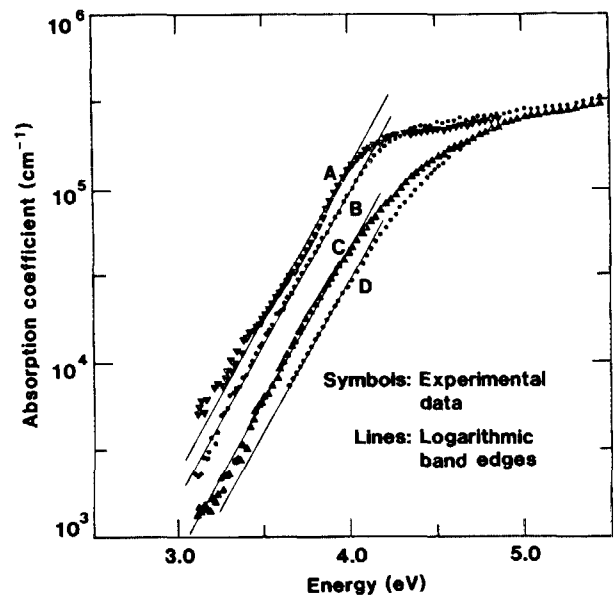

FIG. 35. Absorption coefficient vs photon energy for films of In$_2$O$_3$ (sample A) and In$_2$O$_3$:Sn (samples B–D). Symbols refer to experimental results taken at room temperature. A certain scatter in the data illustrates the difficulty of using thin films to measure small absorption coefficients. The parallel lines are indicative of logarithmic band edges.

reproduced by setting $\alpha'' = 1$ cm^{-1}, $a = 3.99$ (eV)$^{-1}$, $c = 0.376 \times 10^{-14}$ cm^2 eV, and $d = 0.979$ eV. This strictly empirical description holds for $\hbar\omega \lesssim 4$ eV.

Logarithmic band edges have been reported for many semiconductors,[181] and the phenomenon has been explained[204] from diverse models including electric microfields due to ionized defects,[205] thermal fluctuations of the band gap,[206] and excitonic effects.[207] Below we comment on the former two. In principle, the theory outlined earlier in this section could be extended to encompass also the band-edge range, but this has not yet been accomplished and so we are left here with more empirical and approximate models. We note that indirect forbidden transitions are known[165,208–210] to take place at 2.6 eV in In$_2$O$_3$, but the associated absorption is believed to be too weak to play any role in the present case.

Ionized defects, such as Sn^{4+} in In$_2$O$_3$, yield a broadening of the band gap which in principle could be treated with the theory outlined in Secs. VII B and VII C. However, we have chosen to follow here the approach of Redfield,[205] who described tailing through a Franz–Keldysh effect[211,212] of microfields caused by the defects. The absorption coefficient can be written

$$\alpha(\hbar\omega) = \int_0^\infty dq\, A(\hbar\omega, q) H(q), \tag{46}$$

where the electric field distribution $H(q)$ is given by the screened Holtzmark distribution, and the local absorption coefficient in the presence of a field q is

$$A(\hbar\omega) = \omega_q^{1/2} \int_{(E_g - \hbar\omega)/\hbar\omega_q}^\infty dy |\text{Ai}(y)|^2 \quad \text{for } \hbar\omega < E_g. \tag{47}$$

Here Ai(y) is the Airy function, and

$$\omega_q = (e^2 q^2 / 12\hbar m_{vc}^*)^{1/3}. \tag{48}$$

    I. Hamberg and C. G. Granqvist

Computations using Eqs. (46)–(48) showed that about half of the observed absorption could be explained through these formulas. However, the relation between $\log \alpha$ and $\hbar\omega$ was only approximately linear, and we do not believe that ionized impurities is the only reason for the band tails.

Another, more empirical, approach focuses on thermal fluctuations of the band gap.[204,206] A band gap is defined within a small cell whose size is about the phonon coherence length. The number of phonons within each cell is given by Bose–Einstein statistics and has an exponential distribution. The band gap within a cell is taken to be reduced in proportion to the number of phonons present. The band gaps can be written $E_g - \delta$, where the δ's are distributed according to

$$P(\delta) = \beta \exp(-\beta\delta) \quad \text{for } \delta \geqslant 0. \qquad (49)$$

The resulting band edge can then be represented by

$$\alpha(\hbar\omega) = \alpha_0 \int_{\delta_1}^{\infty} d\delta\, P(\delta)g[\hbar\omega - (E_g - \delta)], \qquad (50)$$

where $\delta_1 = 0$ for $\hbar\omega \geqslant E_g$ and $\delta_1 = E_g - \delta$ for $\hbar\omega < E_g$, and g is chosen so that it gives a good description of α for $\hbar\omega \geqslant E_g$. Equations (49) and (50) give a logarithmic band edge with slope β.

We do not wish to pursue the present analysis any further, but merely state that there are several mechanisms which can contribute to the logarithmic band edges, and that one of them is associated with the ionized impurities in In_2O_3.

VIII. ANALYSIS OF THE FREE-ELECTRON PROPERTIES

The spectral selectivity which is desired for a window coating rests to a large extent on its free-electron properties. A quantitative analysis of them will be given here. It is most conveniently performed in terms of a complex dynamic resistivity $\rho \equiv \rho_1 + i\rho_2$, which is connected with the susceptibility by the general relation

$$\chi = i/(\epsilon_0 \omega \rho) . \qquad (51)$$

This formalism is particularly useful since ρ_1 is directly related to the type of scattering which prevails among the free electrons. In Sec. VIII A we discuss scattering mechanisms in general terms and argue that studies of ρ_1 for energies between the plasma energy and the band gap can discriminate between different types of scattering. Section VIII B is devoted specifically to ionized-impurity scattering. Our treatment is based on work by Gerlach and Grosse.[213] Screening in the free-electron gas is included through the random phase approximation and other electron gas theories. Section VIII C presents a comparison of theory and experiments for ρ. It is found that good agreement can be achieved for high-quality In_2O_3:Sn films by considering ionized impurity scattering only. We conclude in Sec. VIII D by a discussion of the roles of pseudopotential scattering and of exchange and correlation in the electron gas.

A. Mechanisms for scattering of the free electrons

We start from the Drude theory, which can be expressed in terms of a dynamic resistivity as

$$\rho_1^{\text{Drude}} = \gamma/(\epsilon_0 \omega_N^2) , \qquad (52)$$

$$\rho_2^{\text{Drude}} = -\omega/(\epsilon_0 \omega_N^2) . \qquad (53)$$

It is seen that ρ_1^{Drude} includes the whole effect of scattering, whereas ρ_2^{Drude} is independent of scattering and can be understood as the result of the inertia of the free electrons. The Drude theory is not sufficient for a quantitative model of the free-electron properties. This is so because γ is introduced as a parameter whose magnitude can only be fixed by fitting to experimental data. Furthermore, we found evidence for an energy dependence of γ (cf. Fig. 24), which cannot be accounted for within the Drude model. In order to have a quantitative theory for In_2O_3:Sn, one must explicitly consider the scattering.

There are many sources of electron scattering which may influence the optical properties. One can separate between electron-defect scattering (against grain boundaries and external surfaces, neutral and ionized point defects, dislocations, precipitations, and clusters), electron-lattice scattering (against local deformation potentials, etc.), and electron-electron scattering. A general approach to electron scattering is founded on solutions of the Boltzmann transport equation. Thorough discussions have been given by Nag[214] and by Chattopadhyay and Queisser.[215] The expressions given for the frequency-dependent case are usually not accurate enough for quantitative analyses. We note, however, that approximate formulas for ϵ_2 have been derived[216] for ionized impurity scattering; they have been used[82,148] for interpreting some optical data in In_2O_3:Sn. A somewhat different approach to the scattering rests upon the equivalence of Joule heat and energy loss.[217] The formalism is outlined in a review by Gerlach and Grosse[213]; details are given in a series of short papers.[218–220] We will use this theory here since it provides detailed expressions for the dynamic resistivity.

Formally, we can go beyond the Drude theory by substituting

$$\gamma \rightarrow \gamma_1(\omega) + i\gamma_2(\omega) \qquad (54)$$

in Eq. (52). ρ_1 is still directly connected with the electron scattering, and a comparison of experimental and theoretical data for this quantity yields a crucial test of the validity of the models used. In the energy range

$$\hbar\omega_p < \hbar\omega < E_g , \qquad (55)$$

the comparison is straightforward, since ρ_1 obeys a power

TABLE III. Exponent s in the real part of the dynamic resistivity for different scattering mechanisms and scattering models.

Scattering mechanism	Scattering model	s
Ionized impurity	Coulomb potential	$-\frac{3}{2}$
Dislocation	Charged monopole line	-2
	Charged dipole line	-1
Neutral defect (short ranged)	δ potential	$\frac{1}{2}$
Acoustic phonons	Deformation potential coupling	$\frac{1}{2}$
	Piezoelectric coupling	$-\frac{1}{2}$
Optical phonons	Polar coupling	$-\frac{3}{2}$

law

$$\rho_1 \propto \omega^s , \qquad (56)$$

where s takes on different values depending on the scattering mechanism. Correspondingly, we have $\epsilon_2 \propto \omega^{s-3}$. Table III, based on Ref. 213, summarizes the exponents applicable to different scattering mechanisms, each represented by a certain scattering model. We find

$$s = -\tfrac{3}{2} \qquad (57)$$

for ionized impurity scattering, described by a Coulomb potential. Other exponents apply to neutral impurities, dislocations, and phonons.

B. Ionized impurity scattering

Several of the scattering mechanisms discussed above are expected to be of little importance in films with good crystallinity, such as for the best In_2O_3:Sn coatings. One important mechanism cannot be neglected, though, and it warrants a detailed treatment: the scattering against ionized impurities. These ions are necessary in order to have free electrons. We now follow Refs. 27 and 29 and note that if doping is entirely through the Sn atoms, the ion density N_i is

$$N_i = n_e . \qquad (58)$$

For doping by doubly charged oxygen vacancies, a corresponding relation would be $2N_i = n_e$.

The dynamic resistivity due to ionized impurity scattering can be written[213,218]

$$\rho(\omega) = i \frac{Z^2 N_i}{6\pi^2 \epsilon_0 n_e^2 \omega} \int_0^\infty k^2 \, dk \left(\frac{1}{\epsilon^{eg}(k,\omega)} - \frac{1}{\epsilon^{eg}(k,0)} \right)$$
$$- i \frac{\omega}{\epsilon_0 \omega_p^2} , \qquad (59)$$

where Z is the charge of the impurities (unity for Sn doping), and ϵ^{eg} is the dielectric function of the free-electron gas and accounts for the screening of the ions. Equation (59) assumes that the ions act as single scatterers. Some results are available also for pair scattering.[219] Alternative derivations of $\rho(\omega)$ are given in Refs. 221 and 222.
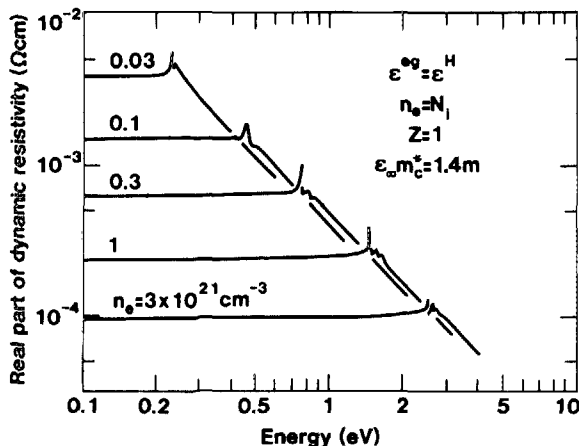

FIG. 36. Real part of the dynamic resistivity computed for ionized impurity scattering [Eq. (59)] with the shown parameters. The peak structure near the plasma energy is only partly resolved.

The remaining part of the theory regards ϵ^{eg}. We first use the random phase approximation[176,179] (RPA), which is in line with the treatment in Sec. VII. For electron collision processes it is the longitudinal part of the dielectric function that matters, and in the limit of small damping we have for the degenerate electron gas[179] (with $\epsilon^{eg} \equiv \epsilon^{RPA}$)

$$\epsilon^{RPA}(k,\omega) \equiv \epsilon_\infty + vP(k,\omega)$$
$$= \epsilon_\infty + (3\omega_N^2/k^2 v_F^2)(F_1 + iF_2) , \qquad (60)$$

$$F_1 = \frac{1}{2} + \frac{1}{8z} [1 - (z-u)^2] \ln \left| \frac{z - u + 1}{z - u - 1} \right|$$
$$+ \frac{1}{8z} [1 - (z+u)^2] \ln \left| \frac{z + u + 1}{z + u - 1} \right| , \qquad (61)$$

$$F_2 = \begin{cases} (\pi/2)u, & z + u < 1 , & (62) \\ (\pi/8z)[1 - (z-u)^2], & |z-u| < 1 < z+u , & (63) \\ 0, & |z-u| > 1 , & (64) \end{cases}$$

$$z = k/2k_F , \qquad (65)$$

$$u = |\omega|/kv_F , \qquad (66)$$

$$v_F = \hbar k_F/m_c^* . \qquad (67)$$

RPA is known[176] to yield a good description of the electron gas, particularly when the parameter

$$r_s^* = a_0^*(4\pi n_e/3)^{1/3} \qquad (68)$$

is small. In heavily doped oxide semiconductors one can have $r_s^* \sim 1$. This is, in fact, smaller than for metals, which attests to the applicability of the RPA. However, despite this fact, the RPA is not entirely satisfactory since it leaves out the effects of exchange and correlation, and it is of some interest to invoke more elaborate theories.

An extension of RPA which includes exchange but not correlation was introduced by Hubbard.[223] Now screening can be represented (with $\epsilon^{eg} \equiv \epsilon^H$) by

$$\epsilon^H(k,\omega) = \epsilon_\infty + [1 - G^H(k)]vP(k,\omega) , \qquad (69)$$

$$G^H(k) = k^2/2(k^2 + k_F^2) . \qquad (70)$$

The particular formulation in Eq. (69) pertains[224] to an electron-testcharge dielectric response, and a somewhat different expression would hold for a testcharge-testcharge response. The distinction between the two types of dielectric functions is discussed in Refs. 225–228. For the present case of electron-ion interaction it is believed[199] that Eq. (69) is adequate.

An improvement of the RPA is given by the Singwi–Sjölander theory,[229] which accounts for both exchange and correlation. As an approximation[230] one can still use Eq. (69), with G^H replaced by

$$G^{SS}(k) = A_1 \{1 - \exp[-A_2(k/k_F)^2]\} . \qquad (71)$$

A_1 and A_2 are weakly dependent on r_s^*. For $r_s^* = 1$, one can put[230] $A_1 = 0.71$ and $A_2 = 0.37$.

Figure 36 shows results of a model calculation of $\rho_1(\omega)$ by use of Eq. (59). Screening in the electron gas was introduced via the Hubbard dielectric function [Eqs. (69) and (70)]. Some small changes would occur if ϵ^{RPA} or ϵ^{SS} were employed instead, as we shall see. The parameters were chosen to make the data applicable to In_2O_3:Sn with $0.03 \leqslant n_e \leqslant 3 \times 10^{21}$ cm^{-3}. The curves show a consistent pat-

tern: At low energies there is a constant level, dependent on n_e, corresponding to the dc resistivity. Slightly above the plasma energy there is a rather abrupt "knee" and the curves fall off towards higher energy as $\sim \omega^{-3/2}$, which is the expected power dependence.

C. Comparison of theory and experiment

Experimental values on dynamic resistivity can be obtained from the dielectric functions by use of Eqs. (25) and (51). The dots and solid lines in Fig. 37, taken from Ref. 203, show results for three heavily doped In_2O_3:Sn films with somewhat different electron densities; the data are given point by point for $\hbar\omega > 0.5$ eV, since this range is of great importance for the theoretical analysis. We observe that the experimental results resemble the theoretically expected ones, given in Fig. 36. ρ_1 is rather constant below the plasma energy and joins smoothly with the measured dc resistivity. Above the plasma energy, ρ_1 falls off according to a power law. With due consideration of experimental uncertainties, we may state that s in Eq. (56) lies in the range

$$- 2 \lesssim s \lesssim - 1.3 . \tag{72}$$
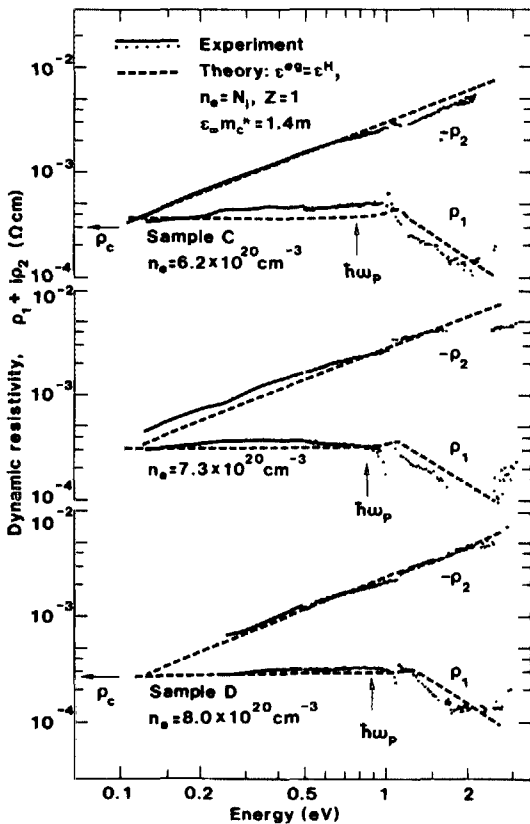
At the highest energies shown in Fig. 37, ρ_1 levels off and

FIG. 37. Real and imaginary parts of the dynamic resistivity for In_2O_3:Sn films. Dots and solid curves were evaluated for three films produced by evaporation of $In_2O_3 + 9$ mol % SnO_2. The actual spread in the data is apparent from the dots; the lines are shown for the energies where the spread is insignificant. The results at the top and bottom refer to samples C and D, respectively, whose dielectric functions were given in Figs. 21 and 22. Dashed curves were computed from the theory of ionized impurity scattering with the shown parameters. The detailed plasmon features around the "knee" in the ρ_1 data are not resolved. The pertinent values of plasma energy and dc resistivity are indicated by arrows.

starts to increase at the approach to the semiconductor band gap. $-\rho_2$ also follows a power law with an exponent between 0.85 and 1.0. Additional data, obtained for $\hbar\omega < 0.1$ eV, were consistent with the results in Fig. 37. Data for samples with $n_e = 0.4$ and 1.7×10^{20} cm^{-3} gave indications for a behavior similar to the one shown in Fig. 37, but the experimental uncertainties were too large to permit an entirely satisfactory analysis.

The experimental results can be compared with computations based on the theory outlined above. To this end we assume that only scattering against tin ions, each of which has donated one electron, is important. The Hubbard correction to the RPA is used, and the $\epsilon_\infty m_c^*$ ratio is as given by Eq. (20). The dashed curves in Fig. 37 were obtained with *no free parameter*. The correspondence between theory and experiment is striking; not only the slopes of the curves but also their magnitude in the whole spectral region—from the thermal infrared and well into the visible—are in agreement. The only significant discrepancy regards the "knee" in the ρ_1 data which seems to take place at a somewhat too high energy in the computations.

From the ρ_1 data in Fig. 37 one can conclude that the ionized impurities are dominating the scattering of the free electrons. Since these impurities are necessary as dopants, we may state that *the optical performance of the best In_2O_3:Sn films is approaching the theoretical limit*. The ρ_2 data are governed by the inertia of the free electrons, and the role of scattering is insignificant. Hence the agreement between theory and experiments for ρ_2 points at the internal consistency of our analysis but does not give information on the electron scattering. The importance of ionized impurity scattering has been asserted in some previous papers.[9,82,88,231] However, this earlier work was qualitative only and confined to rather narrow wavelength ranges. As far as we know, our work (originally reported in Refs. 27 and 29) gives the first *quantitative* analysis over a wide spectrum, encompassing the main part of the wavelength interval of interest for energy-efficient windows.

A constant mean free path l can be associated with the scattering at low energies by

$$l = v_F / \gamma , \tag{73}$$

where v_F is the velocity of the free electrons at the Fermi level. We find $l \sim 5$ nm for the samples of Fig. 37. Since the grain size is an order of magnitude larger (cf. Fig. 9), it is hardly surprising that grain-boundary scattering is not manifest. Above $\hbar\omega_p$ the ions become less efficient scatterers, and the associated mean free path goes up. At $\hbar\omega \sim 2$ eV it may well be that defect scattering is not negligible. In fact, it appears that the experimental ρ_1 data level off around this energy, which may speak in favor of a residual scattering mechanism apart from the ions. Phenomenologically, we may include the additional scattering by writing

$$\chi^{FC} = [i/\epsilon_0 \omega \rho(\omega)] + i\eta , \tag{74}$$

where $\rho(\omega)$ is due to ionized impurities and $\eta \approx 0.01$. The residual term η can be regarded as a quality measure for the films, and it is to be expected that its magnitude depends on the fabrication technique.
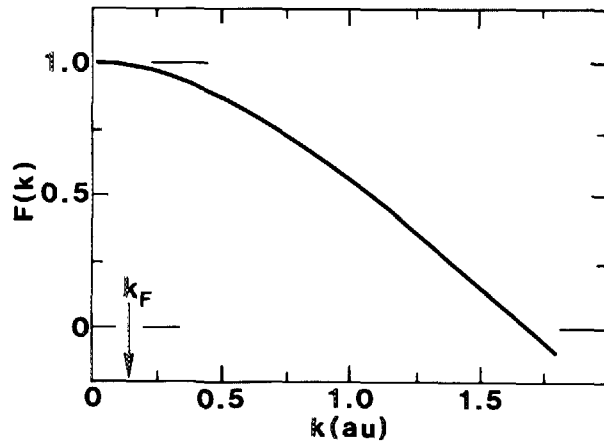
FIG. 38. $F(k)$ as a function of k in atomic units (au). $F(k)$ is the ratio between the Fourier transform of the bare scattering potential $V_{Sn}(r)$ $- V_{In}(r)$ and the Fourier transform of the Coulomb potential for a point charge. The evaluation was performed for $N_i = 10^{21}$ cm^{-3}, but is not sensitive to the detailed magnitude of the electron density. The arrow points at the Fermi wave number for $n_e = 7 \times 10^{20}$ cm^{-3}.
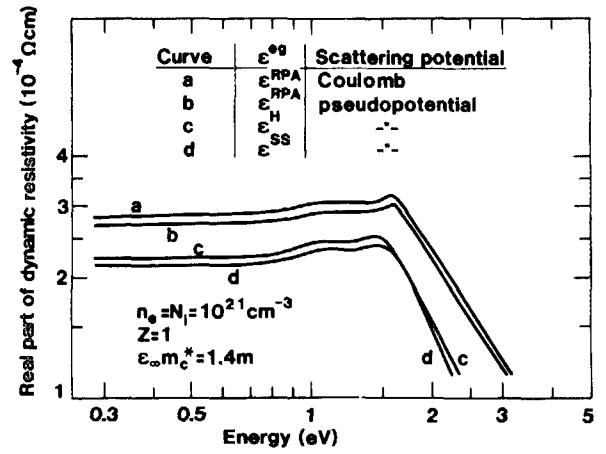

FIG. 39. Real part of the dynamic resistivity computed for ionized impurity scattering [Eqs. (59) and (79)] with the shown parameters. Different expressions for the screening in the electron gas and for the scattering potential were used to obtain the curves.

D. Comments on pseudopotential scattering, exchange, and correlation

The analysis given above used a Coulomb potential to represent electron-ion scattering and described screening in the electron gas by the Hubbard correction to the RPA. Here we consider these approximations in some detail. The discussion is based on Ref. 232.

A realistic representation of the scattering potential is given by

$$V_i(\mathbf{r}) = \sum_g [V_{Sn}(\mathbf{r} - \mathbf{R}_g) - V_{In}(\mathbf{r} - \mathbf{R}_g)], \qquad (75)$$

where $\mathbf{R}_g$ runs over a random distribution of Sn^{4+} on In^{3+} sites. V_i can be estimated by the Heine–Abarenkov pseudo-potentials[200,201] appropriate to the two ionic species, as discussed by Engström.[199] Figure 38 shows the function $F(k)$ defined by

$$F(k) \equiv V_i(k)/V_c(k), \qquad (76)$$

where $V_i(k)$ is the Fourier transform of the unscreened difference $V_{Sn}(r) - V_{In}(r)$ and $V_c(k)$ is the Fourier transform of the Coulomb potential for a point charge, viz.,

$$V_c(k) = Ze/\epsilon_0 k^2. \qquad (77)$$

It is seen that $F(k)$ is close to unity for $k \lesssim 2k_F$, which is the pertinent range for the computations. The explicit form of $V_i(k)$ may be parametrized as

$$V_i(k) = V_c(k) [1 + \zeta_1(k/k_F)^2 + \zeta_2(k/k_F)^3], (78)$$

where $\zeta_1 = -0.0154$ and $\zeta_2 = 0.000\,58$ apply for $N_i = 10^{21}$ cm^{-3}. The effect of pseudopotential scattering can now be studied explicitly, provided that we rewrite Eq. (59) as [199]

$$\rho(\omega) = i \frac{N_i \epsilon_0}{6\pi^2 n_e^2 e^2 \omega} \int_0^\infty k^6 \, dk \, |V_i(k)|^2$$

$$\times \left(\frac{1}{\epsilon^{eg}(\mathbf{k},\omega)} - \frac{1}{\epsilon^{eg}(\mathbf{k},0)} \right) - i \frac{\omega}{\epsilon_0 \omega_p^2}. \qquad (79)$$

Figure 39 reports on a set of calculations of ρ_1 for

$n_e = 10^{21}$ cm^{-3}. The influence of different scattering potentials and dielectric functions for the free-electron gas is investigated. Curve (a) was computed with a Coulomb potential and the RPA was used to describe the screening. We can compare curve (a) with curve (b), obtained by replacing the Coulomb potential by the pseudopotential in Eq. (78). The entire curve is shifted downwards when the pseudopotential is introduced, which is a manifestation of a weakened scattering. The decrease is 3–5% only, which is consistent with $F(k)$ being close to unity. The difference decreases with electron density and is down to 0.5–1% for $n_e = 10^{20}$ cm^{-3}. We thus find that the Sn^{4+} ions can be treated as approximate point scatterers up to the highest doping levels of interest for window coatings.

Curves (c) and (d) were obtained of use of the Hubbard correction to the RPA and the Singwi–Sjölander approaches, respectively (together with the pseudopotential). It is found that ρ_1 is decreased by about 20% compared with the "pure" RPA result, and that the "knee" is moved towards lower energy. Both of these features are significant for improving the agreement with experimental results. We also observe that the power law applicable between the plasma energy and the band gap no longer yields a clear-cut 3/2 dependence when we invoke ϵ^H or ϵ^{SS}. For the Singwi–Sjölander dielectric function the exponent is ~ -2. This theoretical value of s is still (marginally) consistent with the experimental finding, and there is no reason to reassess the conclusion that ionized impurity scattering provides the main damping in the electron gas.

IX. ANALYSIS OF THE PHONON ABSORPTION

In Sec. V—particularly in Figs. 19, 25, and 26—one may observe some fine structure in the thermal-infrared optical data. It was tentatively ascribed to phonon absorption. In this section we present more detailed information on the phonon effects and also give a parametrization of the phonon susceptibility χ^{PH}. A discussion of phonon effects in In$_2$O$_3$ and In$_2$O$_3$:Sn films was given in Refs. 22 and 203.
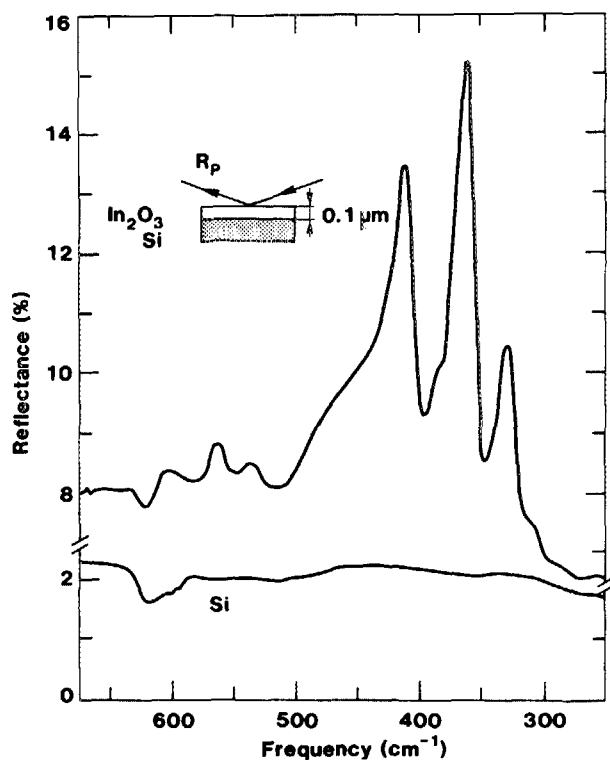
FIG. 40. Spectral reflectance of a bare Si substrate (lower curve) and after coating it with a 0.1-μm-thick film of In_2O_3 (upper curve) whose electron density was $\sim 0.5 \times 10^{20}$ cm^{-3}. The optical measurement used 70° angle of incidence and p-polarized light. The experimental configuration is shown in the inset.

Figure 40 shows high-resolution reflectance data for an In_2O_3 film. The spectrum, given on a wave-number axis, displays three main peaks at 330, 365, and 412 cm^{-1}. These have shoulders at 310, 385, and $\sim$475 cm^{-1}, indicating the presence of weaker structures close to the main peaks. At higher wave numbers, there are three small peaks at 540, 565, and 605 cm^{-1}. All of these structures are believed to correspond to damped transverse phonon polaritons, whose ensuing influence on the optical data is a reflectance maximum.[156] The longitudinal polariton coincides with the plasmon resonance, which is a consequence of the free electrons in In_2O_3. In In_2O_3:Sn, the added free electrons effectively

TABLE IV. Infrared absorption frequencies in In_2O_3 films and particles.

Designation	Film (Fig. 40) (cm^{-1})	Powder (Fig. 41) (cm^{-1})	Powder (Ref. 233) (cm^{-1})
ω_1	605	603	602
ω_2	565	568	568
ω_3	540	541	541
ω_4	$\sim$475*	$\sim$475*	476
ω_5	412	430	420
ω_6	385*	$\sim$377	378
ω_7	365	$\sim$370	370
ω_8	330	335	330
ω_9	310*	310	307
ω_{10}	...	...	244
ω_{11}	...	...	218

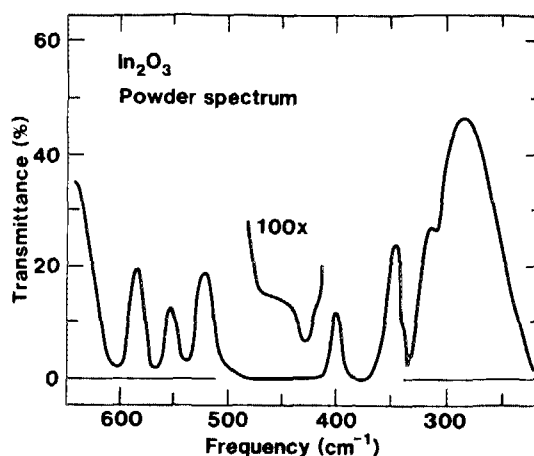*Somewhat uncertain results obtained from "shoulders" in the spectra.

FIG. 41. Spectral transmittance of a KBr pellet containing In_2O_3 particles. Part of the spectrum shows transmittance in 100$\times$ magnification.

screen out the transverse polaritons, so that hardly any observable structure remains in the spectra.

It is of interest to compare the polariton structure with measurements conducted on In_2O_3 particles. To this end we report some data for samples produced by crumbling pieces of the evaporation material, mixing it with infrared-transparent KBr, and consolidating by pressing. Figure 41 shows a transmission spectrum of such a pellet. A number of minima are seen. They stem from phonon absorption and coincide approximately with the reflectance peaks in the film sample. A direct correspondence is not to be expected since the oscillator strengths are different for the particle and film samples and, furthermore, the particle spectra are influenced by the sizes and shapes of the grains.

Table IV shows a compilation of infrared absorption frequencies in In_2O_3 as observed for thin films (Fig. 40) and for powder samples (Fig. 41). The latter data can be compared with results by White and Keramidas,[233] who studied powder specimens similar to the present ones. The three sets of data are found to be in excellent agreement. According to White and Keramidas,[233] a factor group analysis predicts 16 infrared active modes in In_2O_3. It appears that nine of these can be identified in the spectra reported here.

The dielectric function of In_2O_3 was derived in Sec. V C, where the influence of the free electrons was eliminated by computation. The results, given in Fig. 26, show three dominating peaks in ϵ_2, which is clearly consistent with the data in Fig. 40. Hence one may represent χ^{PH} by a sum of three damped Lorentz oscillators according to

$$\chi^{PH} = \sum_{j=1}^{3} \frac{\Omega_j^{PH}}{(\omega_j^{PH})^2 - \omega^2 - i\omega\Gamma_j^{PH}}. \qquad (80)$$

TABLE V. Parameters for the dominating oscillators in χ^{PH}.

Designation	j	ω_j^{PH} (cm^{-1})	Ω_j^{PH} (cm^{-1})	Γ_j^{PH} (cm^{-1})
ω_5	1	412	330	5
ω_6, ω_7	2	365	600	12
ω_8, ω_9	3	330	450	16

The parameters ω_j^{PH}, Ω_j^{PH}, and Γ_j^{PH} were determined by fitting to the experimental results; the specific wave numbers are listed in Table V. Using the designation in Table IV, we see that $j = 1$ corresponds to ω_5, $j = 2$ corresponds to ω_6 and ω_7, and $j = 3$ corresponds to ω_8 and ω_9.

X. APPLICATION TO ENERGY-EFFICIENT WINDOWS

We now turn away from the basic optical properties of a heavily doped semiconductor and regard instead its application to energy-efficient windows. In Sec. X A we bring together the susceptibilities due to bound electrons, free electrons, and phonons into a consistent and fully quantitative model for the optical properties of In_2O_3:Sn. This model is used to optimize the integrated luminous, solar, and thermal performance with regard to film thickness and electron density for a single uniform film on glass. Generally speaking, it is an advantage to increase the transmittance, and to this end we study in Sec. X B In_2O_3:Sn films antireflection coated with MgF_2 and with certain novel[234,235] metal oxyfluoride films. The best tandem coatings showed a luminous transmittance exceeding that of the uncoated glass while the thermal emittance was $\gtrsim 20\%$. The color properties are clearly important for window coatings. This issue, which has been neglected too often in earlier work, is discussed in Sec. X C, where it is shown that a proper antireflection treatment will also lead to a signficant decrease in the iridescence.

A. Computed luminous, solar, and thermal properties of In_2O_3:Sn films

This section is based on Refs. 32 and 203. The starting point is the dielectric function of In_2O_3:Sn in the 0.3–50-μm range, including the band-edge contribution to the valence electron susceptibility as well as the susceptibilities due to the free electrons and the phonons. Specifically, we use χ_{be}^{VE} as in Eq. (44), χ^{FC} as in Eq. (74) [together with $\rho(\omega)$ given by Eq. (59); $\epsilon^{eg} = \epsilon^H$; $\eta = 0.01$], and χ^{PH} as in Eq. (80). The parameter values given in conjunction with these formulas were employed, and ϵ_∞ and m_c^* were as stated in Sec. V C. In the first calculations reported below, the In_2O_3:Sn films were taken to be backed by a medium characterized by a constant refractive index equal to 1.5. This simulates a substrate of glass with low Fe_2O_3 content in the visible and near infrared, or a foil of a polymer such as polyester, polyethylene, etc. In subsequent calculations, the substrate was represented by the dielectric function of amorphous SiO_2 (Ref. 236).

Figure 42 shows spectral normal transmittance and reflectance for a 0.2-μm-thick film with $10^{20} \lesssim n_e \lesssim 3 \times 10^{21}$ cm^{-3}. The band-gap widening, the onset of strong reflectance at a wavelength which scales with n_e, and a gradual disappearance of the phonon-induced structure are all clearly seen. It appears that the best low-emittance coating is obtained with $n_e \simeq 6 \times 10^{20}$ cm^{-3}, and that one would get a very good solar control coating with $n_e \sim 3 \times 10^{21}$ cm^{-3}. The latter value cannot be realized with experimental samples, though.

We wish to assess the films for use on energy efficient windows, and to this end we introduce integrated luminous
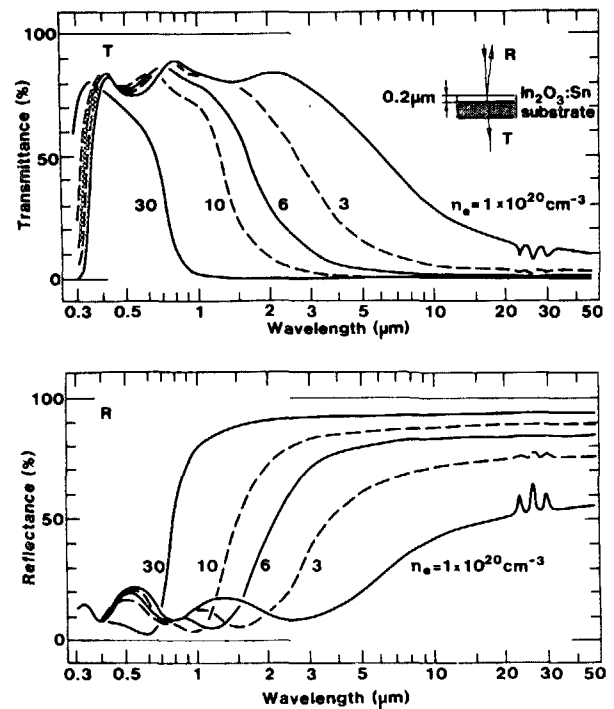

FIG. 42. Spectral normal transmittance (upper part) and reflectance (lower part) as computed from a model for the optical properties of In_2O_3:Sn. The shown values of electron density and film thickness were used.

(lum), solar (sol), and thermal (therm) quantities by the relation

$$X_\gamma = \int d\lambda \, \phi_\gamma(\lambda) X(\lambda) \bigg/ \int d\lambda \, \phi_\gamma(\lambda) . \qquad (81)$$

Depending on which quantity we want to compute, we set ϕ_γ equal to the photopic luminous efficiency of the eye ϕ_{lum} (Ref. 145), the solar irradiance spectrum ϕ_{sol} (Ref. 144), or the blackbody exitance spectrum for 300 K, ϕ_{therm}. The various spectra were shown earlier in the upper part of Fig. 1. X denotes the spectral property: normal transmittance, normal reflectance, or hemispherical emittance E. The emittance was obtained from

$$E(\lambda) = 1 - T_h(\lambda) - R_h(\lambda) , \qquad (82)$$

where T_h is the hemispherical transmittance given by

$$T_h(\lambda) = \frac{1}{2} \int_0^{\pi/2} d(\sin^2 \theta) \, [T_s(\theta,\lambda) + T_p(\theta,\lambda)] , \qquad (83)$$

and an analogous relation holds for the hemispherical reflectance R_h. The subscripts s and p in Eq. (83) refer to different states of polarization.

Figure 43 shows T_{lum} and R_{lum} for In_2O_3:Sn coatings with four thicknesses and $10^{20} \lesssim n_e \lesssim 3 \times 10^{21}$ cm^{-3}. At $n_e < 10^{21}$ cm^{-3} we find $75 \lesssim T_{lum} \lesssim 85\%$ and $10 \lesssim R_{lum} \lesssim 20\%$; the actual magnitudes of these quantities are strongly influenced by optical interference. As the electron density goes up, there is a tendency for R_{lum} to decrease while T_{lum} varies in a more erratic manner. Figure 44 is the counterpart for T_{sol} and R_{sol}. It is seen that T_{sol} decreases and R_{sol} increases when n_e goes up. This can be interpreted as a result of the plasma wavelength which gradually moves
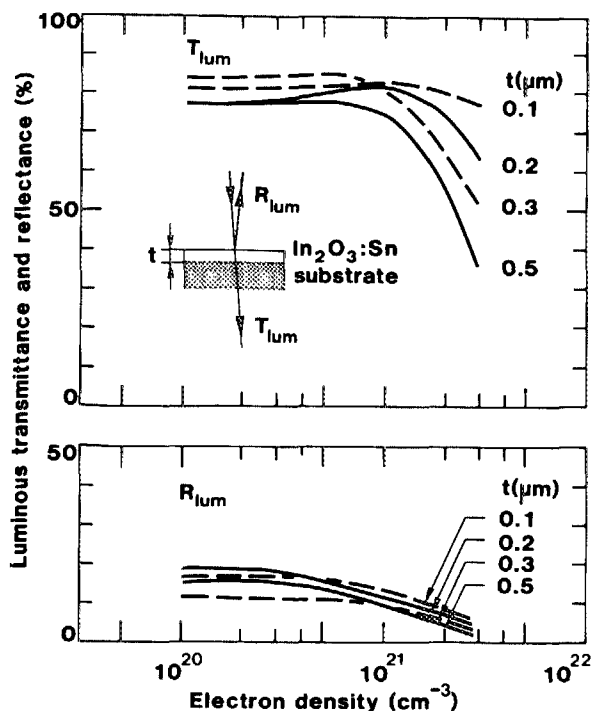
FIG. 43. Luminous normal transmittance (upper part) and reflectance (lower part) vs electron density as computed from a model for the optical properties of In_2O_3:Sn. Results are shown for four film thicknesses.

into the solar spectrum from the infrared side. At $n_e \lesssim 5 \times 10^{20}$ cm^{-3} we have $R_{sol} \approx 13\%$ irrespective of film thickness.

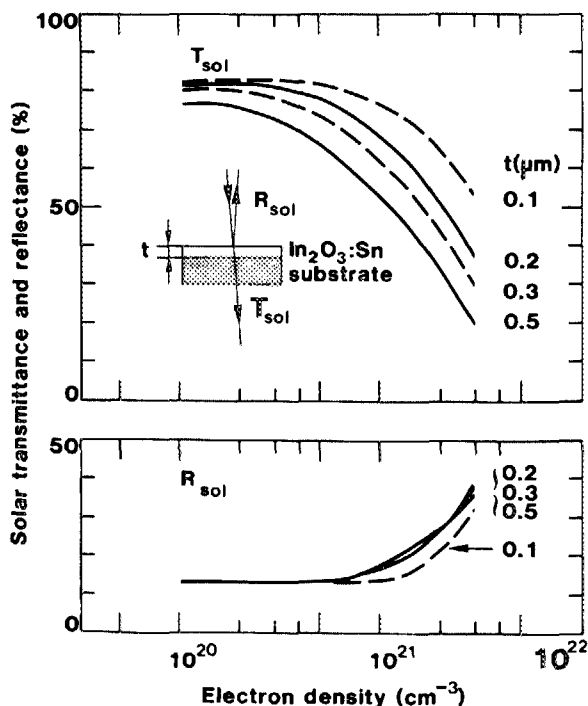Figure 45 reports on hemispherical thermal emittance.

FIG. 44. Solar normal transmittance (upper part) and reflectance (lower part) vs electron density as computed from a model for the optical properties of In_2O_3:Sn. Results are shown for four film thicknesses. The curves for R_{sol} corresponding to 0.2-, 0.3-, and 0.5-μm-thick films are almost overlapping.
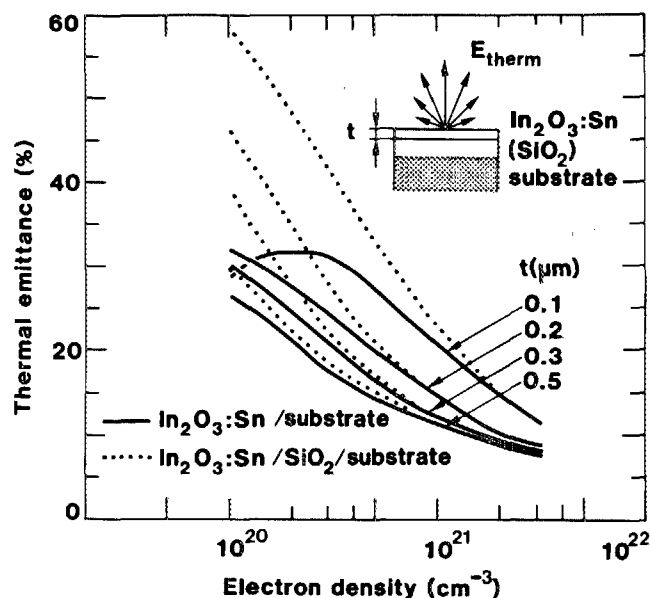

FIG. 45. Thermal hemispherical emittance vs electron density as computed from a model for the optical properties of In_2O_3:Sn. The substrate is taken to be nonemitting with a refractive index equal to 1.5 (solid curve) or having properties given by the dielectric function of amorphous SiO_2 (Ref. 236) (dotted curves). The shown film thicknesses were used.

The solid curves were computed for In_2O_3:Sn films backed by a material having a refractive index of 1.5. This assumption disregards the potential effect of emittance from the substrate, and in order to make valid assessments for a glass window, it is also of interest to study a configuration with an intermediate SiO_2 layer. Its thickness was set to 50 μm, and it was verified through computation that this is sufficient to simulate bulk properties. The dotted curves in Fig. 45 pertain to this latter configuration. Generally, there is a decrease in the emittance as the electron density and the film thickness increase, which is a direct consequence of the increased number of free electrons. The thinnest film shows a somewhat different performance with a peak in the emittance curve referring to In_2O_3:Sn on a transparent substrate; the reason is that the coating becomes partly transparent for the lowest electron densities. We conclude from Fig. 45 that substrate emission is important for $n_e \lesssim 5 \times 10^{20}$ cm^{-3}, but negligible above this electron density provided that the In_2O_3:Sn films are thicker than ~ 0.2 μm. These latter films have $E_{therm} \lesssim 15\%$ for $n_e \approx 10^{21}$ cm^{-3}.

Figures 43–45 show that In_2O_3:Sn films can combine high transmittance of luminous and solar radiation with low thermal emittance, and consequently they are useful for energy-efficient windows. A fully quantitative optimization can only be performed for a specified design of a glazed unit and accounting for nonradiative heat transfer.[237,238] This is outside the scope of this review but it is nevertheless possible to draw some general conclusions. To this end we first fix E_{therm} at a low value. It is not meaningful to diminish it to the extreme, since conductive and convective heat transfer cannot be eliminated in an ordinary gas-filled unit. Specifically, we took E_{therm} to be 15, 20, and 25%. The dotted curves in Fig. 45 yield corresponding electron densities for the investigated film thicknesses, and the pertinent values of T_{sol} can be
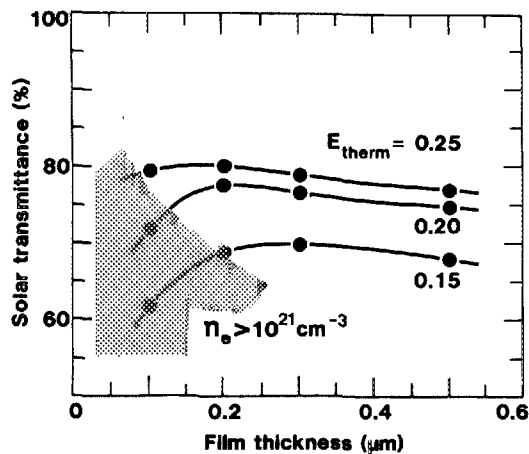
FIG. 46. Normal solar transmittance vs film thicknesses for three values of hemispherical thermal emittance, as computed from a model for the optical properties of In_2O_3:Sn and with the substrate represented by the dielectric function for amorphous SiO_2 (Ref. 236). Curves are drawn only to guide the eye. The shaded area refers to films with $n_e > 10^{21}$ cm^{-3}, which cannot be produced experimentally.

FIG. 47. Spectral normal transmittance and near-normal reflectance as measured for an antireflection-coated In_2O_3:Sn film in the solar and thermal range. T_g and R_g refer to the transmittance and reflectance of the bare glass substrate. The experimental configuration is shown in the inset.

read from Fig. 44. Figure 46 displays solar transmittance as a function of film thickness with E_{therm} as parameter. Requiring $E_{therm} = 15\%$ one cannot exceed $T_{sol} \approx 70\%$, which is undesirably low for many applications. On the other hand, limiting the requirement to $E_{therm} = 20\%$, one can have $T_{sol} \approx 78\%$. At still larger values of E_{therm} it is possible to reach a marginally improved solar transmittance. Optimum performance can be obtained with 0.2-μm-thick In_2O_3:Sn films having $4 \lesssim n_e \lesssim 6 \times 10^{20}$ cm^{-3}. Spectral data for such a film were shown in Fig. 42. The optimization of the luminous properties can be regarded as a separate problem; as we shall see, its solution rests on antireflection treatments.

B. Antireflection-coated In_2O_3:Sn films

It can be inferred from the previous section that T_{lum} is $\lesssim 87\%$ for In_2O_3:Sn films with at least a moderately low thermal emittance. The limitation in transmittance is governed to a large extent by reflection, and it is obvious that an improved performance can be achieved by applying an antireflection coating. Preferrably one should have a quarter-wavelength layer with a refractive index of approximately $(\epsilon_\infty)^{1/4} \approx 1.4$. Some earlier work along these lines has been reported for MgF_2 on In_2O_3:Sn (Refs. 17, 42, 43, and 70) and SiO_2 on doped SnO_2 (Ref. 239). Below we summarize recent results obtained with[18–20] MgF_2 and aluminum oxyfluoride[234,235] (Al-O-F) antireflection layers.

Figure 47 gives an overview over spectral transmittance and reflectance for a sample consisting of a Corning 7059 glass coated with 0.36 μm of $In_2O_3 + 9$ mol % SnO_2 and 0.10 μm of MgF_2. The top layer corresponds to a quarter-wavelength antireflection coating for the midvisible spectrum. MgF_2 was deposited by resistive evaporation from a Mo boat; the substrate was kept at room temperature. The reflectance at $\lambda = 436$ nm was monitored continuously during the MgF_2 evaporation by use of a photodiode, and the deposition was stopped when the reflectance was close to a minimum. It is seen from Fig. 47 that $T_{lum} \approx 92\%$ for the
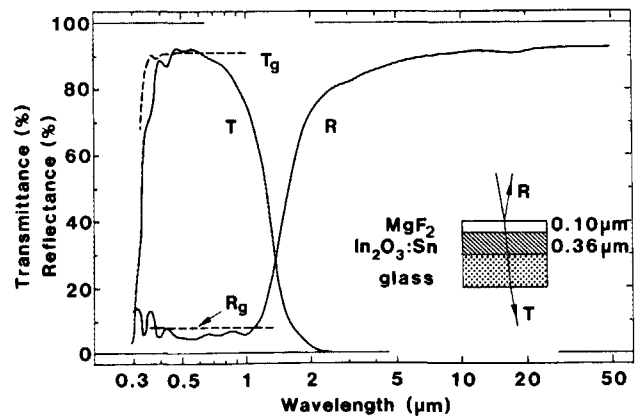
coated glass, which is marginally higher than for the uncoated glass, and that $R_{lum} \approx 6\%$, which is noticeably lower than for the uncoated glass.

The optical properties in the visible range are studied in more detail in Fig. 48, where normal transmittance through another MgF_2-coated $In_2O_3 + 9$ mol % SnO_2 film is shown. Application of a 0.27-μm-thick In_2O_3:Sn film leads to a lowered transmittance with pronounced oscillations due to optical interference. After overcoating with 0.09 μm of MgF_2 we note two important results: the transmittance of the coated glass is higher than for the uncoated glass across almost the entire visible part of the spectrum, and the interference effects become much less manifest. Both of these effects are important for window coatings; the enhanced transmission is of obvious significance for unobstructed viewing and for solar energy transmission, whereas the diminished interference leads to less perceived color. Furthermore, a

FIG. 48. Normal spectral transmittance as measured for an antireflection coated In_2O_3:Sn film in the luminous range. The curves refer to the uncoated glass, the In_2O_3:Sn-coated glass, and after a final deposition of MgF_2. The experimental configuration is shown in the inset.

FIG. 49. Spectral infrared reflectance for an In_2O_3:Sn film with and without an MgF_2 antireflection layer. The curves refer to 45° angle of incidence of s- and p-polarized light. The experimental configuration is shown in the inset.
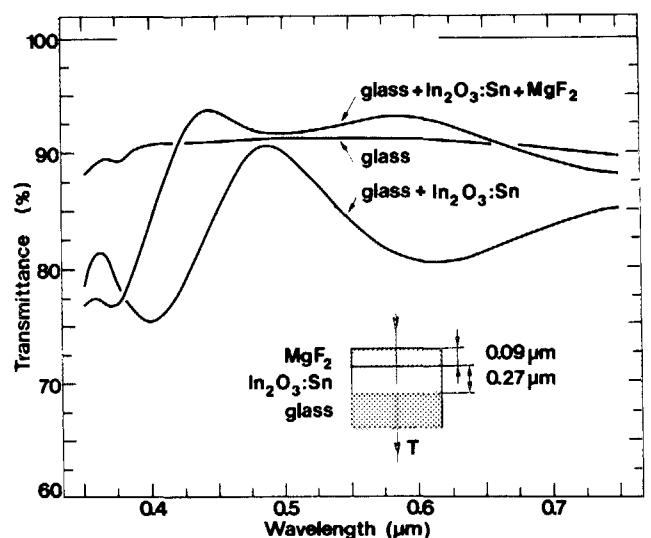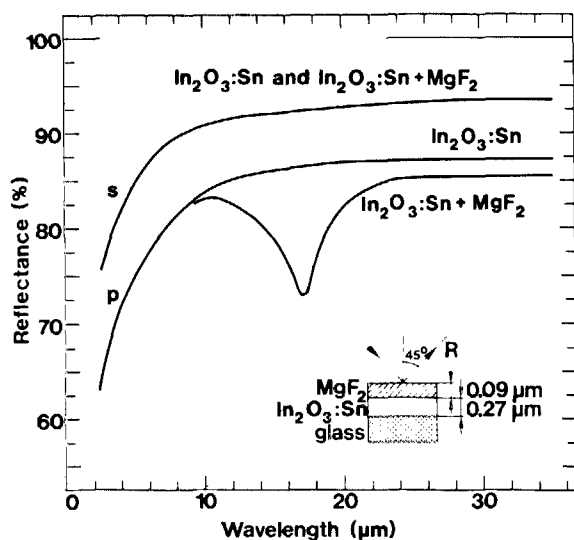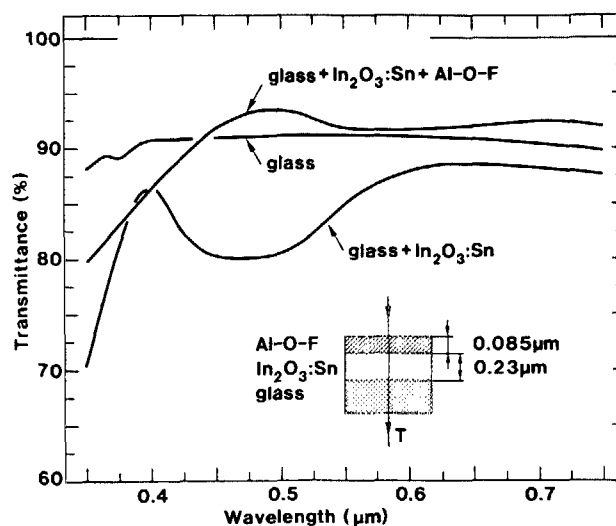

FIG. 50. Normal spectral transmittance as measured for an antireflection-coated In_2O_3:Sn film in the luminous range. The curves refer to uncoated glass, the In_2O_3:Sn-coated glass, and after a final deposition of aluminum oxyfluoride (Al-O-F). The experimental configuration is shown in the inset.

low luminous reflectance is needed in order to fulfill building regulations in some parts of the world.

The antireflection coating deteriorates the thermal properties to some extent. This effect was checked by measurement of the infrared reflectance for the coating which was earlier reported on in Fig. 48. Figure 49 shows results for 45° angle of incidence of s- and p-polarized light. The s-polarized light yields the same reflectance before the after application of the MgF_2 layer. For p-polarized light, however, there is a clear minimum around $\lambda \approx 17$ μm which stems from absorption in MgF_2. These results are consistent with the published[240] dielectric function of crystalline MgF_2. We may conclude that the antireflection layer increases the hemispherical thermal emittance by no more than a few percent.

We now regard the antireflection layer from a practical point of view. In principle, the earlier studied evaporated MgF_2 films can be applied to large substrates, but an alternative technique, such as high-rate reactive dc planar magnetron sputtering, may be more economic for production. Aluminum oxyfluoride, which can be made by the latter technique,[234,235] appears to have properties which makes this material very well suited for antireflection of In_2O_3:Sn. The Al-O-F coatings were produced by dc sputtering from an aluminum target in a reactive gas containing oxygen and carbon tetrafluoride. The deposition rate was as high as 3.4 ± 0.1 nm/s. The optical properties were characterized by $n \lesssim 1.60$ and $k \lesssim 10^{-3}$ for the pertinent wavelengths. Figure 50 shows normal transmittance through an Al-O-F-coated $In_2O_3 + 9$ mol % SnO_2 film on a Corning 7059 glass substrate. It is plotted in the same way as in Fig. 48. We see that with 0.23 μm of In_2O_3:Sn and 0.085 μm of Al-O-F, the transmittance of the coated glass is higher than for the uncoated glass across the main part of the visible spectrum. Some experiments were performed also with a 0.28-μm-thick In_2O_3:Sn film, having a thickness which yields maximum T_{lum}. Application of 0.10 μm of Al-O-F gives some improvement in T_{lum}, albeit not as large as for the 0.23-μm-thick film reported in Fig. 50.

C. Color properties

The color produced by applying a coating to a transparent substrate is important if the final product is to be used as a window. The requirements are most stringent for reflected light. We feel that color properties have not received proper attention in much of the earlier work on transparent infrared reflectors, although there are exceptions (for example, in Ref. 138). Below we summarize a colorimetric analysis of $In_2O_3 + 9$ mol % SnO_2 films with and without antireflection treatment. Much of the presentation is based on Refs. 21 and 235. We use the CIE Colorimetric System[241-246] (the CIE 1931 2° Standard Observer).

The purpose of colorimetric analysis is to give color specifications for observers with normal vision in terms of tristimulus values or chromaticity coordinates. The ideal observer's color-matching functions are shown in the inset of Fig. 51. They are denoted $\bar{x}$, $\bar{y}$, and $\bar{z}$, and represent red, green, and blue primaries, respectively. One can describe any color as an additive mixture of these. The $\bar{y}$ curve is chosen so that it coincides with the relative luminous efficiency of the light-adapted eye (cf. Fig. 1). The CIE tristimulus values $(X_{CIE}, Y_{CIE}, Z_{CIE})$, corresponding to a certain color stimulus $\psi(\lambda)$, are obtained from

$$X_{CIE} = k_{CIE} \int d\lambda \, \psi(\lambda) \, \bar{x}(\lambda) , \qquad (84)$$

and analogously for Y_{CIE} and Z_{CIE}. The color stimuli are

$$\psi(\lambda) = \begin{cases} S(\lambda) \, T(\lambda) , & (85a) \\ S(\lambda) \, R(\lambda) , & (85b) \end{cases}$$

for transmitted and reflected light, respectively, where $S(\lambda)$ is the relative spectral irradiance function of the illuminant which irradiates the object. The constant k_{CIE} is given by

$$k_{CIE} = \left(\int d\lambda \, S(\lambda) \, \bar{y}(\lambda) \right)^{-1} , \qquad (86)$$

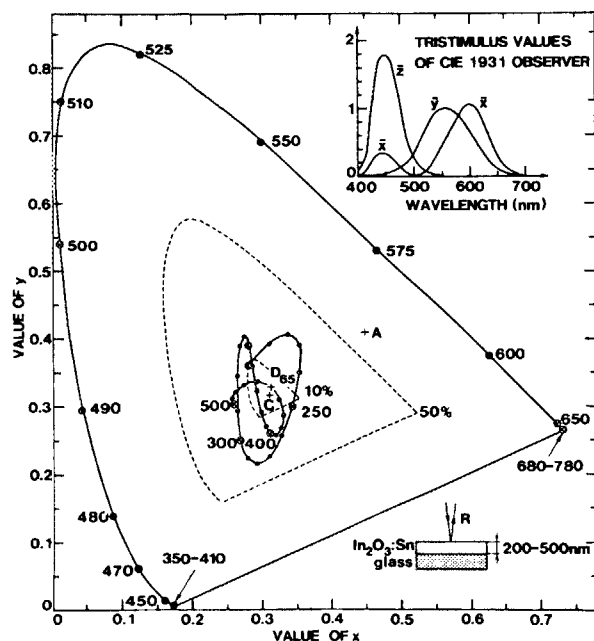so that Y_{CIE} yields T_{lum} or R_{lum}. Chromaticity coordinates

FIG. 51. CIE 1931 (x, y) chromaticity diagram with wavelength (in nanometers) marked along the spectrum locus (solid curve). The solid straight line connecting the ends of the spectrum locus is known as the "purple line." Chromaticity coordinates for three standard illuminants are indicated by crosses. The dashed curves refer to 10 and 50% excitation purity with regard to illuminant C. The solid curve near the center of the figure represents the locus of normally reflected light from an In_2O_3:Sn film on glass, irradiated by illuminant C, as the film thickness is varied between 200 and 500 nm. Chromaticities corresponding to 10-nm-thickness increments are marked on the curve. The upper inset depicts the color matching functions $\bar{x}$, $\bar{y}$, and $\bar{z}$ for the CIE 1931 Standard Observer.

are obtained from

$$x = X_{CIE} (X_{CIE} + Y_{CIE} + Z_{CIE})^{-1} \qquad (87)$$

and correspondingly for y and z. These formulas lead to the

chromaticity diagram in the main part of Fig. 51. Any color can be represented as a point within the shown boundary (closed solid curve).

The CIE Colorimetric System defines a number of standard illuminants with specified $S(\lambda)$ functions. For window applications it is appropriate to use illuminant C, representing daylight with a correlated color temperature of 6774 K. Alternatively, one could be illuminant D_{65} with 6504-K color temperature. Colors seen in incandescent light can be described by use of illuminant A, which approximates the light from a tungsten lamp. The chromaticities of these three illuminants are shown as crosses in Fig. 51. We also introduce an excitation purity, which is defined as the ratio between two lengths in the chromaticity diagram; the first length is between the chromaticity of illuminant C and that of the color considered, and the second length is in the same direction from the first point to the spectrum locus. The dashed curves in Fig. 51 denote 10 and 50% excitation purity.

Table VI gives colorimetric quantities for In_2O_3:Sn with and without MgF_2 (as reported in Fig. 48), and for In_2O_3:Sn with and without Al-O-F (as reported in Fig. 50). We also include results for a thicker In_2O_3:Sn film with and without Al-O-F. Without exception, the antireflection coating leads to a significant decrease in the excitation purity—i.e., to less perceived color—and to an improvement of the luminous value. The improvement is most striking for the first set of data; it is demonstrated that the MgF_2 layer has the effect of reducing the excitation purity from 2.2 to 0.6% for transmitted light and from 25.4 to 8.5% for reflected light. Further, the MgF_2 gives an increase of T_{lum} from 87.4 to 94.6% and a decrease of R_{lum} from 12.4 to 5.2%.

Colorimetric analysis is important for assessing (and minimizing) the color of a coating with regard to its thickness. To this end one needs the dielectric functions of the constituent materials: for $In_2O_3 + 9$ mol % SnO_2 we relied

TABLE VI. Colorimetric quantities for spectral transmittance $T(\lambda)$ and reflectance $R(\lambda)$ of In_2O_3:Sn films with and without antireflection coatings. Thicknesses are given in parentheses. The data are based on the CIE 1931 Standard Observer and Illuminant C.

| Color stimulus		Optical data	Chromaticity coordinates		Excitation purity (%)	Luminous value (%)
Coating			x	y		
In_2O_3:Sn $(0.27\,\mu m)$		$T(\lambda)$	0.3073	0.3268	2.2	87.4
		$R(\lambda)$	0.3245	0.2601	25.4	12.4
	$+ MgF_2$ $(0.10\,\mu m)$	$T(\lambda)$	0.3111	0.3177	0.6	94.6
		$R(\lambda)$	0.2895	0.3022	8.5	5.2
In_2O_3:Sn $(0.23\,\mu m)$		$T(\lambda)$	0.319	0.316	2.6	84.2
		$R(\lambda)$	0.257	0.326	12	13.2
	$+ Al\text{-}O\text{-}F(0.085\,\mu m)$	$T(\lambda)$	0.311	0.319	1.0	92.0
		$R(\lambda)$	0.323	0.324	6	6.7
In_2O_3:Sn $(0.28\,\mu m)$		$T(\lambda)$	0.318	0.336	5.6	89.1
		$R(\lambda)$	0.308	0.252	26	8
	$+ Al\text{-}O\text{-}F$ $(0.10\,\mu m)$	$T(\lambda)$	0.316	0.322	2.6	91.9
		$R(\lambda)$	0.282	0.284	14	5.6
Illuminant C			0.3101	0.3163	0	$\cdots$
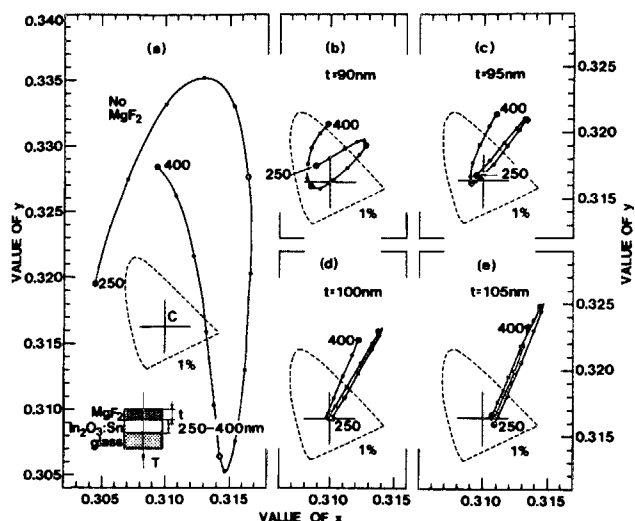
FIG. 52. Solid curves show the CIE 1931 (x, y) chromaticity coordinates for normal transmission of daylight (standard illuminant C) through an In_2O_3:Sn film (250–400 nm thickness) antireflected by MgF_2 (0,90,95,105 nm thickness) on glass. Chromaticities corresponding to 10-nm-thickness increments of In_2O_3:Sn are marked on the curves.

on the values given in Sec. V B, for MgF_2 we found from optical measurements that $\epsilon = 1.90 + i0$ which is consistent with literature results,[247] and for Corning 7059 glass we used[248] $\epsilon = 2.34 + i0$. These data were employed to compute spectral transmittance and reflectance for visible wavelengths, from which the chromaticity coordinates were derived. We used the selected ordinate technique (see, for example, Ref. 246) to evaluate the integrals in Eq. (84).

Figures 52 and 53 show chromaticity plots for transmittance and reflectance, respectively, when the In_2O_3:Sn thickness is varied between 0.25 and 0.40 μm and the MgF_2 has
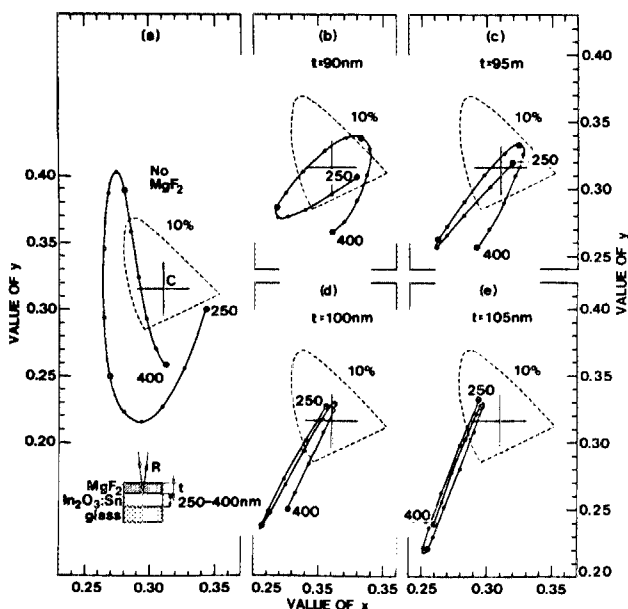

FIG. 53. Solid curves show the CIE 1931 (x, y) chromaticity coordinates for normal reflection of daylight (standard illuminant C) from an In_2O_3:Sn film (250–400-nm thickness) antireflected by MgF_2 (0,90,95,100,105 nm thickness) on glass. Chromaticities corresponding to 10-nm-thickness increments of In_2O_3:Sn are marked on the curves.

different thicknesses—either zero or one of four different values chosen to lie around the thickness required for a quarter-wavelength antireflection coating for visible light. It is seen that the single In_2O_3:Sn film can produce a variety of colors both in transmission and in reflection. The excitation purity can be as large as 6% for transmitted light and 38% for reflected light. Application of the MgF_2 makes the excitation purity go down, and substantial parts of the curves lie inside the 1% and the 10% limits, respectively. From the shown plots, is is found that an excitation purity < 1% in transmission and < 10% in reflection can be realized with In_2O_3:Sn thicknesses in the 0.22–0.26- and 0.335–0.365-μm ranges if these films are coated with 0.09–0.105 μm of MgF_2. Fixing the MgF_2 thickness at 0.1 μm, one obtains a constant yellow (0.570 $< \lambda <$ 0.574 μm) color in transmission and a constant blue (0.469 $< \lambda <$ 0.473 μm) color in reflection within an In_2O_3:Sn thickness interval as large as 0.27–0.33 μm. The chromaticity data in Table VI are consistent with the theoretical estimates in Figs. 52 and 53.

In practical situations, the coated windows are to be viewed under varying off-normal angles, and hence it is of interest to study the chromaticities for color stimuli corresponding to oblique incidence. To this end, Eq. (85) was replaced by

$$\phi_\theta(\lambda) = \begin{cases} S(\lambda) \left[T_s(\theta, \lambda) + T_p(\theta, \lambda) \right]/2, & (88a) \\ S(\lambda) \left[R_s(\theta, \lambda) + R_p(\theta, \lambda) \right]/2, & (88b) \end{cases}$$

with θ being a fixed angle of incidence. Computations analogous to those leading to Figs. 52 and 53 showed[21] that the changes in the chromaticities were rather small for $\theta \lesssim 30°$.

We remark, finally, that when assessing the practical usefulness of window coatings one should consider criteria on color discrimination[242,243,246] rather than on excitation purity. Unfortunately, color discrimination is a difficult subject for objects that are to be viewed in a variety of different conditions, and no readily applicable results are known to us. We observe, however, that the strongest variations of the chromaticities for optimized antireflection coated In_2O_3:Sn films take place in a direction around $\sim 60°$ from the x axis in the CIE 1931 (x, y) diagram. This coincides approximately with the major axes in the MacAdam discrimination ellipses[242,243,246] in the pertinent area of the chromaticity diagram.

XI. SUMMARY AND REMARKS

We have reviewed work on In_2O_3:Sn films produced by reactive e-beam evaporation onto heated glass. The technique is capable of yielding such coatings of unsurpassed quality, although films prepared in other ways may have similar properties. A disadvantage may be the difficulty of preparing highly uniform coatings over extended surfaces. These problems are surmountable, though, and evaporation is in fact used industrially to produce In_2O_3:Sn coatings on glass. For very large surfaces—for example, for windows in commerical buildings, etc.—it may be more cost effective to work with another technique such as sputtering or chemical vapor (spray) deposition. The best film quality was obtained for evaporation of In_2O_3 + 9 mol % SnO_2 with the following process parameters: deposition rate ~ 2 nm/s, substrate

temperature $\gtrsim 150\,^\circ$C, and oxygen pressure $\sim 5 \times 10^{-4}$ Torr. The substrate temperature is adequate for coating window glass, but an alternative, such as ion-assisted evaporation or magnetron sputtering, may be required for coating plastic foil. Superior optical and electrical properties occurred in films with crystallite dimensions $\gtrsim 50$ nm and a C-type rare-earth oxide structure. The electron diffractograms contained some "extra" rings, which ought to have been extinct in bulklike films. They are expected to contain information on the structural properties, but their implications have not yet been disentangled.

Optical properties in the 0.2–50-μm wavelength range are of central importance. Experimental studies showed that an increase in the doping had several effects: the semiconductor band gap (in the ultraviolet) shifted towards shorter wavelengths, the infrared reflectance was enhanced, and a set of absorptance peaks (in the thermal infrared) vanished. Heavily doped In_2O_3:Sn films with thicknesses of $\sim 0.3\,\mu$m displayed high luminous transmittance and high infrared reflectance and hence are of interest as window coatings. The best films had a dc resistivity of $\sim 2 \times 10^{-4}\,\Omega$ cm and a mobility of ~ 30 cm^2/V s. Microwave reflectance was found to correlate well with long-wavelength infrared reflectance.

The optical performance was discussed in terms of a complex dielectric function, which was extracted from the spectrophotometric data by computation. In order to secure reliable results we paid particular attention to the proper selection of input data, to numerical accuracy, and to internal consistency. A preliminary analysis was performed within the classical Drude theory. By choosing suitable values of plasma frequency and relaxation frequency, one could obtain an approximate description of the dielectric function in the main spectral range. However, the Drude theory gives neither the magnitude nor the energy dependence of the relaxation frequency. These facts, together with the need to account for band-gap shifts and infrared absorption maxima by other notions, made it obvious that one has to go beyond the Drude model in order to understand the optical properties.

A quantitative model for the optical properties of In_2O_3:Sn must encompass the combined effects of valence electrons, free electrons, and phonons. A separation into elementary excitations is natural since the corresponding resonances take place at widely different energies. A band-structure model was suggested for the undoped In_2O_3 host crystal. It comprises oppositely curved isotropic and parabolic bands separated by a direct energy gap of 3.75 eV. In the present films, the doping is so large that the Mott critical density is exceeded. The tin impurities are then singly ionized, and the associated electrons occupy the bottom of the conduction band in the form of a free-electron gas. The substitutionally incorporated tin ions behave effectively as point scatterers, which can be understood from the similarity of the pseudopotentials for Sn^{4+} and In^{3+}. Screening of the ions could be accounted for by the random phase approximation, which works well since the effective electron radius [r_s^* in Eq. (68)] is small. Exchange and correlation plays a small, though not entirely negligible, role. Phonon effects were included by empirically determined damped Lorentz oscillators. They are confined to a part of the far-infrared range.

Interband transitions give strong absorption at $\gtrsim 4$ eV. The band gap is widened by as much as ~ 0.6 eV as a consequence of the doping. This can be understood quantitatively as the net result of two competing effects: a band-gap widening due to the blocking of the lowest states in the conduction band (i.e., a Burstein–Moss effect), and a band-gap narrowing due to electron-electron and electron-ion scattering. The scattering may also account for the transition width. The band gaps displayed logarithmic tails towards low energy. It is surprising that the significance of band-gap narrowing has not been appreciated in earlier work on In_2O_3:Sn despite the fact that such an effect has been widely discussed[195–198,249] in the context of heavily doped Si for microelectronic device applications.

In the main spectral range, the optical properties are governed by the presence of free electrons. An analysis of the complex dynamic resistivity showed unambiguously that singly ionized tin atoms were the most efficient scatterers for the free electrons, although we found some evidence that other types of scattering (for example, grain-boundary scattering) could play a role in the midvisible range. The small influence of lattice defects is a consequence of the high degree of crystallinity. Since the ions must be present in order to produce the electron gas—and hence an onset of metallic-like properties around the plasma energy—we may state that the optical performance of the best In_2O_3:Sn films is approaching the theoretical limit.

Between the energy gap and the plasma energy, the real part of the dynamic resistivity obeys a power law and is proportional to ω^s. For ionized impurity scattering the exponent lies between $-3/2$ and ~ -2, depending on the model used for screening in the electron gas. Clearly one should be hesitant to draw conclusions on the dominant scattering mechanism from observations of small departures of s from $-3/2$. We note in this connection that in recent work[250] on crystalline electrochromic WO_3 one has observed $s \approx -2$ and speculated that monopole dislocations yield important scattering. The arguments above cast some doubt on this suggestion.

Figure 54 summarizes several of the most important results from the theoretical analysis and presents an overview of the fundamental physical properties and mechanisms on a logarithmic wavelength scale. The band gap (E_g), the plasma energy ($\hbar\omega_p$), and a typical phonon energy ($\hbar\omega_{PH}$) are shown. We have $\hbar\omega_p \lesssim 1$ eV, but the question remains whether the plasma energy could be pushed further towards the visible by enhancing the electron density. One may consider increasing the Sn content, but this is expected to lead to unwanted electron scattering against Sn-containing complexes, and work by Köstlin et al.[83] indicates that $In_2O_3 + 9$ mol % SnO_2 is not far from the optimum composition. By preparing films under reducing conditions one might hope to obtain additional free electrons by oxygen vacancies or, possibly, by interstitial In. The maximum electron density of In_2O_3-based coatings cannot be conclusively given, but it does not appear likely that values much above 10^{21} cm^{-3} can be realized.
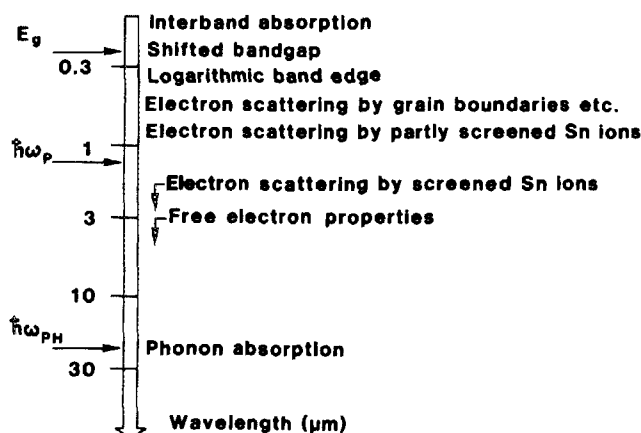
Eg —→
0.3 —
ħωₚ — 1 —
3 —
10 —
ħω_PH —→
30 —

Interband absorption
Shifted bandgap
Logarithmic band edge
Electron scattering by grain boundaries etc.
Electron scattering by partly screened Sn ions
Electron scattering by screened Sn ions
Free electron properties
Phonon absorption

Wavelength (μm)

FIG. 54. Overview of fundamental physical properties and mechanisms for high-quality In_2O_3:Sn films.

The theoretical model for the optical properties was used to optimize the luminous, solar, and thermal performance of window coatings by computation. A single In_2O_3:Sn film on glass could yield $\sim 78\%$ normal solar transmittance combined with $\sim 20\%$ hemispherical thermal emittance. Substrate emittance is of little concern for such films. Antireflection coating (for example, by a novel high-rate sputtered aluminum oxyfluoride material) could lead to a significant boost of the luminous performance, and optimized coatings had $\sim 95\%$ normal luminous transmittance and $\sim 5\%$ normal luminous reflectance. The antireflection treatment is important also for diminishing potential iridescence effects, and a color purity $< 1\%$ in normal transmission and $< 10\%$ in normal reflection (with regard to a daylight illuminant) could be achieved for extended ranges of film thickness.

The optical properties of In_2O_3:Sn films make them very well suited as window coatings and also for a variety of other applications. For some of these it is adequate to have a single In_2O_3:Sn layer, whereas for other applications such a film has to be integrated in a multilayer coating. High transmission of solar radiation (particularly in the visible range) and low emittance of thermal radiation makes it possible to devise windows which can provide important heating of buildings in cold climates. The possibility to have heavily doped oxide semiconductor coatings that are virtually nonabsorbing for visible light is a special advantage which cannot be matched by alternative metal-based coatings. Iridescence has plagued earlier oxide-type window coatings. This has led manufacturers to use film thicknesses that are much larger than those required to obtain a desired low thermal emittance, which is of course inefficient in terms of materials utilization and process time. Antireflection of thin In_2O_3:Sn films gives distinct improvements of their color properties.

A related application regards efficient solar collectors. Conventionally, one works here with nontransparent surfaces with high solar absorption and low thermal emission placed under convection shields of glass or plastic.[251] An alternative concept is to have a nonselectively solar-absorbing surface under a coated convection shield which transmits solar radiation and reflects thermal radiation back to the absorber. It is imperative to have maximum solar trans-

mittance of such a coating. An advantage of the second concept is that the spectrally selective coating does not have to operate at high temperature, and hence it would not be prone to degradation. However, the production of high-quality selectively solar-absorbing coatings is now an established technology,[252] and it is not obvious that selective transmission would offer any significant improvement.

In_2O_3:Sn coatings can be of interest also for combining luminous transmission with reflection of near-infrared radiation. The electron density cannot be increased to an extent that the plasma wavelength lies at $\sim 0.7 \mu$m, but encouraging results have been found recently by integrating In_2O_3:Sn films in a multilayer coating[253] (similar data have been reported for SnO_2:F-based multilayers[254] and for some all-dielectric $TiO_2/SiO_2/TiO_2$...multilayers[255]). Coatings with this performance are of considerable interest as solar control films on windows in buildings and vehicles, for decreasing the temperature of oven windows, for some laser applications, and for providing energy efficiency of incandescent and fluorescent light sources.[256] We note in this connection that improved thermal insulation of sodium lamps was achieved by doped In_2O_3 films[129] many years ago. The ability to reflect in the gigahertz range is significant for microwave ovens and for some radar applications.

The combination of high short-wavelength transmittance and low electrical resistivity is of interest of many applications including heating and frost prevention of windows (in aircraft, automobiles, locomotives, ship bridges, showcases, frozen food merchandise, etc.) transparent front-surface electrodes (in solar cells, display devices employing liquid crystals, electroluminescent materials or electrochromic materials, etc.), electromagnetic shielding (on computer terminal screens, of delicate electronic equipment designed to work in adverse environments, etc.), and antistatic treatments. Schottky barrier solar cells is still another area for use. Window applications have been in focus for this article, and we end by drawing attention to the possibility of having In_2O_3:Sn as extended electrodes in electrochromic "smart windows"[257] with dynamic control of radiant energy.[250,257–261]

The work reviewed in this paper has dealt almost exclusively with doped In_2O_3, but it is expected that many of the results and conclusions—experimental as well as theoretical—are approximately valid also for coatings based on crystalline ZnO, CdO, SnO_2, WO_3, Cd_2SnO_4, and perhaps others. An extention to other heavily doped oxide semiconductors could be motivated on several grounds. Theoretically, it would be highly relevant to test the models outlined in this review for the optical properties on a material whose bandstructure is well known. Experimentally, one should realize that In is not an abundant metal, and price may restrict the use of In_2O_3-based coatings on a very large scale.

band-gap widening described in Secs. VII B and C. The aluminum oxyfluoride films reported on in Secs. X B and C were developed in our laboratory by G. L. Harding. A. Hjortsberg, who is now at ASEA Research and Innovation, Västerås, Sweden, had a significant impact on our initial studies. Microanalysis was carried out with the help of L. Falk, H.-O. Andrén and G. Wirmark at Chalmers. Many important and enlightening discussions were held with U. Kreibig, Universität des Saarlandes, Saarbrücken, Germany, and with H. P. Myers, P.-O. Nilsson, G. A. Niklasson, T. S. Eriksson, J. S. E. M. Svensson, and others at Chalmers. Technical assistance was received from P.-O. Gustafsson, E. Guttenberg, S. Pehrson, and others. The work was financially supported by grants from the Swedish Natural Science Research Council and the National Swedish Board for Technical Development.

[1]E. Ritter, in *Progress in Electro-Optics*, edited by E. Camatini (Plenum, New York, 1975).

[2]S. D. Berman and S. D. Silverstein, in *Proceedings of the Conference on Efficient Use of Energy*, edited by K. W. Ford *et al.* [AIP Conf. Proc. 25, 286 (1975)].

[3]Z. M. Jarzebski and J. P. Marton, J. Electrochem. Soc. 123, 199C (1976); 123, 299C (1976); 123, 333C (1976).

[4]J. L. Vossen, Phys. Thin Films 9, 1 (1977).

[5]G. Haacke, Annu. Rev. Mater. Sci. 7, 73 (1977).

[6]C. G. Granqvist, Appl. Opt. 20, 2606 (1981).

[7]C. M. Lampert, Solar Energy Mater. 6, 1 (1981).

[8]Z. M. Jarzebski, Phys. Status Solidi A 71, 13 (1982).

[9]H. Köstlin, Festkörperprobleme 22, 229 (1982).

[10]J. C. Manifacier, Thin Solid Films 90, 297 (1982).

[11]K. L. Chopra, S. Major, and D. K. Pandya, Thin Solid Films 102, 1 (1983).

[12]N. Rücker and K. J. Becker, Thin Solid Films 53, 163 (1978).

[13]P. Nath and R. F. Bunshah, Thin Solid Films 69, 63 (1980).

[14]P. Nath, R. F. Bunshah, B. M. Basol, and O. M. Staffsud, Thin Solid Films 72, 463 (1980).

[15]Ki-Seon Lee, J. Korean Inst. Electr. Eng. 17, 43 (1980).

[16]H. -U. Habermeier, Thin Solid Films 80, 157 (1981).

[17]J. Ebert, Proc. Soc. Photo-Opt. Instrum. Eng. 325, 29 (1982).

[18]I. Hamberg, A. Hjortsberg, and C. G. Granqvist, Appl. Phys. Lett. 40, 362 (1982).

[19]A. Hjortsberg, I. Hamberg, and C. G. Granqvist, Thin Solid Films 90, 323 (1982).

[20]I. Hamberg, A. Hjortsberg, and C. G. Granqvist, Proc. Soc. Photo-Opt. Instrum. Eng. 324, 31 (1982).

[21]I. Hamberg and C. G. Granqvist, Appl. Opt. 22, 609 (1983).

[22]I. Hamberg and C. G. Granqvist, Thin Solid Films 105, L83 (1983).

[23]K. D. J. Christian and S. R. Shatynski, Thin Solid Films 108, 319 (1983); Appl. Surf. Sci. 15, 178 (1983).

[24]S. Maniv, C. J. Miner, and W. D. Westwood, J. Vac. Sci. Technol. A 1, 1370 (1983).

[25]Z. Ovadyahu, B. Ovryn, and H. W. Kraner, J. Electrochem. Soc. 130, 917 (1983).

[26]L. Assadourian and L. S. Herczeg, Appl. Opt. 23, 1452 (1984); 23, 3500 (1984).

[27]I. Hamberg and C. G. Granqvist, Appl. Phys. Lett. 44, 721 (1984).

[28]I. Hamberg, C. G. Granqvist, K. -F. Berggren, B. E. Sernelius, and L. Engström, Phys. Rev. B 30, 3240 (1984).

[29]I. Hamberg and C. G. Granqvist, Proc. Soc. Photo-Opt. Instrum. Eng. 428, 2 (1983); Solar Energy Mater. 11, 239 (1984).

[30]I. Hamberg and C. G. Granqvist, in *Solar World Congress*, edited by S. V. Szokolay (Pergamon, Oxford, 1984), p. 1948.

[31]I. Hamberg, C. G. Granqvist, K. -F. Berggren, B. E. Sernelius, and L. Engström, Proc. Soc. Photo-Opt. Instrum. Eng. 502, 2 (1984); Solar Energy Mater. 12, 479 (1985).

[32]I. Hamberg and C. G. Granqvist, Appl. Opt. 24, 1815 (1985).

[33]S. Noguchi, M. Mizuhashi, and H. Sakata, Rep. Res. Lab. Asahi Glass Co. 28, 25 (1978).

[34]M. Mizuhashi, Thin Solid Films 70, 91 (1980); 76, 97 (1981).

[35]M. Mizuhashi, Jpn. J. Appl. Phys. 22, 615 (1983).

[36]R. Aitchison, Aust. J. Appl. Sci. 5, 10 (1954).

[37]Y. T. Sihvonen and D. R. Boyd, Rev. Sci. Instrum. 31, 992 (1960).

[38]R. R. Mehta and S. F. Vogel, J. Electrochem. Soc. 119, 752 (1972).

[39]W. W. Molzen, J. Vac. Sci. Technol. 12, 99 (1975).

[40]J. A. Thornton and V. L. Hedgcoth, J. Vac. Sci. Technol. 13, 117 (1976).

[41]J. B. DuBow, D. E. Burk, and J. R. Sites, Appl. Phys. Lett. 29, 494 (1976).

[42]Y. Ohhata and S. Yoshida, Oyo Butsuri 46, 43 (1977).

[43]S. Yoshida, Appl. Opt. 17, 145 (1978).

[44]K. Itoyama, J. Electrochem. Soc. 126, 691 (1979).

[45]J. C. C. Fan, Appl. Phys. Lett. 34, 515 (1979); Thin Solid Films 80, 125 (1981).

[46]Y. Ohhata, F. Shinoki, and S. Yoshida, Thin Solid Films 59, 255 (1979).

[47]W. T. Pawlewicz, I. B. Mann, W. H. Lowdermilk, and D. Milam, Appl. Phys. Lett. 34, 196 (1979).

[48]A. J. Steckl and G. Mohammed, J. Appl. Phys. 51, 3890 (1980).

[49]M. Buchanan, J. B. Webb, and D. F. Williams, Appl. Phys. Lett. 37, 213 (1980).

[50]P. C. Karulkar and M. E. McCoy, Thin Solid Films 89, 259 (1981).

[51]F. T. J. Smith and S. L. Lyu, J. Electrochem. Soc. 128, 2389 (1981).

[52]R. Tueta and M. Braguer, Thin Solid Films 80, 143 (1981).

[53]R. P. Howson and M. I. Ridge, Thin Solid Films 77, 119 (1981).

[54]M. I. Ridge, M. Stenlake, R. P. Howson, and C. A. Bishop, Thin Solid Films 80, 31 (1981).

[55]R. P. Howson, M. I. Ridge, and C. A. Bishop, Thin Solid Films 80, 137 (1981).

[56]M. I. Ridge and R. P. Howson, Thin Solid Films 96, 121 (1982).

[57]M. I. Ridge, R. P. Howson, and C. A. Bishop, Proc. Soc. Photo-Opt. Instrum. Eng. 325, 47 (1982).

[58]W. C. Kittler, Jr. and I. T. Ritchie, Proc. Soc. Photo-Opt. Instrum. Eng. 325, 61 (1982).

[59]H. Hennig, K. -H. Heckner, D. Hirsch, and H. Ladwig, Phys. Status Solidi A 74, 133 (1982).

[60]R. P. Howson, M. I. Ridge, and K. Suzuki, Proc. Soc. Photo-Opt. Instrum. Eng. 428, 14 (1983).

[61]J. Szczyrbowski, A. Dietrich, and H. Hoffman, Phys. Status Solidi A 69, 217 (1982); 78, 243 (1983).

[62]T. Ohyama, M. Okamoto, and E. Otsuka, J. Phys. Soc. Jpn. 52, 3571 (1983).

[63]M. Fujinaka and A. A. Berezin, Thin Solid Films 101, 7 (1983).

[64]T. Horodyski, K. Budzynska, and E. Leja, Thin Solid Films 106, 195 (1983).

[65]S. -J. Jiang and C. G. Granqvist, Proc. Soc. Photo-Opt. Instrum. Eng. 562, 129 (1985).

[66]J. L. Vossen, RCA Rev. 32, 289 (1971).

[67]J. L. Vossen and E. S. Poloniak, Thin Solid Films 13, 281 (1972).

[68]D. B. Frazer and H. D. Cook, J. Electrochem. Soc. 119, 1368 (1972).

[69]J. Jurisson, R. E. Peterson, and H. Y. B. Mar, J. Vac. Sci. Technol. 12, 1010 (1975).

[70]J. C. C. Fan and F. J. Bachner, J. Electrochem. Soc. 122, 1719 (1975); Appl. Opt. 15, 1012 (1976).

[71]K. Itoyama, Jpn. J. Appl. Phys. 17, 1191 (1978).

[72]W. G. Haines and R. H. Bube, J. Appl. Phys. 49, 304 (1978).

[73]Y. Sawada and Y. Taga, Thin Solid Films 110, L129 (1983).

[74]M. Russak and J. DeCarlo, J. Vac. Sci. Technol. A 1, 1563 (1983).

[75]S. Ray, R. Banerjee, N. Basu, A. K. Batabyal, and A. K. Barua, J. Appl. Phys. 54, 3497 (1983).

[76]J. E. Morris, M. I. Ridge, C. A. Bishop, and R. P. Howson, J. Appl. Phys. 51, 1847 (1980).

[77]J. Machet, J. Guille, P. Saulnier, and S. Robert, Thin Solid Films 80, 149 (1981).

[78]C. Yuanri, X. Xinghao, J. Zhaoting, P. Chuancai, and X. Shuyun, Thin Solid Films 115, 195 (1984).

[79]J. F. Smith, A. J. Aronson, D. Chen, and W. H. Class, Thin Solid Films 72, 469 (1984).

[80]O. Kuboi, Jpn. J. Appl. Phys. 20, L783 (1981).

[81]R. Groth, Phys. Status. Solidi 14, 69 (1966).

[82]R. Clanget, Appl. Phys. 2, 247 (1973).

[83]H. Köstlin, R. Jost, and W. Lems, Phys. Status Solidi A 29, 87 (1975).

[84]J. Kane, H. P. Schweizer, and W. Kern, Thin Solid Films 29, 155 (1975).

[85]R. B. Goldner and H. M. Haskall, Appl. Opt. 14, 2328 (1975).

[86]R. B. Goldner, Appl. Opt. 16, 808 (1977).

[87]S. Kulaszewicz, I. Lasocka, and G. Michalski, Thin Solid Films 55, 283 (1979).

[88]J. C. Manifacier, L. Szepessy, J. F. Bresse, M. Perotin, and R. Stuck, Mater. Res. Bull. **14**, 163 (1979).

[89]E. Kawamata and K. Ohshima, Jpn. J. Appl. Phys. **18**, 205 (1979).

[90]J. P. Schunck and A. Coche, Appl. Phys. Lett. **35**, 863 (1979).

[91]P. R. Sharma, T. C. Anthony, S. Ashok, S. J. Fonash, and L. L. Tongson, Jpn, J. Appl. Phys. **19**, Suppl. 19-1, 551 (1980).

[92]S. Kulaszewicz, Thin Solid Films **76**, 89 (1981).

[93]J. C. Manifacier, J. P. Filard, and J. M. Bind, Thin Solid Films **77**, 67 (1981).

[94]G. Blandenet, M. Court, and Y. Lagarde, Thin Solid Films **77**, 81 (1981).

[95]R. Pommier, C. Grill, and J. Marucchi, Thin Solid Films **77**, 91 (1981).

[96]G. Frank, E. Kauer, and H. Köstlin, Thin Solid Films **77**, 107 (1981).

[97]P. Turner, R. P. Howson, and C. A. Bishop, Thin Solid Films **83**, 253 (1981).

[98]G. Frank, E. Kauer, H. Köstlin, and F. J. Schmitte, Proc. Soc. Photo-Opt. Instrum. Eng. **324**, 58 (1982); Solar Energy Mater. **8**, 387 (1983).

[99]G. Frank and H. Köstlin, Appl. Phys. A **27**, 197 (1982).

[100]L. A. Ryabova, V. S. Salun, and I. A. Serbinov, Thin Solid Films **92**, 327 (1982).

[101]H. S. Soni, S. D. Sathaye, and A. P. B. Sinha, Indian J. Pure Appl. Phys. **21**, 197 (1983).

[102]L. Gouskov, J. M. Saurel, C. Gril, M. Boustani, and A. Oemry, Thin Solid Films **99**, 365 (1983).

[103]M. Privman, J. Berger, and D. S. Tannhauser, Thin Solid Films **102**, 117 (1983).

[104]S. Kulaszewicz, W. Jarmoc, and K. Turowska, Thin Solid Films **112**, 313 (1984); S. Kulaszewicz, W. Jarmoc, I. Lasocka, Z. Lasocki, and K. Turowska, Thin Solid Films **117**, 157 (1984).

[105]V. M. Donnelly, M. Geva, J. Long, and R. F. Karlicek, Appl. Phys. Lett. **44**, 951 (1984).

[106]A. K. Saxena, S. P. Singh, R. Thangaraj, and O. P.Agnihotri, Thin Solid Films **117**, 95 (1984).

[107]N. J. Arfsten, J. Non-Cryst. Solids **63**, 243 (1984).

[108]J. N. Avaritsiotis and R. P. Howson, Thin Solid Films **77**, 351 (1981).

[109]Y. Hori, K. Doi, and I. Ikuzo, Oyo Butsuri, **34**, 507 (1965).

[110]C. A. Pan and T. P. Ma, Appl. Phys. Lett. **37**, 163, 714 (1980); J. Electrochem. Soc. **128**, 1953 (1981); J. Electron. Mater. **10**, 43 (1981).

[111]D. Laser, J. Appl. Phys. **52**, 5179 (1981); Thin Solid Films **90**, 317 (1982).

[112]Z. Ovadyahu and Y. Imry, Phys. Rev. B **24**, 7439 (1981).

[113]Z. Ovadyahu and H. Wiesman, J. Appl. Phys. **52**, 5865 (1981).

[114]Z. Ovadyahu, S. Moehlecke, and Y. Imry, Surf. Sci. **113**, 544 (1982).

[115]A. F. Hebard and S. Nakahara, Appl. Phys. Lett. **41**, 1130 (1982).

[116]T. -C. Chen, T. -P. Ma, and C. Baker, Appl. Phys. Lett. **43**, 901 (1983).

[117]D. K. Jain and J. C. Garg, Indian J. Pure Appl. Phys. **18**, 842 (1980).

[118]K. B. Sundaram and G. K. Bhagavat, Phys. Status Solidi A **63**, K15 (1981).

[119]L. Holland and G. Siddall, Vacuum **3**, 375 (1953).

[120]A. Thelen and H. König, Naturwissenschaften **43**, 297 (1956).

[121]V. I. Fistul' and V. M. Vainshtein, Fiz. Tverd. Tela **8**, 3447 (1966) [Sov. Phys.—Solid State **8**, 2769 (1967)]; V. M. Vainshtein and V. I. Fistul', Fiz. Tekh. Poluprovodn. **1**, 135 (1967); **4**, 1495 (1970) [Sov. Phys. Semicond. **1**, 104 (1967); **4**, 1278 (1970)].

[122]H. K. Müller, Phys. Status Solidi **27**, 723, 733 (1968).

[123]E. B. Kaganovich, V. D. Ovsjannikov, and S. V. Svechnikov, Thin Solid Films **60**, 335 (1979).

[124]J. Szczyrbowski, A. Dietrich, and H. Hoffman, Phys. Status Solidi A **69**, 217 (1982).

[125]S. S. Bawa, S. S. Sharma, S. A. Agnihotry, A. M. Biradar, and S. Chandra, Proc. Soc. Photo-Opt. Instrum. Eng. **428**, 22 (1983).

[126]Y. Murayama, J. Vac. Sci. Technol. **12**, 818 (1975).

[127]R. P. Howson, J. N. Avaritsiotis, M. I. Ridge, and C. A. Bishop, Thin Solid Films **58**, 379 (1978); **63**, 163 (1979).

[128]A. Fischer, Z. Naturforsch. A **9**, 508 (1954).

[129]E. Kauer and A. Rabenau, Z. Naturforsch. **13a**, 531 (1958); H. J. J. von Boort and R. Groth, Philips Tech. Rev. **29**, 17 (1968).

[130]A. V. Sheklein and N. B. Rekant, Geliotekhnika **7**(3), 41 (1971) [Appl. Solar Energy **7**(3), 24 (1971)].

[131]E. Kawamata and K. Ohshima, Jpn. J. Appl. Phys. **18**, 205 (1979).

[132]O. Tabata, T. Tanaka, M. Waseda, and K. Kinuhama, Surf. Sci. **86**, 230 (1979).

[133]A. P. Mammana, E. S. Braga, I. Torriani, and R. L. Anderson, Thin Solid Films **85**, 355 (1981).

[134]N. Croitoru and E. Bannett, Thin Solid Films **82**, 235 (1981).

[135]G. Rupprecht, Z. Phys. **139**, 504 (1954).

[136]C. M. Lampert, Ind. Eng. Chem. Prod. Res. Dev. **21**, 612 (1982).

[137]C. M. Lampert, Energy Res. **7**, 359 (1983).

[138]P. H. Berning, Appl. Opt. **22**, 4127 (1983).

[139]C. G. Granqvist, Proc. Soc. Photo-Opt. Instrum. Eng. **401**, 330 (1983).

[140]C. M. Lampert, Opt. Eng. **23**, 92 (1984).

[141]C. G. Granqvist, Physics Teacher **22**, 372 (1984).

[142]C. G. Granqvist, Phys. Scr. **32**, 401 (1985).

[143]C. G. Granqvist, I. Hamberg, and J. S. E. M. Svensson, Ind. Eng. Chem. Prod. Res. Dev. **24**, 93 (1985).

[144]M. P. Thekaekara, in *Solar Energy Engineering*, edited by A. A. M. Sayigh (Academic, New York, 1977), p. 37. The data for the less turbid atmosphere in Table 3.5 are used.

[145]M. P. Alpern, in *Handbook of Optics*, edited by W. G. Driscoll and W. Vaughan (McGraw-Hill, New York, 1978), p. 12–22.

[146]G. A. Niklasson and C. G. Granqvist, J. Appl. Phys. **55**, 3382 (1984).

[147]H. Hoffman, J. Pickl, M. Schmidt, and D. Krause, Appl. Phys. **16**, 239 (1978).

[148]R. Clanget, Ph. D. thesis, Universität des Saarlandes, Saarbrücken, Germany, 1973 (unpublished).

[149]M. Marezio, Acta Crystallogr. **20**, 273 (1966).

[150]*Landolt-Börnstein Numerical Data and Functional Relationships in Science and Technology, New Series* (Springer, Berlin, 1975), Vol. III/7 b 1, p. 64.

[151]F. A. Kröger, *The Chemistry of Imperfect Crystals*, 2nd edition (North-Holland, Amsterdam, 1974), Vol. 2.

[152]J. H. Weaver, C. Krafka, D. W. Lynch, and E. E. Koch, *Optical Properties of Metals, Physics Data* (Fachinformationszentrum Energie Physik Mathematik GmbH, Karlsruhe, Germany, 1981), Vol. 18-2.

[153]P. Winsemius, Ph. D. Thesis, Rijksuniversiteit te Leiden, the Netherlands, 1973 (unpublished).

[154]J. L. van der Pauw, Philips Res. Rep. **13**, 1 (1958).

[155]R. A. Smith, *Semiconductors*, 2nd edition (Cambridge University Press, Cambridge, 1978).

[156]I. Hamberg, Ph. D. Thesis, Chalmers University of Technology, Gothenburg, Sweden, 1984 (unpublished).

[157]N. Markuvitz, *Waveguide Handbook* (MIT Radiation Laboratory Series, 1951).

[158]O. S. Heavens, *Optical Properties of Thin Solid Films* (Butterworths, London, 1955).

[159]M. Born and E. Wolf, *Principles of Optics*, 6th ed. (Pergamon, Oxford, 1980).

[160]A. Hjortsberg, Appl. Opt. **20**, 1254 (1981).

[161]R. C. McPhedran, L. C. Botten, D. R. McKenzie, and R. P. Netterfield, Appl. Opt. **23**, 1197 (1984).

[162]P. -O. Nilsson, Appl. Opt. **7**, 435 (1968).

[163]T. S. Eriksson and A. Hjortsberg, Proc. Soc. Photo-Opt. Instrum. Eng. **428**, 135 (1983); Solar Energy Mater. **11**, 141 (1984).

[164]See, for example, F. Wooten, *Optical Properties of Solids* (Academic, New York, 1972).

[165]R. L. Weiher, J. Appl. Phys. **33**, 2834 (1962); R. L. Weiher and B. G. Dick, *ibid.* **35**, 3511 (1964); R. L. Weiher and R. P. Ley, *ibid.* **37**, 299 (1966).

[166]F. López-Aguilar, J. Costa-Quintana, and J. S. Muños, Phys. Status Solidi B **111**, 659 (1982); F. López-Aguilar and J. Costa-Quintana, *ibid.* **114**, 599 (1982); **118**, 779 (1983).

[167]W. Hirschwald and D. M. Kolb, in *Current Topics in Materials Science*, edited by E. Kaldis (North-Holland, Amsterdam, 1981), Vol. 7, p. 239.

[168]J. C. Boettger and A. B. Kunz, Phys. Rev. B **27**, 1359 (1983).

[169]J. Robertson, J. Phys. C **12**, 4767 (1979).

[170]L. Kopp, B. N. Harmon, and S. H. Liu, Solid State Commun. **22**, 677 (1977).

[171]D. W. Bullett, J. Phys. C **16**, 2197 (1983).

[172]J. C. C. Fan and J. B. Goodenough, J. Appl. Phys. **48**, 3524 (1977).

[173]N. F. Mott, *Metal-Insulator Transitions* (Taylor and Francis, London, 1974).

[174]P. P. Edwards and M. J. Sienko, Phys. Rev. B **17**, 2575 (1978).

[175]P. Grosse, *Freie Elektronen in Festkörpern* (Springer, Berlin, 1979).

[176]D. Mahan, *Many Particle Physics* (Plenum, New York, 1981).

[177]E. Burstein, Phys. Rev. **93**, 632 (1954).

[178]T. S. Moss, Proc. Phys. Soc. London Sect. B **67**, 775 (1954).

[179]J. Lindhard, Kgl. Danske Videnskab. Selskab. Mat. -Fys. Medd. **28**, No. 8 (1954).

[180]F. Urbach, Phys. Rev. **92**, 1324 (1953).

[181]M. V. Kurik, Phys. Status Solidi A **8**, 9 (1971).

[182]A. P. Roth, J. B. Webbs, and D. F. Williams, Solid State Commun. **39**,

R158   J. Appl. Phys., Vol. 60, No. 11, 1 December 1986

I. Hamberg and C. G. Granqvist   R158

[183]O. Carporaletti, Solar Energy Mater. 7, 65 (1982).

[184]H. Nanto, T. Minami, S. Shooji, and S. Takata, J. Appl. Phys. 55, 1029 (1984).

[185]H. Finkenrath, Z. Phys. 159, 112 (1960).

[186]T. Arai, J. Phys. Soc. Jpn. 15, 916 (1960).

[187]H. Koch, Phys. Status Solidi 7, 263 (1964).

[188]S. P. Lyashenko and V. K. Miloslavskii, Opt. Spektrosk. 19, 108 (1965) [Opt. Spectrosc. (USSR) 19, 55 (1965)].

[189]E. Shanti, A. Banerjee, V. Dutta, and K. L. Chopra, J. Appl. Phys. 51, 6243 (1980); 53, 1615 (1982); E. Shanti, A. Banerjee, and K. L. Chopra, Thin Solid Films 88, 93 (1982).

[190]K. B. Sundaram and G. K. Bhagavat, J. Phys. D 14, 921 (1981).

[191]K. Suzuki and M. Mizuhashi, Thin Solid Films 97, 119 (1982).

[192]A. J. Nozik, Phys. Rev. B 6, 453 (1972).

[193]N. Miyata, K. Miyake, K. Koga, and T. Fukushima, J. Electrochem. Soc. 127, 918 (1980).

[194]E. Leja, K. Budzyńska, T. Pisarkiewicz, and T. Stapiński, Thin Solid Films 100, 203 (1983).

[195]R. W. Keyes, Comm. Solid State Phys. 7, 149 (1977).

[196]R. A. Abram, G. J. Rees, and B. L. H. Wilson, Adv. Phys. 27, 799 (1978).

[197]G. D. Mahan, J. Appl. Phys. 51, 2634 (1980).

[198]K. -F. Berggren and B. E. Sernelius, Phys. Rev. B 24, 1971 (1981).

[199]L. Engström, Ph. D. Thesis, Linköping University, Linköping, Sweden, 1984 (unpublished).

[200]A. O. E. Animalu and V. Heine, Philos. Mag. 12, 1249 (1965).

[201]M. L. Cohen and V. Heine, in Solid State Physics, edited by H. Ehrenreich, F. Seitz, and D. Turnbull (Academic, New York, 1970), Vol. 24.

[202]G. H. Wannier, Elements of Solid State Theory (Cambridge University Press, Cambridge, 1959), p. 212.

[203]I. Hamberg and C. G. Granqvist, Proc. Soc. Photo-Opt. Instrum. Eng. 562, 137 (1985).

[204]D. J. Dunstan, J. Phys. C 15, L419 (1982).

[205]D. Redfield, Phys. Rev. 130, 914 (1963); 130, 916 (1963).

[206]T. Skettrup, Phys. Rev. B 18, 2622 (1978).

[207]H. Sumi and Y. Toyosawa, J. Phys. Soc. Jpn. 31, 342 (1971).

[208]J. F. McCann and J. O'M. Bockris, J. Electrochem. Soc. 128, 1719 (1981).

[209]F. T. Lioh, C. Y. Yang, K. Hakim, and S. N. Leoine, J. Appl. Electrochem. 13, 377 (1983).

[210]W. Erbs, J. Kiwi, and M. Grätzel, Chem. Phys. Lett. 110, 648 (1984).

[211]W. Franz, Z. Naturforsch. 13a, 484 (1958).

[212]L. V. Keldysh, Zh. Eksp. Teor. Fiz. 34, 1138 (1958) [Sov. Phys. JETP 7, 788 (1958)].

[213]E. Gerlach and P. Grosse, Festkörperprobleme 17, 157 (1977).

[214]B. R. Nag, Electron Transport in Compound Semiconductors, Vol. 11 of Springer Series in Solid-State Sciences (Springer, Berlin, 1980).

[215]D. Chattopadhyay and H. -J. Queisser, Rev. Mod. Phys. 53, 745 (1981).

[216]R. von Baltz and W. Escher, Phys. Status Solidi B 51, 499 (1972).

[217]M. G. Calkin and P. J. Nicholson, Rev. Mod. Phys. 39, 361 (1967).

[218]E. Gerlach, Phys. Status Solidi B 61, K97 (1974); E. Gerlach and M. Rautenberg, 65, K13 (1974).

[219]E. Gerlach and M. Rautenberg, Phys. Status Solidi B 86, 479 (1978).

[220]E. Gerlach and M. Rautenberg, Phys. Status Solidi B 67, 519 (1975); 81, 153 (1977); N. J. Doran and E. Gerlach, ibid. 73, 203 (1976); ibid. 76, K43 (1976); E. Gerlach, P. Grosse, M. Rautenberg, and W. Senske, ibid. 75, 553 (1976); E. Gerlach and K. Paier, ibid. 92, 495 (1979); E. Gerlach and H. Kluttig, ibid. 93, 443 (1979); E. Gerlach, ibid. 97, 119 (1980); E. Gerlach and B. Harbecke, ibid. 100, 187 (1980).

[221]W. Götze and P. Wölfle, Phys. Rev. B 6, 1226 (1972).

[222]J. S. Helman and W. Baltensperger, Phys. Rev. B 17, 2427 (1978).

[223]J. Hubbard, Proc. R. Soc. London Ser. A 243, 336 (1957).

[224]M. Shimoji, Liquid Metals (Academic, New York, 1977).

[225]L. Kleinman, Phys. Rev. 160, 585 (1967); 172, 383 (1968).

[226]R. W. Shaw, Jr., J. Phys. C 3, 1140 (1970).

[227]L. Hedin and B. I. Lundqvist, J. Phys. C 4, 2064 (1971).

[228]R. Lobo, Phys. Rev. B 8, 5348 (1973).

[229]K. S. Singwi, M. P. Tosi, R. H. Land, and A. Sjölander, Phys. Rev. 176, 589 (1968).

[230]P. Vashishta and K. S. Singwi, Phys. Rev. B 6, 875 (1972).

[231]P. Grosse, F. J. Schmitte, G. Frank, and H. Köstlin, Thin Solid Films 90, 309 (1982).

[232]I. Hamberg and C. G. Granqvist, J. Appl. Phys. 59, 2950 (1986).

[233]W. B. White and V. G. Keramidas, Spectrochim. Acta 28A, 501 (1972).

[234]G. L. Harding, Solar Energy Mater. 12, 169 (1985).

[235]G. L. Harding, I. Hamberg, and C. G. Granqvist, Solar Energy Mater. 12, 187 (1985).

[236]T. S. Eriksson, S. -J. Jiang, and C. G. Granqvist, Appl. Opt. 24, 745 (1985); T. S. Eriksson and C. G. Granqvist, J. Appl. Phys. 60, 2081 (1986).

[237]F. Kreith, Principles of Heat Transfer, 3rd ed. (International Textbook, Scranton, PA, 1973).

[238]J. A. Duffie and W. A. Beckman, Solar Engineering of Thermal Processes (Wiley, New York, 1980).

[239]N. B. Rekant and A. V. Sheklein, Geliotekhnika 4,(5) 49 (1968) [Appl. Solar Energy 4,(5) 35 (1968)].

[240]G. R. Hunt, C. H. Perry, and J. Ferguson, Phys. Rev. 134, A688 (1964).

[241]A. C. Hardy, Handbook of Colorimetry (Massachusetts Institute of Technology, Cambridge, MA, 1963).

[242]G. Wyszecki and W. S. Stiles, Color Science: Concepts and Methods, Quantitative Data and Formulas, 2nd ed. (Wiley, New York, 1982).

[243]D. B. Judd and G. Wyszecki, Color in Business, Science and Industry (Wiley, New York, 1975).

[244]G. Wyszecki, in Handbook of Optics, edited by W. G. Driscoll and W. Vaughan (McGraw-Hill, New York, 1978), Sec. 9.

[245]F. Grum and C. J. Bartleson, eds., Optical Radiation Measurements, Vol. 2, Color Measurement (Academic, New York, 1980).

[246]D. L. MacAdam, Color Measurement: Theme and Variations, Vol. 27 of Springer Series of Optical Sciences (Springer, Berlin, 1981).

[247]W. L. Wolfe, in Handbook of Optics, edited by W. G. Driscoll and W. Vaughan (McGraw-Hill, New York, 1978), p. 7–95.

[248]R. K. Whitney, Corning Glass Works (private communication).

[249]L. Viña and M. Cardona, Phys. Rev. B 29, 6739 (1984).

[250]R. B. Goldner, A. Brofos, G. Foley, E. L. Goldner, T. E. Haas, W. Henderson, P. Norton, B. A. Ratnam, N. Weis, and K. K. Wong, Proc. Soc. Photo-Opt. Instrum. Eng. 502, 54 (1984).

[251]B. O. Seraphin, in Solar Energy Conversion: Solid State Physics Aspects, Vol. 31 of Topics in Applied Physics, edited by B. O. Seraphin (Springer, Berlin, 1979), p. 5.

[252]G. A. Niklasson and C. G. Granqvist, J. Mater. Sci. 18, 3475 (1983).

[253]Y. Sawada and Y. Taga, Thin Solid Films 116, L55 (1984).

[254]L. N. Alexandrov and A. S. Ivantsev, Appl. Surf. Sci. 11/12, 563 (1982).

[255]K. Honda, A. Ishizaki, Y. Yuge, and T. Saitoh, Proc. Soc. Photo-Opt. Instrum. Eng. 428, 29 (1983).

[256]S. H. Howe, in Coatings for Energy Efficiency and Solar Applications, edited by J. J. Mason (UK Section of the International Solar Energy Society, London, 1984), p. 33.

[257]J. S. E. M. Svensson and C. G. Granqvist, Proc. Soc. Photo-Opt. Instrum. Eng. 502, 30 (1984).

[258]C. M. Lampert, Solar Energy Mater. 11, 1 (1984).

[259]J. S. E. M. Svensson and C. G. Granqvist, Solar Energy Mater. 11, 29 (1984); Appl. Phys. Lett. 45, 828 (1984); Thin Solid Films 126, 31 (1985).

[260]R. B. Goldner and R. D. Rauh, Proc. Soc. Photo-Opt. Instrum. Eng. 428, 38 (1983); Solar Energy Mater. 11,177 (1984); R. B. Goldner, D. H. Mendelsohn, J. Alexander, W. R. Henderson, D. Fitzpatrick, T. E. Hass, H. H. Sample, R. D. Rauh, M. A. Parker, and T. L. Rose, Appl. Phys. Lett. 43, 1093 (1983); D. H. Mendelsohn and R. B. Goldner, J. Electrochem. Soc. 131, 857 (1984); R. D. Rauh, S. F. Cogan, and M. A. Parker, Proc. Soc. Photo-Opt. Instrum. Eng. 502, 38 (1984).

[261]D. K. Benson, C. E. Tracy, and M. R. Ruth, Proc. Soc. Photo-Opt. Instrum. Eng. 502, 46 (1984).

R159   J. Appl. Phys., Vol. 60, No. 11, 1 December 1986

I. Hamberg and C. G. Granqvist   R159